

# NEW APPROACH TO ANALYSE SPIN PROBE AND SPIN TRAP ESR

Katerina Makarova

**Thesis Committee****Thesis supervisor:**

Prof. Dr. H. van Amerongen,  
Professor of Biophysics  
Wageningen University

**Thesis co-supervisor:**

Dr. H. Van As,  
Associate Professor of Biophysics  
Wageningen University

**Other members:**

Prof. Dr. C.J.F. ter Braak (Wageningen UR, PRI)  
Prof. Dr. V.V. Apanasovich (Belarusian State University)  
Dr. M. I. Huber (Leiden University)  
Dr. J.J. Vervoort (Wageningen University)

This research was conducted under the auspices of the Graduate School of Experimental Plant Sciences.

# NEW APPROACH TO ANALYSE SPIN PROBE AND SPIN TRAP ESR

Katerina Makarova

## **Thesis**

Submitted in partial fulfilment of the requirements for the degree of doctor  
at Wageningen University  
by the authority of the Rector Magnificus  
Prof. dr. M.J. Kropff,  
in the presence of the  
Thesis Committee appointed by the Doctorate Board  
to be defended in public  
on Wednesday, January 19, 2011  
at 1:30 p.m. in the Aula

Katerina Makarova, 2011  
“New approach to analyse spin probe and spin trap ESR”  
PhD thesis, Wageningen University, Nederland  
met een samenvatting in het Nederlands

ISBN: 978-90-8585-840-9

# CONTENTS

<b>Abbreviations.....</b>	<b>1</b>
<b>General introduction.....</b>	<b>1</b>
1.1. Basic principals and parameters of Electron Spin Resonance .....	2
1.1.1. High-field ESR .....	6
1.1.2. Spin probe.....	6
1.1.3. Spin trapping .....	7
1.2. Data analysis .....	8
1.2.1. Simulation Based Fitting .....	9
1.2.2. Simulation of fast isotropic ESR spectra.....	9
1.3. Computational chemistry .....	10
1.3.1. Geometry optimization.....	11
1.3.2. Transition structure.....	12
1.3.3. Intrinsic reaction coordinate method.....	13
1.3.4. Enthalpy of reaction .....	13
1.3.5. Gibb's free energy .....	14
1.3.6. Magnetic parameters calculation.....	15
1.3.7. Solvent effect.....	15
1.4. Artificial neural networks .....	16
1.4.1. Multi Layer Perceptron .....	17
1.4.2. Radial Basis Function networks .....	18
1.5. Outline of the thesis .....	19
<b>References .....</b>	<b>21</b>
<b>Use of multifrequency ESR and simulation based fitting in partition studies of TEMPO in lipid bilayers .....</b>	<b>23</b>
2.1. Introduction.....	24
2.2. Material and Method.....	27
2.2.1. Materials.....	27
2.2.2. Sample preparation.....	27
2.2.3. ESR spectroscopy.....	28
2.3. Theory .....	28
2.3.1. Calculation of ESR spectral line shapes.....	28
2.4. Results.....	31
2.5. Discussion.....	36
2.5.1. Mathematical model for spectrum simulations .....	37
2.5.2. Simulations of High Field spectra .....	39
2.5.3. Analysis of X band spectra.....	40

2.6. Conclusions.....	42
<b>References .....</b>	<b>43</b>
<b>Spin trapping study of the influence of taxifolin on Fenton reaction in ethanol and methanol.....</b>	<b>47</b>
3.1 Introduction.....	48
3.2 Experimental details .....	48
3.2.1 ESR spectroscopy.....	48
3.2.2 Generation of free radicals for ESR .....	49
3.3 Results and discussions.....	49
3.3.1 Spin Trapping in solvents.....	49
3.3.2 Spin trapping in Fenton reagents in the presence of taxifolin solutions .....	51
3.4 Conclusions.....	52
<b>References .....</b>	<b>54</b>
<b>A combination of Neural Networks and DFT calculations for comprehensive analysis of FDMPO radical adducts from fast isotropic Electron Spin Resonance spectra .....</b>	<b>55</b>
4.1 Introduction.....	56
4.2 Materials and Methods.....	59
4.2.1 ESR spectra simulation .....	59
4.2.2 Neural Network Modeling.....	59
4.2.3 Training and testing data sets. ....	60
4.2.4 DFT calculations .....	62
4.2.5 Sample preparation.....	62
4.2.6 ESR measurements.....	62
4.3 Results and discussion .....	63
4.3.1 ESR spectra simulation .....	63
4.3.2 Development of ANN for identification of radical adducts on the basis of spectral parameters according to the chemical structure.....	65
4.3.3 ESR parameters of FDMPO spin adducts calculated by DFT .....	68
4.4 Conclusions.....	72
<b>References .....</b>	<b>75</b>
<b>Free radical reaction pathway, thermochemistry of peracetic acid homolysis and its application for phenol degradation: spectroscopic study and quantum chemistry calculations.....</b>	<b>79</b>
5.1 Introduction.....	80
5.2 Experimental Section.....	82
5.2.1 Instrumental.....	82
5.2.2 ANN computation. ....	83
5.2.3 Quantum Chemistry Calculations. ....	83
5.3 Results and Discussion .....	83

5.3.1 Detection of Free Radicals .....	83
5.3.2 Formation Mechanism of Detected Radicals. ....	85
5.3.3 Thermochemistry of free radicals formation in MnO <sub>2</sub> /PAA system. ....	86
5.3.4 Phenol oxidation by MnO <sub>2</sub> /PAA system. ....	88
5.3.5 ANN Model Development. ....	88
<b>References .....</b>	<b>101</b>
<b>A neural network approach to the rapid analysis of the kinetics of FDMPO free radical spin adducts from isotropic ESR spectra .....</b>	<b>105</b>
6.1 Introduction.....	106
6.2 Material and methods.....	108
6.2.1 Sample preparation.....	108
6.2.2 Plant material.....	109
6.2.3 ESR.....	109
6.2.4 Simulation based fitting.....	109
6.2.5 Artificial Neural Network .....	110
6.2.6 Training set construction .....	111
6.3 Results and discussion .....	112
6.3.1 Spectra analysis using simulations .....	112
6.3.2 Choice of ANN architecture.....	114
6.3.3 Analysis of spectra observed during Fenton reactions .....	116
6.3.4 Kinetic analysis .....	118
6.3.5 Comparison of the efficiency of iterative analysis and artificial neural networks .....	119
6.4 Conclusions.....	121
<b>References .....</b>	<b>123</b>
<b>Summarizing Discussion.....</b>	<b>127</b>
7.1 Introduction.....	127
7.2 Modeling and analysis of the ESR spectrum (Chapters 2,3,4,5,6) .....	127
7.3 DFT calculations (Chapters 4 and 5) .....	130
7.4 Artificial neural networks (Chapters 4, 5 and 6) .....	131
7.5 General conclusions.....	132
<b>Samenvatting .....</b>	<b>133</b>
<b>Acknowledgments.....</b>	<b>139</b>
<b>Curriculum vitae .....</b>	<b>143</b>
<b>Publications.....</b>	<b>144</b>





## ABBREVIATIONS

14:1PC (DMOPC)	1,2-Dimyristoleoyl- <i>sn</i> -glycero-3-phosphocholine
16:1PC (DPOPC)	1,2-Dipalmitoleoyl- <i>sn</i> -glycero-3-phosphocholine
18:1PC (DOPC)	1,2-Dioleoyl- <i>sn</i> -glycero-3-phosphocholine
20:1PC (DEiPC)	1,2-Dieicosenoyl- <i>sn</i> -glycero-3-phosphocholine
22:1PC (DEPC)	1,2-Dierucoyl- <i>sn</i> -glycero-3-phosphocholine
18:1PG (DOPG)	1,2-Dioleoyl- <i>sn</i> -glycero-3-[phospho- <i>rac</i> -(1-glycerol)]
DMSO	Dimethylsulfoxide
NMR	Nuclear magnetic resonance
ESR	Electron spin resonance (or electron paramagnetic resonance)
HF ESR	High-field electron spin resonance
pd-TEMPO	Per-deuterated 2,2,6,6-tetramethylpiperidine-1-oxyl spin probe
TEMPO	2,2,6,6-Tetramethylpiperidine-1-oxyl spin probe
FDMPO	4-Hydroxy-5,5-dimethyl-2- trifluoromethylpyrroline-1-oxide
POBN	$\alpha$ -(4-Pyridyl-1-oxide)- <i>N</i> - <i>tert</i> -butylnitrone
DIPPMPO	5-Diisopropoxyphosphoryl-5-methyl-1-pyrroline N-oxide
2-TFDMPO	5,5-Dimethyl-2-(trifluoromethyl)-1-pyrroline N-oxide
PAA	Peracetic acid
ANN	Artificial neural network
MLP	Multi layer perceptron
RBF	Radial basis function
DFT	Density functional theory
TS	Transition structure
SBF	Simulation based fitting
AOP	Advanced oxidation processes
UV	Ultraviolet
US	Ultrasound



## **Chapter 1**

### **GENERAL INTRODUCTION**

Electron Spin Resonance (ESR) spectroscopy is a powerful tool for the direct study of free radicals, providing information about their surrounding and identity. Objects that normally don't possess an unpaired electron also can be studied using the spin probe ESR technique. In this way structural and chemical information about the surrounding of the unpaired electron can be obtained as well as dynamic information about the spin probe motion. ESR spectra contain detailed information about the electron distribution in the molecule and the properties of its surroundings, but the analysis and interpretation of ESR data are quite complicated and involve different approaches ranging from simple estimation of signal intensity to sophisticated modeling of the molecule under study in order to predict its magnetic parameters.

The goal of this thesis is to develop new comprehensive methods for the analysis of ESR spectra and interpretation of magnetic parameters. A new approach for the analysis of fast isotropic spectra is proposed. It is based on a combination of an experimental approach (multifrequency ESR) and accurate spectra simulation using an improved model, that will be further introduced below. The determined magnetic parameters of the spin probe are directly interpreted in terms of structural information about the spin probe surroundings (lipid bilayer). The obtained magnetic parameters of various spin traps are interpreted by artificial neural networks (ANN) in order to obtain information about the identities of trapped radicals. Then, Density Functional Theory (DFT) calculations are applied to study the mechanism of reactions involving free radicals detected by spin trapping ESR and to calculate magnetic parameters of the radical adducts.

The purpose of this chapter is to provide a brief introduction of ESR spin-probe and spin-trap techniques, as well as to introduce the basic idea underlying the data analysis

approach for interpreting fast isotropic ESR spectra, computational chemistry and artificial neural networks as tools for the analysis of ESR data.

### 1.1. Basic principals and parameters of Electron Spin Resonance

Electron spin resonance (ESR), also called electron paramagnetic resonance (EPR), is a spectroscopic technique that detects chemical species that have unpaired electrons. A large number of materials, including free radicals, transition metal ions and defects in materials, have an unpaired electron and thus can be studied by the ESR technique (Abragam and Bleaney 1970). Materials, that do not posses unpaired electrons, such as lipid bilayers or proteins, can also be studied by ESR by introducing a spin probe or by spin labeling techniques (Berliner 1976). With the ESR technique the local environment (fluidity, viscosity and polarity) and molecular structure next to the unpaired electron can be studied as well as molecular motion. The general principle of ESR is based on the interaction of an unpaired electron with an external magnetic field (Zeeman effect). The essential aspects of ESR may be illustrated by considering the hypothetical case of a single isolated electron. The magnetic moment of an electron  $\mu$ , in the presence of an external magnetic field,  $B$ , orients parallel (the lowest energy state) or anti-parallel (the highest energy state) to the direction of the magnetic field. The projection of the magnetic moment  $\mu$  on the direction of the magnetic field is

$$S_z = \frac{hm_s}{2\pi} \quad (1)$$

where  $h$  is Planck's constant,  $m_s$  - the spin (projection) quantum number and  $m_s=-1/2$  for the parallel state and  $m_s=1/2$  for the anti-parallel state.

The difference in energy between the two states is proportional to the strength of the external magnetic field (Fig. 1). Using an oscillating magnetic field in the microwave range, a transition can be induced from the lower to the higher energy state and *vice versa*, but only if the energy of this microwave exactly matches the difference between the energy levels with  $|\Delta m_s| = 1$ . The equation describing the absorption or emission of microwave energy between the two spin states is

$$\Delta E = h\nu = g \mu_B B \quad (2)$$

where  $\Delta E$  is the energy difference between the two spin states,  $h$  – Planck's constant,  $g$  – the Zeeman splitting factor, which is close to  $g_e=2.0023$  (electron g-factor) for free radicals/spin

probes but its actual value depends on the electron configuration of the radical or ion,  $\mu_B$  – the Bohr magneton,  $B$  – the applied magnetic field,  $\nu$  – the microwave frequency. So the measured energy difference depends linearly on the magnetic field and without magnetic field, the energy difference is zero.

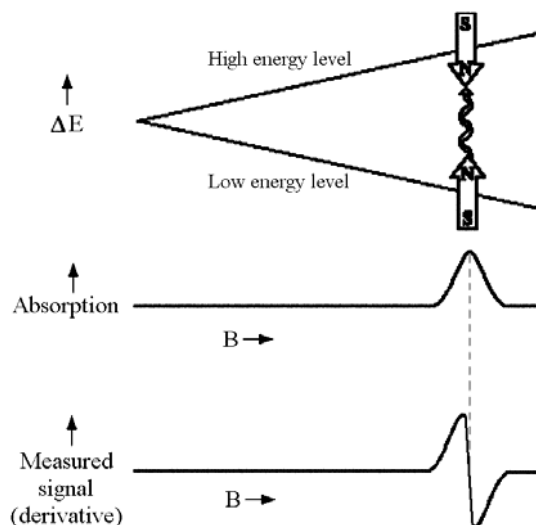


**Figure 1.** Variation of the energies of an electron spin state as a function of the applied magnetic field strength. Absorption occurs only if the energy ( $\mu_B g B$ ) exactly matches the difference between the energy levels with  $|m_S| = 1$ .

Usually, in ESR spectroscopy, the electromagnetic radiation frequency is kept constant, and the magnetic field is scanned. At the resonance field strength  $B$ , where the peak of absorption occurs, the energy of the radiation matches the energy difference of the two spin states. The resonance field and the frequency are related by the  $g$ -factor:

$$g = h\nu / (\mu_B B) \quad (3)$$

When  $B$  increases,  $\nu$  also increases, whereas  $g$  is a constant, the value of which is determined by the structure of the uncoupled electron orbits and local environments, i.e. by the properties of the paramagnetic species, but not by the external conditions. For another resonance frequency it will be another resonance field, but the ratio between resonance frequency and the strength of the resonance magnetic field will be the same and determined by the  $g$ -factor. At higher frequencies only the resolution of the  $g$ -factor is improved.

In addition to the  $g$ -factor, the unpaired electron is also very sensitive to its local surroundings, including the nuclei of nearby atoms that also have a magnetic moment and produce a local magnetic field at the electron. The interaction of an unpaired electron and a

nucleus is called hyperfine interaction. Each hyperfine interaction with a certain nucleus is characterized by the specific hyperfine splitting constant ( $a$ ).

$$h\nu = \mu_B g B + a m_I \quad (4)$$

where  $m_I$  is the nuclear quantum number. When the value of the hyperfine splitting constant is larger than the line broadening then well-separated peaks are observed in the ESR spectrum. In this case the hyperfine splitting constant provides information about the identity and number of atoms that make up a molecule. In nitroxide radicals the interaction with a nitrogen atom results in a three line pattern due to  $m_I = 0, \pm 1$  and  $a_N = 14\text{-}17$  G (Figure 2). On top of the interaction with nitrogen, there are also unresolved proton hyperfine interactions ( $m_I = \pm 1/2$ ,  $a_H = 0.2\text{-}0.5$  G (Kao, Barth et al. 2007)). The peaks arising from these interactions are strongly overlapping; as a result they broaden each peak in the nitroxide spectrum.

However, a nitroxide radical exhibits anisotropy, so the  $g$ -factor and hyperfine splitting constant are represented by  $3 \times 3$  matrices. In this case the hyperfine splitting constant and  $g$ -factor are referred to as  $g$  and  $a$ -tensors. Usually, for nitroxides a Cartesian molecule-fixed coordinate system  $[x, y, z]$  is defined, where the  $x$ -axis coincides with the N-O bond and the  $z$ -axis is along the  $2p_z$  axis of the nitrogen atom, and the  $y$ -axis is perpendicular to others (Figure 2).

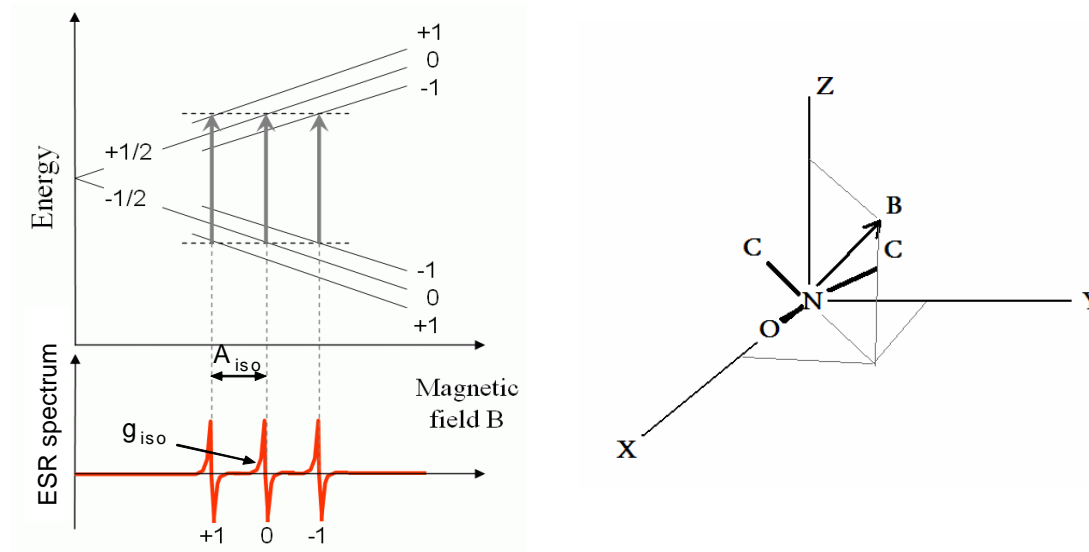


**Figure 2.** Nitroxide ESR spectra due to the interaction of an unpaired electron with  $^{14}\text{N}$  ( $m_I = 0, \pm 1$ ) and nitroxide principal axes for  $g$  and  $a$ -tensors.

Because of the symmetry of the  $2p_z$  orbital, the  $[x, y, z]$  axes system coincides with the principal axes of the  $g$  and  $a$  tensors, so  $g$  and  $a$ -tensors are diagonal in this axes system. The tensors for the 2,2,6,6-tetramethylpiperidinoxy (TEMPO) spin probe are presented below (Windle 1981).

$$\mathbf{g} = \begin{pmatrix} 2.0087 & 0 & 0 \\ 0 & 2.0061 & 0 \\ 0 & 0 & 2.0027 \end{pmatrix} \quad (5)$$

$$\mathbf{a} = \begin{pmatrix} 0.68 & 0 & 0 \\ 0 & 0.68 & 0 \\ 0 & 0 & 3.0 \end{pmatrix}, \text{ in mT.} \quad (6)$$

Moreover, the ESR spectral line shape contains information about dynamic processes such as molecular motion and fluidity (viscosity) in the local environment (Freed and Fraenkel 1963; Freed, Bruno et al. 1971). In this work only fast isotropic motion is considered. Then the molecule with the unpaired electron is allowed to tumble rapidly in an isotropic way as is the case in solutions or membranes, so the components of the  $g$ - and  $a$ -tensors are averaged out. The rotational motion is a random process, and its timescale is characterized by the rotational correlation time  $\tau_C$ , representing the characteristic time after which molecules with initially identical orientations lose their alignment. Generally, such isotropic motion should result in a Lorentzian line shape. However, there are some factors that broaden the ESR line, such as inhomogeneous broadening from unresolved hydrogen hyperfine structure or broadening caused by oxygen or other paramagnetic species. As a result of such broadening the Voigt shape occurs (convolution of Gaussian and Lorentzian) (Kivelson 1960). The linewidth of the Voigt shape is determined by the rotational correlation time,  $\tau_C$ , and the broadening constant,  $\Gamma_L$ . The mathematical model for the simulation of ESR spectra of 2,2,6,6-tetramethylpiperidine-1-oxyl spin probe (TEMPO) is described in Chapter 2. The same model is applied for the simulations of ESR spectra from 4-hydroxy-5,5-dimethyl-2-trifluoromethylpyrroline-1-oxide (FDMPO) (Chapter 4, 6),  $\alpha$ -(4-pyridyl-1-oxide)-*N*-*tert*-butylnitron (POBN) (Chapter 3) and 5-diisopropoxyphosphoryl-5-methyl-1-pyrroline N-oxide (DIPPMPO) (Chapter 5) spin traps.

The size of the ESR signal is related to the concentration of the ESR active species in the sample. In case of ESR, the size of the signal is determined as a second integral of the spectrum (integrated intensity).

To summarize, a fast isotropic ESR spectrum is characterized by 5 frequency-independent parameters, namely the integrated intensity, the g-factor, the hyperfine splitting constant or constants for several nuclei, the correlation time and the broadening constant.

### 1.1.1. High-field ESR

Traditionally, ESR experiments have been carried out at 9.5 GHz (X-band) and 0.3 T. Recently, a strong trend has evolved to expand the range of microwave frequencies and magnetic fields to higher values. High-field ESR offers the great advantage of increased spectral resolution, a gain in g-factor sensitivity and the sensitivity to a different motional regime, i.e. different  $\tau_C$ -values (Burghaus, Rohrer et al. 1992; Grinberg and Berliner 2004).

The biggest advantage attributed to HF ESR is directly derived from Eq. 3, that describes the interaction energies of an unpaired electron with the nuclei in a typical paramagnetic radical. By varying the external magnetic field  $B$ , it is now possible to separate the influence of the field dependent ( $\mu_B g B$ ) term from the field independent term ( $a$ ). The difference in resonance positions due to the electron Zeeman term for two different radicals with isotropic g-values  $g_1$  and  $g_2$  is given by :

$$\Delta B = \frac{h\nu}{\mu_B} \left( \frac{1}{g_1} - \frac{1}{g_2} \right) \quad (7)$$

This separation is a factor of 10 higher at 95 GHz (W-band) as compared to X-band ESR.

### 1.1.2. Spin probe

Objects such as biological membranes do not have intrinsic paramagnetic properties and therefore do not give rise to an ESR spectrum. However, they can be studied by ESR spectroscopy utilizing the spin probe technique, in which a paramagnetic probe is introduced into the system under study (Berliner 1976).

The spin label or spin probe can be any paramagnetic moiety that is sufficiently stable under the required experimental conditions and has a characteristic EPR spectrum that depends on the physical state of its close surroundings. The most commonly used spin probes are nitroxides. In nitroxides, the unpaired electron is located in a  $\pi$ -orbital on the nitrogen and oxygen atoms. The spin of the unpaired electron will interact with both nuclei, but since the oxygen nucleus has no spin, only the interaction with the nitrogen nucleus will be observed. Thus the ESR spectrum of nitroxides that are tumbling rapidly in solution exhibits a



characteristic primary triplet coupling splitting from the  $^{14}\text{N}$  nucleus of the nitroxide group. The spectrum shows a triplet with 1:1:1 signal intensity centered at  $g \sim 2.006$  (Figure 2). In spin probes, the magnitude of the nitrogen hyperfine splitting  $a_N$  and the  $g$ -tensor varies, depending on the spin probe surrounding environment (polarity). Moreover, the polarity dependence of the  $g$ - and  $a$ -tensors is opposite in nature: a spin probe in a more polar environment is characterized by larger  $a$ -tensor and lower  $g$ -tensor values.

Various spin labels and probes are being used, depending on the specific goal of the study. For example, TEMPO spin probes are often used to study properties of membranes (phase transition temperatures) (Bartucci and Sportelli 1993). In contrast to spin labels, which are covalently attached to some chemical reactive moiety, these spin probes can freely diffuse in the membrane and provide information about both the water and lipid phases. Thus, the ESR spectrum of TEMPO in a membrane is a superposition of two components coming from TEMPO in water (larger  $a_N$ ) and TEMPO in lipid phase ( $a_N$ ) (Figure 3).

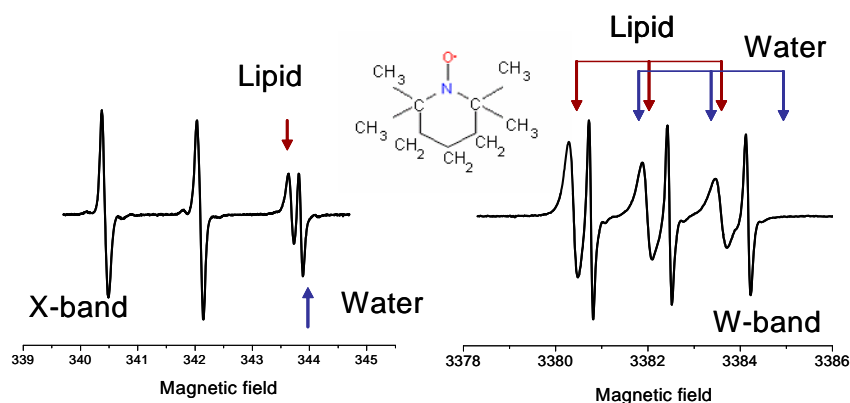


**Figure 3.** TEMPO spin probe and CW ESR spectrum of TEMPO in aqueous/ lipid phase at 9.5 GHz (X-band) and 95GHz (W-band).

The TEMPO spin probe is used in Chapter 2 for the study of lipid bilayers.

### 1.1.3. Spin trapping

The ESR spin-trapping technique is widely used for the detection and identification of short-lived free radicals (Janzen 1971; Janzen 1998). The method involves trapping of a short living free radical by an additional reaction to produce a more stable radical adduct, easily detectable by ESR. The appearance of the ESR spectra will depend on the original free radical structure, so the hyperfine coupling parameters of such an adduct permit identification of the initial radical. The main types of spin traps, which find use in studies of free radicals in biological systems, are nitroso and nitron derivatives. Nitrones can trap a large number of

different radicals including carbon, hydrogen, oxygen, etc. In this work FDMPO (Chapter 4, 6), POBN (Chapter 3) and DIPPMPO (Chapter 5) spin traps were used (Figure 4).

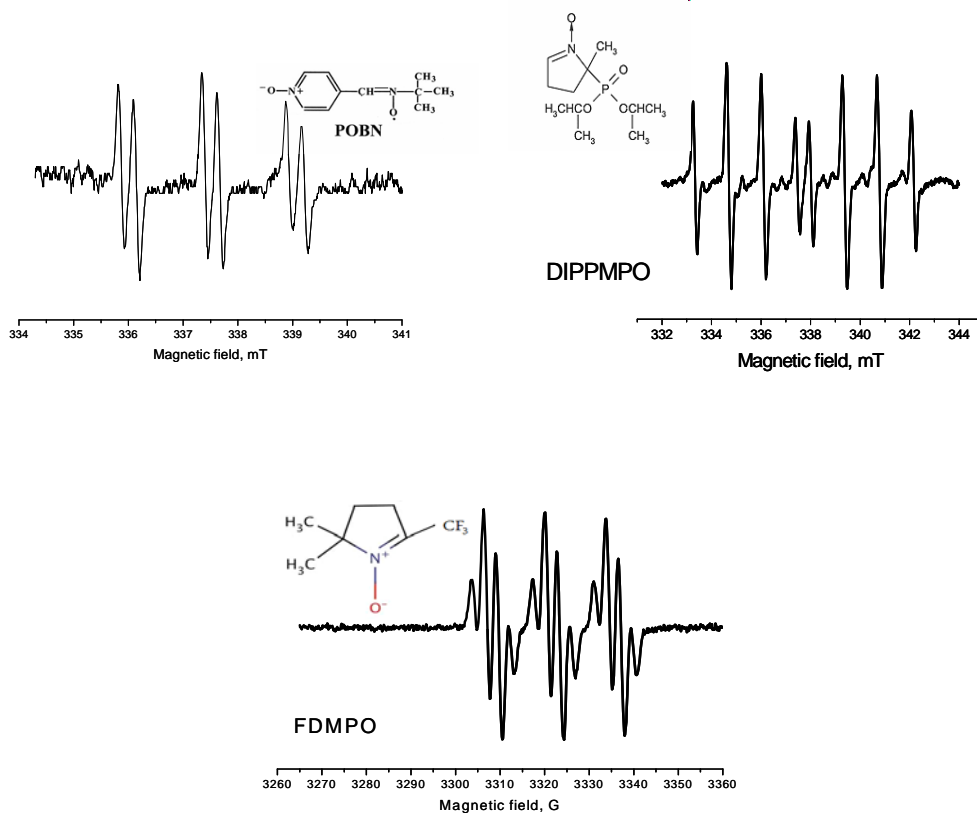


**Figure 4.** DIPPMPO, POBN and FDMPO spin trap structures and X-band spectra of their hydroxyl radical adducts at room temperature.

## 1.2. Data analysis

Data analysis is an important part of the research process. The goal of the analysis is to obtain information from raw data or characterize raw data by a set of parameters and to reveal trends in a data set. Methods of data analysis range from simple organization of data into informative tables or plots of experimental data to the creation of sophisticated models that describe the experimental system. Typically, these models require massive amounts of calculations, so computers are widely used for implementation of models and for calculations.

The primary goal of creating a model is to replicate the experimental system through simplification (Law and Kelton 1991). Therefore, only its essential and interesting properties are dealt with. In general, there is a compromise between accuracy and simplicity of the model i.e. a very accurate model could be too complex to implement, whereas a simple model could be highly inaccurate.

### 1.2.1. Simulation Based Fitting

Simulation based fitting (SBF) is used to find parameters of the model, that describe the system under study properly. Mathematically, the idea of SBF fitting is finding a global minimum of a function  $e$  with the corresponding set of parameters  $p=(p_1 \dots p_m)$  (so-called tuning parameters)

$$e=L(Yf(p)) \quad (8)$$

where  $L$  is a mathematical operator for a function,  $Y$  - experimental data,  $f(p)$  – artificial data obtained from an analytical function or simulation. Comparing experimental and artificial data by calculating the function  $e$ , the optimization procedure changes the tuning parameters, and the procedure repeats again, thereby trying to minimize the function  $e$  (Figure 5). There are several numerical optimization methods, which allow the minimization of the function  $e$ . In this work the non-derivative simplex method is used (Nelder and Mead 1965). This method constructs a simplex in the space of tuning parameters, so in the case of 2 parameters the simplex is represented by a line, 3-simplex is a triangle and 4-simplex is a tetrahedral, etc. Then the method moves the center of this simplex to the point where the target error goal is met.

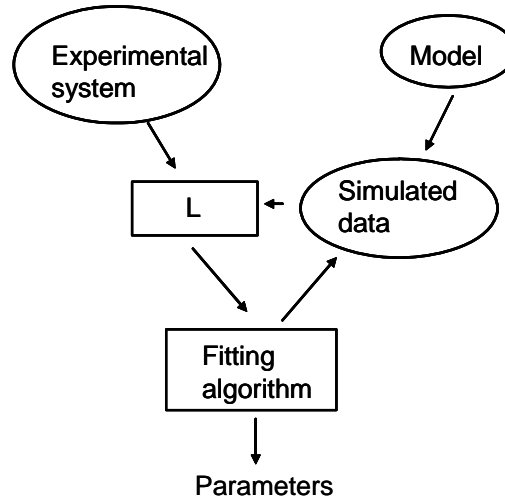


**Figure 5.** General scheme for simulation based fitting

### 1.2.2. Simulation of fast isotropic ESR spectra

In case of SBF applied to the analysis of ESR spectra, experimental and artificial data are represented by experimental and simulated ESR spectra. The simulated spectra are

constructed based on the tuning parameters: isotropic values of the hyperfine splitting constants and the g-tensor for the splitting pattern, and the correlation time, broadening, full hyperfine and g-tensors components for the line shape. The choice of the mathematical model for the line width approximation influences the accuracy of the correlation time parameter. The line width is a frequency dependent parameter, whereas the correlation time is not. Ideally, the approximation should be valid for any frequency. The mathematical model for the simulation of fast isotropic ESR spectra is presented in Chapter 2.

The function  $e$  is calculated as the sum of square errors between the two spectra.

$$e = \sum (Y - f(p))^2 \quad (9)$$

During the optimization the tuning parameters are varied in order to find the minimum value of  $e$ , which corresponds to the best fit.

### 1.3. Computational chemistry

Computational chemistry uses the models and results of theoretical chemistry, incorporated into efficient computer programs, to calculate structure and properties of molecules, for example ESR parameters. The calculations are based primarily on Schrödinger's equation and include the calculation of electron/charge distributions, molecular geometry in ground and excited states, potential energy surfaces, rate constants for reactions, etc. Thus, computational chemistry is used for the determination of molecular properties that are either inaccessible experimentally or can be obtained computationally more easily than by experimental means, in order to interpret experimental data and gain additional understanding of the molecular structure or chemical reaction under study.

Computational chemistry methods range from highly accurate to very approximate. The highly accurate methods are typically used for small systems, since the computational time increases rapidly with the size of the system under study. The programs used in computational chemistry are based on many different quantum chemical methods that solve the molecular Schrödinger's equation associated with the molecular Hamiltonian. Methods which are based entirely on theory and derived directly from theoretical principles, without the inclusion of experimental data are called *ab initio* methods (Parr 1990). In *ab initio* methods the energy of the system is expressed with the help of quantum-mechanical wavefunction, that describes the state of a molecule. The wavefunctions become significantly more complicated as the number of electrons increases, which limits the application of *ab*

*initio* methods to molecules with up to 40 electrons. *Ab initio* methods have the advantage that they can converge to the exact solution. However, the downside is the computational cost and the exact solution may never be reached. Density functional theory (DFT) methods derive energy of the molecule based on determination of the electron density which is a physical characteristic of all molecules (Parr and Weitao 1994). Moreover, determination of the electron density is independent of the number of electrons so systems with a few dozens of electrons could be studied by DFT methods with little computational costs. Molecules that are even larger (hundred of electrons) can be studied by semi-empirical approximate methods (Hückel 1931; Hoffmann 1963).

Over the last few years DFT-based methods have been widely accepted by the computational chemistry community as a reliable practical tool for the study of properties of the molecule, chemical reactions, etc. As the first step of the chemical reaction study, a geometry optimization is performed for each molecule under study, so the angles, dihedral angles and bond lengths are obtained. Then, the reaction path can be followed from reactants to products and the reaction is characterized in terms of enthalpy and Gibbs free energy changes. Moreover, optimized geometries reveal the spin density distribution and, thus allow to calculate magnetic parameters (hyperfine splitting constants) and to compare these with those determined from ESR experiments.

In this work all DFT calculations were carried out using the Gaussian 03 program, which provides possibilities for electronic structure modeling (Frisch, Trucks et al. 2003).

### 1.3.1. Geometry optimization

The geometry of a molecule determines many of its physical and chemical properties, so even a small variation in the arrangement of atoms and electrons in a molecule can lead to changes in the energy of the molecular system. In case of SBF applied to the optimization of the geometry of a molecule, the experimental and simulated data are represented by chemical structures, while the tuning parameters are bond lengths, angles and dihedral angles. Each molecular geometry is described by its energy content. So the aim of geometry optimization is to find a point of minimal energy by varying the geometrical tuning parameters (bond angles, bond distances and dihedral angles). The minimum energy structure(s) obtained in this way represent (an) equilibrium structure(s), which are most stable and most likely to be found in nature.

To observe the effect of small changes in the geometrical parameters on the energy content, the potential energy surface is calculated, which represents the mathematical

relationship of a particular molecular structure and the corresponding energy. In figure 6 the potential energy as a function of the OCO angle and the CC bond length is represented.

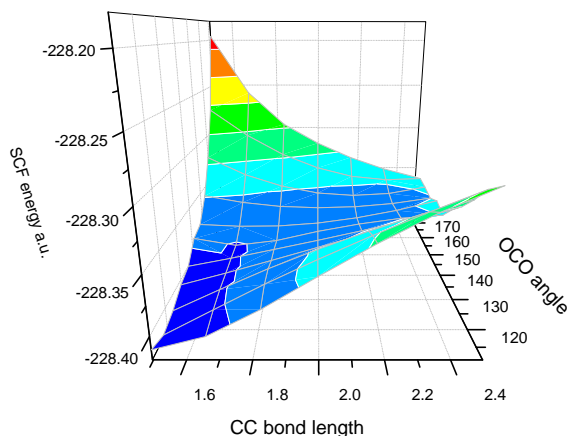


**Figure 6.** Potential energy surface for  $\text{CH}_3\text{CO}_2$ : total energy as a function of the OCO angle and the CC bond calculated at B3LYP/6-31G(d) level of theory

The potential energy surface is characterized by stationary points where the first derivative of the energy with respect to the coordinates is zero. The stationary points that correspond to minima represent the equilibrium structures for the molecule, such as different conformations and structural isomers. When several molecules undergoing a chemical reaction are considered, the extrema on the potential energy surface represent reactants and products. A saddle point (for a definition see next paragraph), which is also a stationary point but not an extremum, corresponds to the transition structure that connects products and reactants. So the idea of geometry optimization is to locate a stationary point based on a certain geometry of the molecule.

### 1.3.2. Transition structure

A point on the potential energy surface that is a maximum in one direction and a minimum in the other direction is a saddle point. Saddle points represent transition structures (TS's) connecting two equilibrium structures, so a TS is defined as the state corresponding to the highest energy along this reaction coordinate. Moreover, assuming a perfectly irreversible reaction, at this point the colliding reactant molecules will always go on to form products.

### 1.3.3. Intrinsic reaction coordinate method

Tracing the reaction path from a TS to reactants and products is essential for understanding the reaction. However, for some reactions the potential energy surface can be rather complicated such that it is not obvious whether the TS connects desired reactants and products. In this case, the path of a chemical reaction can be traced from the TS to the products and to the reactants, using the Intrinsic Reaction Coordinate method (Fukui 1981). Small steps along the negative gradient from the TS down to the local energy minimum in a mass-weighted coordinate system (Cartesian) are taken for calculations of the intrinsic reaction coordinate.

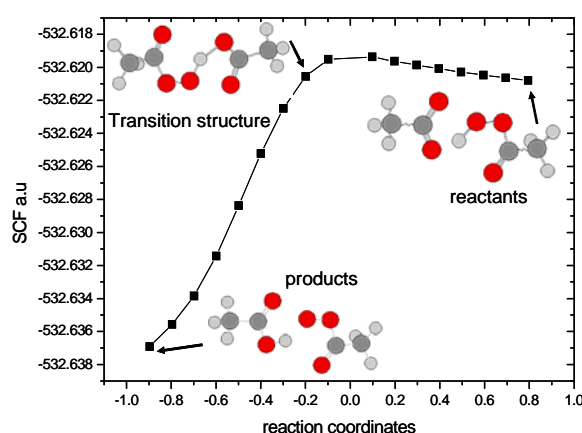


**Figure 7.** The reaction pathway from the reactants ( $\text{CH}_3\text{COOOH}$  and  $\text{CH}_3\text{COO}$ ) to the products ( $\text{CH}_3\text{COOH}$  and  $\text{CH}_3\text{COO}$ ) using Intrinsic Reaction Coordinate method calculated at B3LYP/6-31G(d) basis set.

The reaction of the dissociation of the peracetic acid O-O bond as well as subsequent reactions with formed free radicals was studied in chapter 5.

### 1.3.4. Enthalpy of reaction

Enthalpy describes the heat absorbed or released by the system under conditions of constant pressure. The absolute enthalpy is not measured directly, rather one usually deals with changes in enthalpy ( $\Delta H$ ), i.e. the heat added or lost by the system. The enthalpy change that accompanies a reaction is given by the difference between the enthalpies of the products and the reactants:

$$\Delta H = H_{\text{product}} - H_{\text{reactant}} \quad (7)$$

If the system has a higher enthalpy at the end of the reaction, then  $\Delta H$  is positive and the system absorbed heat from the surrounding (endothermic reaction). If the system has a lower enthalpy at the end of reaction, then  $\Delta H$  is negative and the system released heat during the reaction (exothermic reaction).

Gaussian 03 calculates the sum of electronic ( $\epsilon_o$ ) and thermal enthalpies ( $H_{corr}$ ), and thus the enthalpy of a reaction can be calculated as:

$$\Delta_r H^\circ(298K) = \sum (\epsilon_o + H_{corr})_{products} - \sum (\epsilon_o + H_{corr})_{reactants} \quad (8)$$

This works since the number of atoms of each element is the same on both sides of the reaction, therefore all the atomic information cancels out, and only the molecular data is needed.

### 1.3.5. Gibb's free energy

The Gibbs free energy, also called available energy, is a thermodynamic potential that measures the “useful” work obtained from an isothermal, isobaric thermodynamic system.

The change  $\Delta G$  in Gibbs free energy for an isolated system is defined as

$$\Delta G = \Delta H - T\Delta S_{int} \quad (9)$$

where  $\Delta H$  is the enthalpy change of the reaction (for a chemical reaction at constant pressure),  $S_{int}$  is the internal entropy of the system, T is the temperature. One can discern the following cases for a chemical reaction:

$\Delta G < 0$  : favored or spontaneous reaction

$\Delta G = 0$  : equilibrium situation

$\Delta G > 0$  : disfavored or nonspontaneous reaction

Gaussian 03 calculates the sum of electronic ( $\epsilon_o$ ) and thermal free energy ( $G_{corr}$ ), thus the Gibbs free energy of a reaction can be calculated as:

$$\Delta_r G^\circ(298K) = \sum (\epsilon_o + G_{corr})_{products} - \sum (\epsilon_o + G_{corr})_{reactants} \quad (10)$$



### 1.3.6. Magnetic parameters calculation

In first order approximation, the isotropic hyperfine coupling constant  $a_{\text{iso}}$ , which results from the interaction between an unpaired electron and nucleus A is equal to the Fermi-contact term and it is proportional to the spin density at the corresponding nucleus (Munzarová 2004).

$$a_{\text{iso}} = \frac{4}{3} \pi \mu_e \mu_A g_E g_A \langle S_z \rangle^{-1} \rho^{\alpha-\beta}(A) \quad (11)$$

where  $g_A$  is the nuclear  $g$  value,  $\langle S_z \rangle$  is the expectation value of the  $z$ -component of the total electron spin,  $\rho^{\alpha-\beta}(A)$  is the spin density at the nucleus A.

### 1.3.7. Solvent effect

The solvent effect on the  $a_{\text{iso}}(\text{N}^{14})$  values can be illustrated on the basis of two resonance structures of the nitroxide radicals:

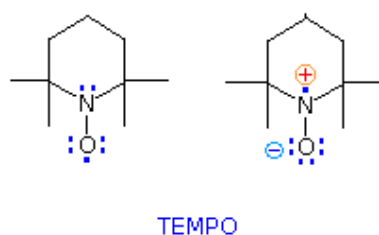


**Figure 8.** Two resonance structures of nitroxide in TEMPO

For example, water solvent induces an increase in electron spin density on the nitrogen atom of the nitroxide fragment due to stabilization of the polar resonance structure  $> \text{N}^+ - \text{O}^-$  at the expense of less polar structure  $> \text{N} - \text{O}^\bullet$ .

In order to take into account the effect of the solvent on the energy and, thus, the optimal geometry of the molecule in DFT calculations, Tomasi's polarized continuum model (PCM) is usually employed (Tomasi, Mennucci et al. 2005). This model considers only electrostatic solute-solvent interactions in order to mimic different solvents such as water ( $\epsilon=79$ ), DMSO ( $\epsilon=47.2$ ), ethanol ( $\epsilon=24.3$ ). The next step is to consider hydrogen bond formation between the solvent and solute molecules, as well as the spin density transfer onto the solvent molecule. This can be computed by including one or two solvent molecules interacting with the radical

center (Owenius, Engstrom et al. 2001). PCM and solvent molecules were used in DFT calculations of nitrogen and fluorine hyperfine splitting constants in chapter 4.

#### **1.4. Artificial neural networks**

Artificial neural networks (ANNs) have emerged as remarkable tools for pattern recognition, classification and the approximation of functions in scientific applications. They have been successfully applied to spectroscopic problems in magnetic resonance (Martinez and Millhauser 1998; Meiler and Will 2001).

AANs have been developed as a generalization of mathematical models of biological nervous systems (Wasserman 1989; Bishop 1995). The basic processing elements of an ANN are called artificial neurons or nodes. The synaptic connections between neurons are represented by numerical weights, which measure the strength of a connection. The non linear characteristic exhibited by neurons is represented by a transfer function that emulates the firing of the neuron.

The learning capability of an artificial neuron is achieved by adjusting the weights in accordance with a chosen learning algorithm. Once trained, an ANN can be an effective tool for the analysis of new data whose underlying statistics is similar to that of the training set. The general architecture of an ANN consists of three types of neuron layers: input, hidden and output layers (Figure 9).

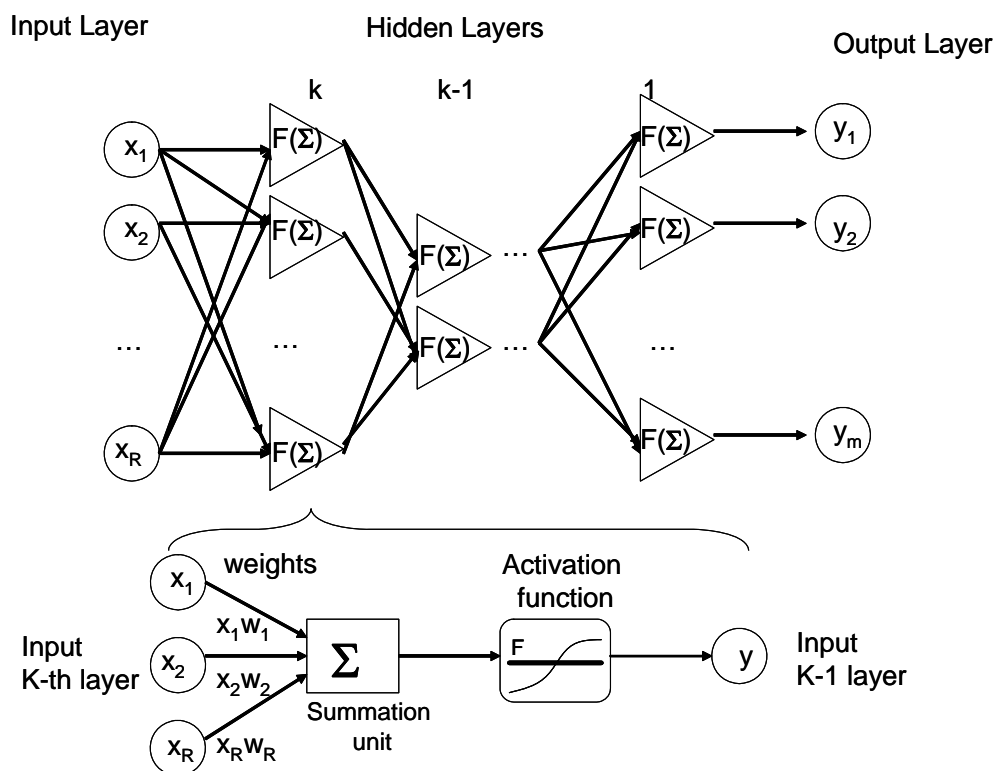


**Figure 9.** General architecture of an artificial neural network

#### 1.4.1. Multi Layer Perceptron

A Multi Layer Perceptron (MLP) is a type of neural network in which the output signals of the  $k$ -th layer are used as input for the neurons of the  $(k-1)$ -th layer Fig.9 (Rosenblatt 1958). The MLP has no feedback (connections that loop) and lateral (connections inside one layer) connections, so propagation of the information from inputs to outputs is very fast. Usually, a supervised training method, called back propagation, is used to train the MLP (Rumelhart, Hinton et al. 1986). As the first step the training pattern's input is propagated forward through the neural network to the output neurons. Subsequently, the actual network output is compared with the desired output values and error in each of the output units is calculated. The idea of training is to bring the error of each output neuron to zero by modifying the weights of the hidden layers (layer by layer).

The MLP is the standard architecture for any supervised-learning pattern recognition and function approximation problem. In chapter 4 an MLP was used for the classification of the FDMPO radical adducts structure based on hyperfine splitting constants determined from the ESR spectrum. In chapter 5 the MLP was used for “black box” modeling of the phenol removal efficiency. Peracetic acid and  $\text{MnO}_2$  concentrations as well as duration of treatment

were used as input for the MLP. The output of the MLP provides the phenol removal efficiency.

#### 1.4.2. Radial Basis Function networks

The Radial Basis Function (RBF) network is a three-layer feed forward network that uses a linear transfer function for the output units and a nonlinear transfer function (normally Gaussian) for the hidden layer neurons. The idea of an RBF network is inspired by the K-Nearest Neighbor (k-NN) models (Fix and Hodges Jr. 1989), i.e. an object is classified based on the closest training examples in the feature space (Fig. 10). Clearly, the result of the classification depends on how many neighboring points are considered, i.e. if  $k=3$  points are considered (Fig. 10), then the green circle is classified as a square, otherwise if  $k=5$  points are considered then the circle is classified as a triangle.

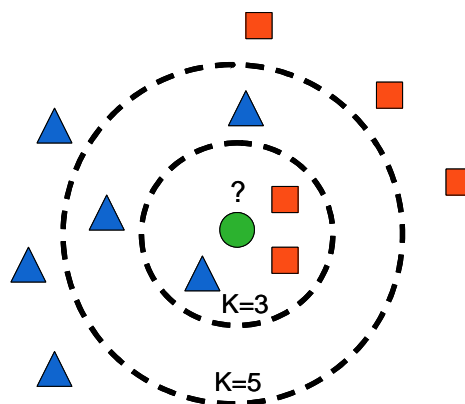


**Figure 10.** Example of the K-nearest neighbor classification. The test green circle is classified as a square when  $k=3$  closest neighbor points are considered (there are 2 squares and 1 triangle near the green circle). If  $k=5$  closest neighbor points are considered then the test circle is classified as a triangle (3 triangles vs 2 squares).

For the RBF network application the neighboring points are represented by neurons. Then the Euclidean distance is computed from the point being evaluated (input point) to the center of each neuron. The weight (influence) of each neuron is calculated by a radial basis function using the radius distance as an argument. In general, the further a neuron is away from the point being evaluated, the less influence it has. The RBF network differs in several ways from the MLP: (1) the method for comparing input and weight vectors, (2) the choice of the transfer function employed at each node in the hidden layer, (3) the method for choosing the number of nodes in the hidden layer, and (4) the procedure used for training the network (Moody and Darken 1989).

In chapter 6 an RBF network is used for extraction of fractions of FDMPO spin adducts from ESR spectra.

## 1.5. Outline of the thesis

This thesis describes the methods of analysis of the fast isotropic ESR spectra of the TEMPO spin probe and of FDMPO, POBN and DIPPMPO spin traps. In chapter 2, a method for analysis of ESR spectra is presented. The new approach consists of a combination of routine low frequency (9 GHz, X-band) and accurate high frequency (94 GHz, W-band) reference measurements and spectral fitting with fixed correlated parameters. Spectral fitting with the presented model and input values of  $\tau_R$  from the high frequency measurements, as expected, greatly improves the precision of the partition coefficient extracted from the X-band spectra. Based on  $f_{lipid}$ , the mole fraction partition coefficients for TEMPO in PC 20:1 and PC 14:1 are calculated.

In chapter 3, the influence of taxifolin on the Fenton reaction with ethanol and methanol is studied using the spin probe ESR approach. X-band ESR spectra of POBN spin adducts were analyzed with the model presented in chapter 2. The fitting of the experimental spectra made it possible to identify radical adducts that were formed in these reactions and to follow the kinetics of each component. Spectral decomposition reveals that the presence of taxifolin decreased the ESR signal intensity, affecting mainly the c-centered POBN radical adduct component.

In chapter 4, a combination of ANN and DFT calculation is used for comprehensive analysis of FDMPO radical adducts presented in the Fenton reaction with DMSO, methanol, ethanol and PAA cleavage over  $MnO_2$ . The model proposed in chapter 2 was adopted for the simulations of X-band ESR spectra of FDMPO spin adducts. An ANN was designed to estimate the chemical structure of FDMPO radical adducts based on obtained N- and F hyperfine splitting constants. The DFT calculations provide additional information about the chemical structure of these radical adducts and the influences of motional and solvent effects on the calculated N and F hyperfine splitting constants.

In chapter 5, the dissociation of the peracetic acid (PAA) O-O bond as a relevant source of free radicals (e.g.  $\bullet OH$ ) was studied in detail. Radicals formed as a result of chain radical reactions were detected with electron spin resonance (ESR) and nuclear magnetic resonance (NMR) spin trapping (ST) techniques and subsequently identified by means of a simulation based fitting (SBF) approach. The reaction mechanism is established with a complete assessment of relevant reaction thermochemistry and confirmed by electronic structure calculations at different levels of theory. Furthermore, the heterogeneous  $MnO_2$ /PAA system was tested for the elimination of phenol. An artificial neural network

(ANN) was designed to associate the removal efficiency of phenol with the process parameters such as the catalyst and PAA concentrations and the reaction time.

In chapter 6, the antioxidant activity of the ethanol extract of pine and narcissus pollen was studied. A fast approach using RBF neural networks is proposed for the analysis of ESR spectra of FDMPO spin adducts. The ethanol extract of pine pollen prevents the formation of FDMPO/CH<sub>3</sub> spin adduct in the Fenton reaction with DMSO, whereas the ethanol extract of narcissus pollen decreases the formation of both FDMPO/OH and FDMPO/CH<sub>2</sub>OH radical adducts in the Fenton reaction with methanol.

## REFERENCES

- Abragam, A. and B. Bleaney (1970). Electron Paramagnetic Resonance of Transition Ions Chapter 1: Introduction - Effective spin and anisotropy. Oxford, England, Clarendon Press.
- Bartucci, R. and L. Sportelli (1993). "ESR investigation on the phase transitions of DPPC vesicles in presence of high concentration of Li<sup>+</sup>, Na<sup>+</sup>, K<sup>+</sup> and Cs<sup>+</sup>." Colloid Polym. Sci. **271**(23): 262-267.
- Berliner, L. J. (1976). Spin labeling : theory and applications / edited by Lawrence J. Berliner. New York :, Academic Press.
- Bishop, C. M. (1995). Neural Networks for Pattern Recognition, Oxford University Press, Inc.
- Burghaus, O., M. Rohrer, et al. (1992). "A novel high-field/high-frequency EPR and ENDOR spectrometer operating at 3 mm wavelength." Meas. Sci. Technol. **3**: 765-774.
- Fix, E. and J. L. Hodges Jr. (1989). "Discriminatory Analysis: Nonparametric Discrimination: Consistency Properties." Int. Stat. Rev. **57**(3): 238-247.
- Freed, J. H., G. V. Bruno, et al. (1971). "Electron spin resonance line shapes and saturation in the slow motional region." J. Phys. Chem. **75**(22): 3385-3399.
- Freed, J. H. and G. K. Fraenkel (1963). "Theory of linewidths in Electron Spin Resonance spectra." J. Chem. Phys **39**(2): 326-350.
- Frisch, M. J., G. W. Trucks, et al. (2003). Gaussian 03, Revision C.02.
- Fukui, K. (1981). "The path of chemical reactions - the IRC approach." Acc. Chem. Res. **14**(12): 363-368.
- Grinberg, O. and L. J. Berliner (2004). Very High Frequency (VHF) ESR/EPR. New York, Kluwer/Plenum Publishers.
- Hoffmann, R. (1963). "An extended Hückel theory. I. Hydrocarbons." J. Chem. Phys. **39**(6): 1397-1412.
- Hückel, E. (1931). Zeitschrift für Physik **70**: 204.
- Janzen, E. G. (1971). "Spin trapping." Acc. Chem. Res. **4**(1): 31-40.
- Janzen, E. G. (1998). Spin trapping. Foundations of modern EPR. G. R. Eaton, S. S. Eaton and K. M. Salikhov, Singapore: World Scientific.
- Kao, J. P., E. D. Barth, et al. (2007). "Very-low-frequency electron paramagnetic resonance (EPR) imaging of nitroxide-loaded cells." Magn. Reson. Med. **58**(4): 850-854.

- Kivelson, D. (1960). "Theory of ESR linewidths of free radicals." J. Chem. Phys. **33**(4): 1094-1106.
- Law, A. and W. D. Kelton (1991). Simulation Modeling and Analysis, McGraw-Hill.
- Martinez, G. V. and G. L. Millhauser (1998). "A Neural Network Approach to the Rapid Computation of Rotational Correlation Times from Slow Motional ESR Spectra." J. Magn. Reson. **134**(1): 124-130.
- Meiler, J. and M. Will (2001). "Automated structure elucidation of organic molecules from <sup>13</sup>C NMR spectra using genetic algorithms and neural networks." J. Chem. Inform. Comput. Sci. **41**(6): 1535-1546.
- Moody, J. and C. J. Darken (1989). "Fast learning in networks of locally-tuned processing units." Neural. Comput. **1**(2): 281-294.
- Munzarová, M. L. (2004). DFT Calculations of EPR Hyperfine Coupling Tensors, Wiley-VCH Verlag GmbH & Co. KGaA.
- Nelder, J. A. and R. Mead (1965). "A simplex method for function minimization." Comp. J. **7**(4): 308-313.
- Owenius, R., M. Engstrom, et al. (2001). "Influence of solvent polarity and hydrogen bonding on the EPR parameters of a nitroxide spin label studied by 9-GHz and 95-GHz EPR spectroscopy and DFT calculations." J. Phys. Chem. A **105**(49): 10967-10977.
- Parr, R. and Y. Weitao (1994). Density-Functional Theory of Atoms and Molecules. New York, Oxford University Press.
- Parr, R. G. (1990). "On the genesis of a theory." Int. J. Quantum Chem. **37**(4): 327-347.
- Rosenblatt, F. (1958). "The perceptron: a probabilistic model for information storage and organization in the brain." Psychol. Rev. **65**(6): 386-408.
- Rumelhart, D. E., G. E. Hinton, et al. (1986). "Learning representations by back-propagating errors." Nature **323**(6088): 533-536.
- Tomasi, J., B. Mennucci, et al. (2005). "Quantum mechanical continuum solvation models." Chem. Rev. **105**(8): 2999-3094.
- Wasserman, P. D. (1989). Neural computing : theory and practice / Philip D. Wasserman. New York :, Van Nostrand Reinhold.
- Windle, J. J. (1981). "Hyperfine coupling constants for nitroxide spin probes in water and carbon tetrachloride." J. Magn. Reson. **45**(3): 432-439.



## Chapter 2

### USE OF MULTIFREQUENCY ESR AND SIMULATION BASED FITTING IN PARTITION STUDIES OF TEMPO IN LIPID BILAYERS

Katerina Makarova, Henrik Brutlach, Elena A. Golovina, Igor Borovykh

To be submitted

#### ABSTRACT

In this work the factors decreasing the accuracy of the parameters extracted from X-band spectra are explored. The multifrequency ESR approach is applied for improvement of the analysis of X-band data. The use of correlation times defined for TEMPO in aqueous (6.3ps) and lipid phases (61ps) from high-field ESR for X-band simulations improved the accuracy of lipid/water fraction parameters and made them as accurate as those obtained from the simulations of HF ESR spectra. In the presented work the multifrequency ESR spin probe partitioning approach was applied to the study of model membranes. The TEMPO lipid/water fraction parameter reflected changes in the polarity and structure of the lipid bilayers in the studies of DOPC/DOPG lipids and PC 14:1 and PC 20:1 lipids as a function of lipid concentration. The spin probe mole fraction partition coefficients for TEMPO in PC 14:1 ( $K_x=736$ ) and PC 20:1 ( $K_x=915$ ) were obtained.

## **2.1. Introduction**

Biological membranes in living organisms act as structural barriers that maintain the integrity of a cell; they are selective permeability barriers for the passage of molecules in and out of a cell or organelle; they are the site at which a number of important enzymes act; and, in the case of nerve cells, their electrical properties are important for the transmission of information. The physical and chemical properties of biological membranes are of critical importance for understanding specific membrane functions. The structure of the membrane plays an important role in membrane partitioning, insertion and folding of membrane proteins. The study of membranes has been greatly advanced by the development of model bilayer membrane systems that are structurally related to biological membranes (Singer and Nicolson 1972).

Electron spin resonance (ESR) spectroscopy together with nitroxide spin probes and spin labels have enormously contributed to our current understanding of the structure and function of biological and model membranes (Berliner 1976; Marsh and Toniolo 2008). This is because the shape of ESR spectra of such probes is sensitive to the state of the binding of probes, the local polarity and proticity of the environment in which spin probes reside as well as to the molecular motion and orientation of the probes which strongly depend on the local viscosity, structure and dynamics of the environment (Mukai, Lang et al. 1972; Berliner 1976; Polnaszek, Schreier et al. 1978; Marsh 1981; Wisniewska, Widomska et al. 2006). Externally added 2, 2, 6, 6-tetramethylpiperidine-1-oxyl (TEMPO) spin probe (this approach is often called free spin probe approach) is widely used in these studies due to its ability to penetrate into lipid bilayer, providing information about membrane permeability, the phase transitions, spin probe distribution in complex lipid mixtures (Polnaszek, Schreier et al. 1978; Bartucci and Sportelli 1993; Peric, Alves et al. 2005).

Compared e.g. to spin labeled lipids approach, the free spin probe approach has three main advantages. First, a free spin probe can be externally added to the membrane under study at any time. On the contrary, labeled lipids are, in general, incorporated into a lipid bilayer during membrane preparation. Secondly, under physiological conditions the ESR line shape of such free spin probe could be analyzed in terms of the motional narrowing theory (Wilson 1966) making the analysis of ESR spectra simpler. Thirdly, such free spin probes are partitioning between a membrane environment and the aqueous phase surrounding it, providing simultaneous information about both phases. This is possible due to partial resolution of the high field nitrogen hyperfine lines, arising due to different properties of two

environments, which is often observed in ESR spectra at conventional X-band frequencies (Mukai 1972; Schreier, Polnaszek et al. 1978; Bartucci 1993).

Typical continuous wave (cw) X-band ESR spectra of a free spin probe that distributes itself between aqueous and lipid phases is a superposition of two ESR spectra arising from spin probes in two different environments. In most cases such an ESR spectrum is analyzed in terms of a partitioning parameter which is expressed as the ratio of the intensities of the least overlapping high-field lines. The relative intensities of these two lines of the ESR spectra are proportional to the spin probe concentrations in the two phases. This ratio is commonly used for determination of phase transition temperatures, phase diagrams of lipid mixtures and etc (Pringle and Miller 1979; Bartucci and Sportelli 1993; Khulbe, Hamad et al. 2003). In this case only significant changes in ratio of the high field lines amplitudes are considered and interpreted qualitatively. However, the partition coefficient calculated in this manner results in error if differences in activation energies for probe motion in the two media affect the ESR lines differently (Peric, Alves et al. 2005).

In order to improve the resolution and sensitivity of spin probe partitioning ESR different strategies have been employed. One strategy is based on the use of deuterated spin probes, which have narrower lines, but in most of the cases this does not provide full resolution of all three nitrogen hyperfine lines from each phase at X band. The other strategy is to enhance the resolution of X-band ESR by using the second harmonic detection followed by spectral fitting. This strategy was used by (Peric, Alves et al. 2005) and showed some improvement of resolution of two spectral components. Another strategy is to separate components in the X band experimental spectrum with the aid of computer simulations (Stoll and Schweiger 2006). As a result, hyperfine splitting, g-values and correlation time(s) are extracted from simulations of this multicomponent ESR spectrum. However, the quality of parameter determination is rather poor due to the limited sensitivity and resolution of X-band ESR. Moreover, such parameters as correlation time and amount of broadening that are obtained from fitting of the ESR spectra are strongly dependent on the simulation model and these data are not readily comparable.

Dramatic progress in ESR techniques was achieved during the last decade when spectrometers operating at high-field/high frequency (95 GHz and above) became available (Lebedev 1994; Grinberg and Berliner 2004). The advantages of high-field ESR (HF-ESR) are mainly related to the increased electron Zeeman interaction, leading to higher spectral resolution and sensitivity. Thus, two spectral components, i.e. aqueous and lipid, are completely resolved in an experimental spectrum of TEMPO and g-values of each component

can be extracted with high accuracy. Moreover, HF ESR line shapes are sensitive to a different dynamic range than X-band lineshapes. The HF ESR time window is extended to the range of very fast spin probe motion which is irresolvable at X band.

Despite the improved sensitivity and resolution of HF ESR which was demonstrated by Barnes et al (Barnes and Freed 1997) and Smirnov et al (Smirnov 1995) when applied to the study of various spin probes in solution, the application of HF-ESR to the study of free spin probes in lipid bilayers is rather limited (Smirnov 1995). One of the reasons is the sample size limitation, thus, higher concentrations of spin probes are usually used for HF ESR. Subsequently, the increase in spin probe concentration at HF ESR results in a strong effect on the shape of ESR spectrum i.e. leads to enormous line broadening and, therefore, to loss of sensitivity to the  $g$ -tensor and correlation time parameters. Also, the high sensitivity of HF ESR line shapes to the spin probe dynamics (correlation time) results in a large line width and low intensity of the lipid component, leading to a large inaccuracy in the fraction parameter in case of low partition of spin probes in lipid phase. Thus, the best strategy to improve the spin partition approach could be the use of multifrequency ESR, i.e. combining HF ESR (for obtaining accurate values of  $g_{iso}$ ,  $a_{iso}$  and the correlation time) with measurements at lower microwave frequencies (34 and 9 GHz). In this way the whole range of spin probe partition in lipid phase can be studied with the same accuracy and lower concentrations of spin probes can be used.

The primary goal of this work is to explore the factors decreasing the accuracy of the parameters extracted from X-band spectra and the use of the multifrequency ESR approach for improvement of the analysis of X-band data. The secondary goal was to apply the improved X-band analysis procedure to model membrane systems. The ESR spectra from TEMPO spin probe partitioning in model membranes were analyzed in terms of the motional narrowing theory; the Voigt line shape was successfully used for simulations of the ESR spectra obtained at different frequencies. Simulations of High Field ESR spectra of TEMPO partitioning in lipid and aqueous phases resulted in accurate values of  $g_{iso}$  and  $a_{iso}$ , correlation time, line widths and spin probe fraction parameter. In this work the fraction parameters are expressed as lipid or water component intensity normalized to the total ESR spectrum intensity. Thus the sum of lipid fraction and water fractions equals 1. The use of correlation times defined for TEMPO in aqueous and lipid phases from HF ESR for X-band simulations improved the accuracy of lipid/water fraction parameters and made them as accurate as those obtained from the simulations of HF ESR spectra. With this approach even small changes in TEMPO lipid/water fraction parameters could be traced and then turned into biophysical

information about the system, such as changes in the fluidity, structure or polarity profile of the membrane. In the presented work the multifrequency ESR spin probe partitioning approach was applied to the study of model membranes. The TEMPO lipid/water fraction parameter reflected changes in the polarity and structure of the lipid bilayers in the studies of DOPC/DOPG lipids and PC 14:1 and PC 20:1 lipids as a function of lipid concentration. The spin probe mole fraction partition coefficient, which correlates the concentrations of spin probes and lipids with fraction parameter, was computed from the obtained fraction parameters for PC 14:1 and PC 20:1 lipids.

## 2.2. Material and Method

### 2.2.1. Materials

The phospholipids 1,2-dimyristoleoyl-*sn*-glycero-3-phosphocholine (14:1PC), 1,2-dipalmitoleoyl-*sn*-glycero-3-phosphocholine (16:1PC), 1,2-dioleoyl-*sn*-glycero-3-phosphocholine (DOPC, 18:1PC), 1,2-dieicosenoyl-*sn*-glycero-3-phosphocholine (20:1PC) and 1,2-dioleoyl-*sn*-glycero-3-[phospho-*rac*-(1-glycerol)] (DOPG) were obtained from Avanti Polar Lipids (Birmingham, AL, USA). The spin probe 2,2,6,6-tetramethylpiperidine-1-oxyl (TEMPO) was obtained from Sigma-Aldrich. Per-deuterated 2,2,6,6-tetramethylpiperidine-1-oxyl (pd-TEMPO) was obtained from Dr. Igor A. Grigoriev (Institute of Organic Chemistry, Novosibirsk, Russia).

### 2.2.2. Sample preparation

Aliquots of chloroform solutions of DOPC and DOPG were dried under a stream of nitrogen. Residual solvent was removed by evaporation under vacuum for at least a few hours. Vesicle solutions were prepared by re-hydration of the dry lipid film with 10 mM phosphate buffer at pH 7.5 followed by about 30 min vortexing at room temperature. Subsequently, the samples were extruded via a polycarbonate 100 nm filter to prepare homogeneous unilamellar vesicles. Before use the phosphate buffer was bubbled with nitrogen for about 1 hour to partially remove the oxygen. The spin probe pd-TEMPO was added to the vesicle samples prior to the ESR measurements from freshly prepared aqueous stock solutions. To insure a uniform spin probe distribution, the vesicle samples were additionally vortexed for about a few minutes. For multifrequency ESR, the pd-TEMPO concentration was 500  $\mu$ M and the phospholipid concentration was 100 mM.

Lipid concentration dependence experiments were done with the TEMPO spin probe and the phospholipids 14:1, 16:1, 18:1, 20:1 and 22:1PC's. In these experiments, the spin probe concentration was fixed at 100  $\mu$ M and the phospholipid concentration was varied in the range from 7 to 100 mM. ESR samples were prepared as described above.

### 2.2.3. ESR spectroscopy

Room temperature X-band cw-ESR measurements were performed with an Bruker E500 Eleksys SuperX spectrometer equipped with a SHQF resonator (Bruker). Room temperature Q-band cw-ESR measurements were done on a Bruker spectrometer with ER 053 QRD microwave bridge and standard ER 5106 QT resonator. For W-band measurements a homebuilt ESR spectrometer was used (see for example (Brutlach, Bordignon et al. 2006)). Temperature for W band measurements was set to 295 K with an accuracy of 0.5 degree. The X and Q-bands measurements were performed at room temperature (295-297K). The experimental parameters, such as modulation amplitude, microwave power, time constant and scan time were set to avoid disturbance of the ESR spectral shape providing reasonable S/N ratio. The modulation amplitude was set to 0.02-0.05 mT for X-band experiments, and 0.06 mT for Q and W-band spectra. The microwave power was set to 1 mW for the X, Q and W bands spectra. Glass capillaries of 50 $\mu$ l were used for X and Q-band measurements. For W-band experiments quartz capillaries were used.

The correction for the  $g_{iso}$  value of TEMPO in the aqueous and lipid phase was done from Q- and W-bands measurements with a  $^{55}\text{Mn}^{2+}$  ion in Mn/MgO (Burghaus, Rohrer et al. 1992). In the W-band and X-band spectra the aqueous component ( $g_{iso} = 2.00561$ ) was used as a reference.

## 2.3. Theory

### 2.3.1. Calculation of ESR spectral line shapes

When a small, nearly spherical shaped, amphiphilic spin probe, such as pd-TEMPO or TEMPO is added to phospholipid bilayers, it will distribute itself between the lipid and aqueous phases. Since the rotational motion of the spin probe is relatively fast in both phases, the resulting ESR spectrum will be a superposition of two three-line isotropic ESR spectra originating from a spin probe in an aqueous and lipid environment. Positions of ESR lines for such isotropic spectra are characterized by an isotropic  $g$  value,  $g_{iso}$ , and hyperfine splitting,  $a_{iso}$  that are given by:

$$g_{iso} = \frac{1}{3}(g_{xx} + g_{yy} + g_{zz}), \quad (1)$$

and

$$a_{iso} = \frac{1}{3}(a_{xx} + a_{yy} + a_{zz}). \quad (2)$$

Here  $g_{ii}$  and  $a_{ii}$  are the components of the  $\mathbf{g}$  and  $\mathbf{a}$  tensors of the spin probe. As the basic tensor components we used values published previously (Windle 1981):

$$\begin{aligned} g_{xx}^0 &= 2.0087, \quad g_{yy}^0 = 2.0061, \quad g_{zz}^0 = 2.0027, \\ a_{xx}^0 &= a_{yy}^0 = 0.68 \text{ mT}, \quad a_{zz}^0 = 3.0 \text{ mT}. \end{aligned} \quad (3)$$

It is well known that hydrogen bonding and the local solvent polarity influence all the  $\mathbf{g}$  and  $\mathbf{a}$  tensor components of the spin probe but to different extent (Owenius, Engstrom et al. 2001). For lipid/aqueous systems the main effect is visible for the tensor components  $g_{xx}$  and  $a_{zz}$  (Steinhoff 2000; Kurad, Jeschke et al. 2003) (Earle, Moscicki et al. 1994). We take this into account in the following way:

$$\begin{aligned} g_{xx} &= g_{xx}^0 + \Delta g_{xx}, \\ a_{zz} &= a_{zz}^0 + \Delta a_{zz}, \end{aligned} \quad (4)$$

where  $\Delta g_{xx}$  and  $\Delta a_{zz}$  are the corrections to the components induced by environment. The other tensor components are kept the same as in Eq. (3).

In the case of fast isotropic motion with a rotational correlation time  $\tau_R < 10^{-10}$  s (valid for lipid/aqueous systems under physiological conditions) the relaxation leads to the Lorentzian ESR line shapes with linewidth  $\Gamma_m$  (in T) given by (Israelachvili, Sjösten et al. 1975):

$$\Gamma_m = \Gamma_\Gamma + \left[ \frac{4}{45} \left( \frac{h\nu}{\beta_e g_{iso}^2} \Delta g + m \Delta a \right)^2 + \frac{1}{15} \left( \frac{h\nu}{\beta_e g_{iso}^2} \delta g + m \delta a \right)^2 + \frac{3}{8} \left( \frac{4}{45} \Delta a^2 - \frac{1}{15} \delta a^2 \right) [I(I+1) - m^2] \right] \gamma_e \tau_R \quad (5)$$

where

$$\begin{aligned}\Delta a &= a_{zz} - \frac{1}{2}(a_{xx} + a_{yy}), & \Delta g &= g_{zz} - \frac{1}{2}(g_{xx} + g_{yy}), \\ \delta a &= a_{xx} - a_{yy}, & \delta g &= g_{xx} - g_{yy}.\end{aligned}$$

The nuclear quantum states of the nitrogen nucleus (nuclear quantum number  $I = 1$ ) are  $m = 0, \pm 1$ ,  $\gamma_e = 1.760859770 \times 10^{11} \text{ s}^{-1} \text{ T}^{-1}$  is the electron gyromagnetic ratio,  $\nu$  the ESR microwave frequency,  $\beta_e = 9.27400915(23) \times 10^{-24} \text{ J T}^{-1}$  the Bohr magneton, and  $h = 6.62606896(33) \times 10^{-34} \text{ J s}$  Planck's constant.  $\Gamma_r$  is a residual line width, which is assumed to be constant for all three nitrogen hyperfine lines (Israelachvili, Sjösten et al. 1975).

Due to inhomogeneous broadening originating from the presence of oxygen, unresolved hydrogen hyperfine structure, high spin probe concentration, etc., the experimental line shape of the TEMPO spin probes is not purely Lorentzian (Bales, Peric et al. 1998; Bales, Meyer et al. 2008). To take this effect into account, a convolution of Gaussian and Lorentzian functions was used for the lineshape analysis (Israelachvili, Sjösten et al. 1975; Hemminga 1983). For the Gaussian lineshape, we use the linewidth values from Eq. (5). Satellite lines arising from the natural abundance  $^{13}\text{C}$  isotope were also included in the simulation. For this, a splitting constant of 0.58 mT is taken with a 1:1 splitting pattern (Hatch and Kreilick 1972).

The fitting of the model parameters was done using the simplex method (Nelder and Mead 1965) because of its fast convergence. The optimization is navigated by the mean-squared error function. Nine tuning parameters ( $g_{iso}$ ,  $A_{iso}$ ,  $\tau_R$ ,  $\Gamma_r$  for the aqueous and lipid components, and the fraction  $f$ , defined as a ratio of the double integral of the lipid or the aqueous component and the double integral of the total ESR spectrum, were allowed to vary during the optimization.

The correlation between the model's parameters  $a_{iso}$ ,  $g_{iso}$ ,  $\tau_R$ ,  $\Gamma_r$  was tested in the following way. The reference one-component ESR spectra were simulated for X, Q and W-bands using  $\tau_R=70\text{ps}$ ,  $\Gamma_r=0.065\text{mT}$ ,  $a_{iso}=1.60\text{mT}$ ,  $g_{xx}=2.00874$  values. Subsequently, the fitting of each reference spectrum was performed 500 times with random starting parameters. The determined  $a_{iso}$ ,  $g_{iso}$ ,  $\tau_R$ ,  $\Gamma_r$  parameters were checked for linear dependence between them.



## 2.4. Results

Figure 1 shows the room temperature experimental ESR spectra of the pd-TEMPO spin probe in an aqueous solution of 18:1PC vesicles at X (9.4 GHz), Q (34 GHz) and W-band (95 GHz). As was mentioned above, the ESR spectra consist of two spectral components due to the spin probe located in two different environments: lipid and water environment. At the X-band (Fig. 1a) the ESR spectra arising from the spin probe in different environment are only partly resolved (see high field component). The effect of the surrounding environment is only detectable at the high-field nitrogen hyperfine line, where the combined effect on  $g_{xx}$  and  $a_{zz}$  and, thus, on  $g_{iso}$  and  $a_{iso}$  is most pronounced and lines are partially resolved. When increasing the microwave frequency to the Q-band the spectral resolution due to  $g_{iso}$  increases (Fig. 1b) and at the W-band (Fig. 1c) both spectral components are fully resolved. The spectral component with the smaller hyperfine splitting is assigned to the spin probe in the lipid phase, whereas the outer spectral lines with higher hyperfine splitting arise from spin probes in the aqueous phase (Figure 1). In addition to spectral shift, the two spectral components have pronounced difference in line intensities and line width. This is because of the rotational motion of the spin probe in the lipid phase is slower as compared to the aqueous phase, its ESR spectral components are more broadened and consequently reduced in intensity. This broadening effect becomes even stronger at increasing ESR frequencies, because the  $\mathbf{g}$  tensor and correlation time contribution increases with microwave frequency  $\nu$  (see Eq. 5).

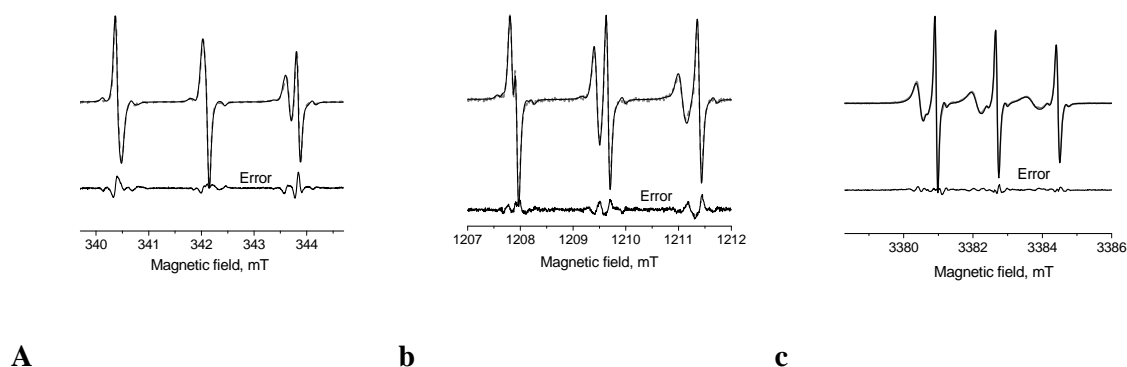


**Figure 1.** Room temperature ESR spectra of the spin probe pd-TEMPO in aqueous solution of DOPC vesicles at X (a), Q (b) and W-bands (c). The spin probe concentration was 500  $\mu\text{M}$  and the lipid concentration 100 mM. The experimental spectrum (grey line) is shown together with the simulated spectrum (solid black line). The residual plot is the difference between the experimental and simulated spectra (solid 'error' line). At each frequency, all spectra are plotted on the same vertical scale

SBF was used to separate the two components in the experimental ESR spectra in Fig. 1. The quality of the fits, as shown by the residuals between experimental and simulated spectra, is improving at higher microwave frequency. In general the simulated spectra at all three microwave frequencies are in a good agreement with the experimental ones, indicating that the isotropic motional narrowing approach in Eq. (5) can be used for the simulation of multifrequency ESR spectra of a free spin probe in water/lipid mixtures. From the fitting we get the  $a_{iso}$ ,  $g_{iso}$ ,  $\tau_R$ ,  $\Gamma_I$  and the fraction  $f$  for lipid and aqueous components.

**Table 1** Estimated parameters for the aqueous and lipid components in the ESR spectra (500  $\mu$ M pd-TEMPO in an aqueous 100 mM DOPC vesicle solution) recorded at X (9.4 GHz), Q (34 GHz) and W(95 GHz)-band at room temperature. The sensitivity of the parameters was estimated using multiple fitting with random starting estimations.

Tuning parameters	X-band		Q-band		W-band	
component	Water	DOPC	Water	DOPC	Water	DOPC
$\tau_R$ (ps)	8 -60*	70 $\pm$ 50	5-20*	60 $\pm$ 15	6.3 $\pm$ 0.5	61 $\pm$ 2.5
$g_{xx}$ ( $g_{iso}$ )***	2.0082 (2.0056)	2.0088 (2.0057)	2.00827 (2.00560)	2.00878 (2.00577)	2.00827 (2.00560)	2.00881 (2.00578)
$a_{iso}$ (mT)	1.70	1.60	1.71	1.59	1.72	1.59
$f$	0.49 $\pm$ 0.05 (0.45 $\pm$ 0.01)**	0.51 $\pm$ 0.05 (0.55 $\pm$ 0.01)**	0.42 $\pm$ 0.03 (0.45 $\pm$ 0.01)**	0.58 $\pm$ 0.03 (0.55 $\pm$ 0.01)**	0.44 $\pm$ 0.01	0.56 $\pm$ 0.01

\* exact values were not defined due to the large inaccuracy.

\*\* values obtained from simulation of X and Q-band spectra with predefined  $\tau_R = 6.3$  ps and  $\tau_R = 61$  ps for aqueous and lipid components, respectively.

\*\*\*  $g_{iso}$  is calculated based using equation (1) with obtained  $g_{xx}$  and  $g_{yy}^0 = 2.0061$ ,  $g_{zz}^0 = 2.0027$ .

As the next step the correlation between the model's parameters  $a_{iso}$ ,  $g_{iso}$ ,  $\tau_R$ ,  $\Gamma_I$  was tested. Among the determined  $a_{iso}$ ,  $g_{iso}$ ,  $\tau_R$ ,  $\Gamma_I$  parameters (all found solutions have the same goodness of fit) for X, Q and W-band, a correlation was found only between  $\tau_R$  and  $\Gamma_I$  (Fig. 2). It is clear from Fig.2 that the range of correlation between  $\tau_R$  and  $\Gamma_I$  decreases at increased frequency, due to the increasing contribution from  $\tau_R$  to the linebroadening (Eq. 5). Thus, at W-band the correlation between parameters becomes negligible and accurate values of  $\tau_R$  and  $\Gamma_I$  are determined.

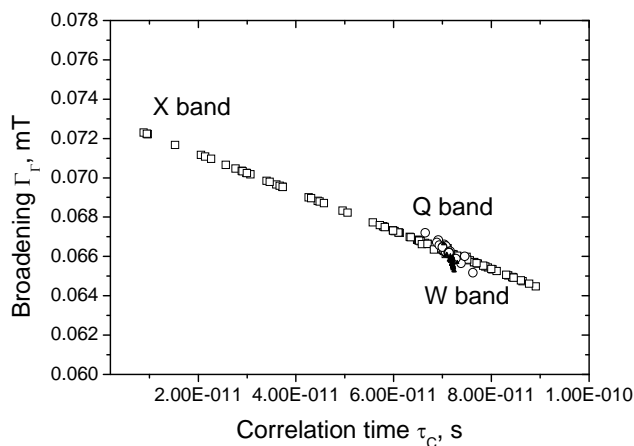


**Figure 2.** Line broadening parameter ( $\Gamma_{\Gamma}$ ) versus correlation time ( $\tau_R$ ) obtained from fitting of a reference spectrum at X, Q and W-band. The reference one component spectra at X, Q and W-bands were calculated using  $\tau_R = 70$  ps,  $\Gamma_{\Gamma} = 0.065$  mT,  $a_{iso} = 1.60$  mT,  $g_{xx} = 2.00874$  values. The reference spectra at each frequency were fitted 500 times with random starting parameters.

Figure 3 shows spectra of pd-TEMPO spin probe in an aqueous solution of DOPC and DOPG vesicles at X (a), Q(b) and W-band (c). A higher partitioning of the spin probes into the lipid phase of DOPG than of DPC is observed. In addition, the polarity effect of the charged DOPG headgroups environment on the  $g_{iso}$  value of spin probe results in a shift of the Q and W-band spectrum of the lipid component to higher field (Fig. 3 b,c). All spectra are normalized using reference ESR spectra of spin probe in aqueous phase.

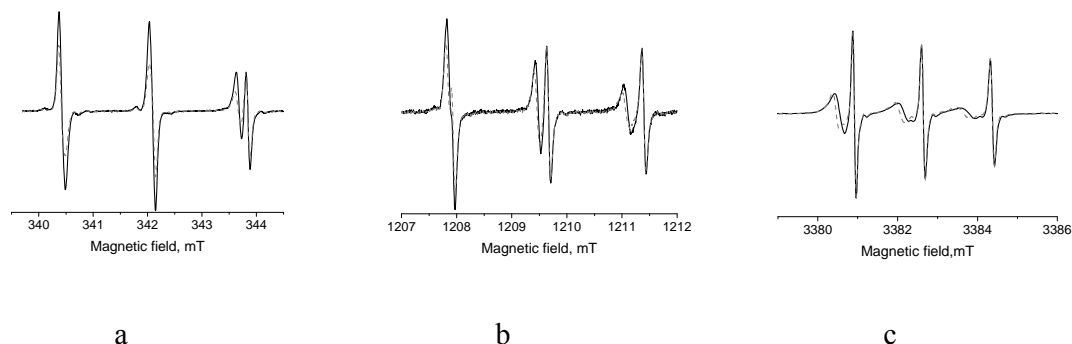


**Figure 3.** ESR spectra of 500  $\mu$ M pd-TEMPO in a 100 mM aqueous solution of DOPC (dotted line) and DOPG (solid line) vesicles at X- (9.5GHz), Q- (34GHz) and W-band (95GHz) at 293 K. Spectra are normalized to the aqueous component.

Parameters extracted from X-, Q- and W-band spectra of pd-TEMPO in aqueous solutions of DOPC and DOPG are summarized in Table 1 (DOPC) and Table 2 (DOPG).

In order to improve the accuracy, the X and Q-band spectra from pd-TEMPO in aqueous solutions of DOPG and DOPG were simulated with  $\tau_R = 62$  ps for the lipid and  $\tau_R = 6$  ps for the aqueous component as obtained from SBF of the W-band spectrum. The obtained fraction coefficients are summarized in brackets in the last row of Table 1 (DOPC) and Table 2 (DOPG). Clearly, the use of reference parameters ( $\tau_R$ ) determined from HF ESR increases the accuracy of the parameters obtained from the X and Q-band, because the optimization routine can now find the global minimum of the error function.

**Table 2** Estimated parameters for the aqueous and lipid component in the ESR spectrum (500  $\mu$ M pd-TEMPO in a 100 mM aqueous solution DOPG vesicles). Spectra are recorded at the X, Q and W-bands at 293K. The sensitivity of the parameters was estimated using multiple fitting with random starting estimations.

Tuning parameters	X-band		Q-band		W-band	
component	Water	DOPG	Water	DOPG	Water	DOPG
$\tau_R$ (ps)	7-50*	55 $\pm$ 50	6-28*	50 $\pm$ 15	6.2 $\pm$ 0.5	65 $\pm$ 2.5
$a_{iso}$ (mT)	1.70	1,60	1.71	1,60	1.72	1,60
$g_{xx}$ ( $g_{iso}$ )***	2.0082 (2.0056)	2,0087 (2.0057)	2.00827 (2.00560)	2,00873 (2.00574)	2.00827 (2.00560)	2,00874 (2.00575)
$f$	0.4 $\pm$ 0.1 (0.36 $\pm$ 0.01)**	0.6 $\pm$ 0.1 (0.64 $\pm$ 0.01)**	0.43 $\pm$ 0.03 (0.37 $\pm$ 0.01)**	0.57 $\pm$ 0.03 (0.63 $\pm$ 0.01)**	0.35 $\pm$ 0.01	0.65 $\pm$ 0.01

\* exact values were not defined due to the large inaccuracy. The ranges of possible values were estimated after 10 fittings with random start parameters.

\*\* values obtained from simulation of X and Q-band spectra with predefined  $\tau_R = 6.3$  ps and  $\tau_R = 6.1$  ps for aqueous and lipid components, respectively.

\*\*\*  $g_{iso}$  is calculated based using equation (1) with obtained  $g_{xx}$  and  $g_{yy}^0 = 2.0061$ ,  $g_{zz}^0 = 2.0027$ .

X-band ESR spectra of the TEMPO spin probe in 14:1PC are shown in Fig. 4. In this experiment, the phospholipid concentration was changed at a fixed spin probe concentration of 100  $\mu$ M. As can be observed at the high-field nitrogen hyperfine line, the lipid component increases upon increasing the phospholipid concentration. A similar behavior is observed for TEMPO in 20:1 and other PCs (spectra not shown).

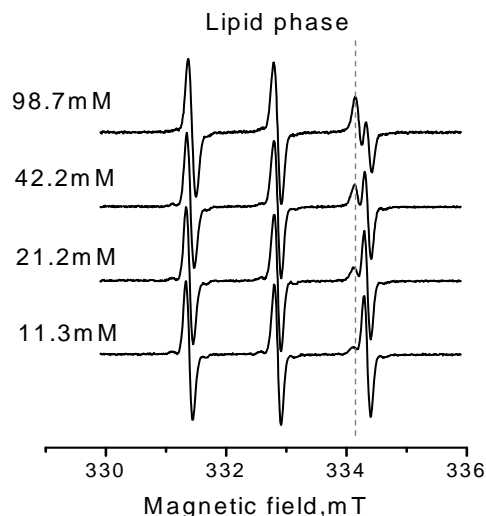


**Figure 4.** X-band ESR spectra of TEMPO in PC 14:1 with different lipid concentration in mM, *pd*-TEMPO concentration was fixed to 100  $\mu$ M. Experiments were performed at room temperature.

Figure 5 shows the fraction of TEMPO in the lipid phase as a function of the phospholipid concentration. Fig. 5a and 5b show the results of analysis with no restrictions and with the fixed values  $\tau_{\text{Rwater}}=6.3 \times 10^{-12}$  s and  $\tau_{\text{Rlipids}}=6.1 \times 10^{-11}$  s, respectively. The error bars indicate the inaccuracy in the obtained parameter as a result of 10 fits of the ESR spectrum with random starting parameters. The fraction coefficient ( $f$ ) of spin probes in the lipid phase as a function of phospholipid concentration was described previously with the following equation (White, Wimley et al. 1998; Santos, Prieto et al. 2003).

$$K_x = \frac{[P_{bil}]/([L] + [P_{bil}])}{[P_{water}]/([W] + [P_{water}])} \quad (6)$$

where  $K_x$  is the mole fraction partition coefficient,  $[W]$  and  $[L]$  are the molar concentrations of water and lipid,  $[P_{bil}]$  and  $[P_{water}]$  are the bulk molar concentrations of the spin probe in the bilayer and aqueous phases, respectively, thus  $[P_{total}] = [P_{bil}] + [P_{water}]$ . Eq.(6) assumes that all lipids in the bilayers vesicles are accessible to the spin probe. Because (i) under most experimental conditions  $[W] = 55.3 \text{ M} \gg [P_{water}]$  and (ii)  $[L] \gg [P_{bil}]$ , to avoid concentration-dependence effects on partition coefficients Eq.(6) can be simplified to Eq.(7):

$$f_{lipid} = \frac{K_x [L]}{[W] + K_x [L]} \quad (7)$$

where  $f_{lipid}$  is the fraction of the spin probe in the lipid phase.  $K_x$  can be determined by least-squares fitting of Eq. (7) to plots of  $f_{lipid}$  against  $[L]$  (Fig. 5b).

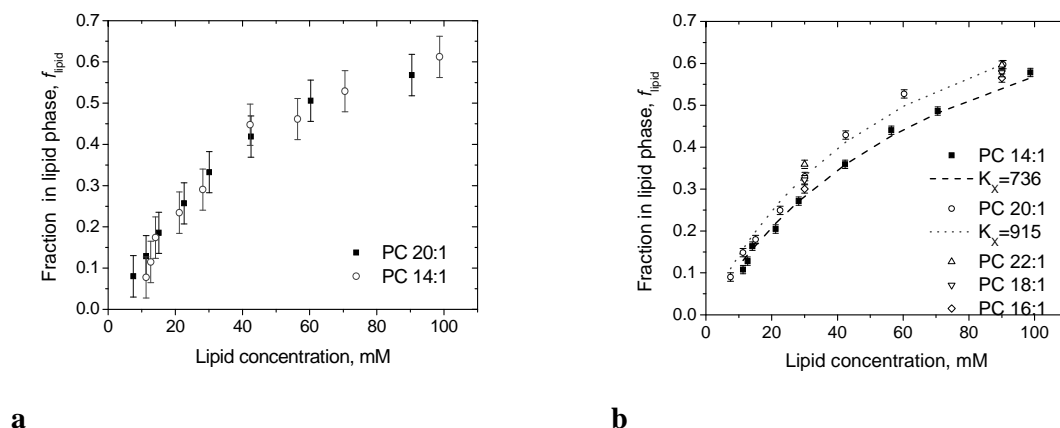


**Figure 5.**  $f_{lipid}$  as a function of lipid concentration for lipids with different acyl chain lengths: PC 14:1 and 20:1. TEMPO concentration was 100  $\mu$ M. Additionally, 30 mM and 90 mM concentrations of PC 20:1 (triangles), PC 18:1 (triangles) and PC 16:1 (diamonds) were used.  $f_{lipid}$  was obtained from simulations with no restrictions of the parameters (a) and simulations with fixed correlation time values (b). Dashed lines - least square fitting of the fraction dependence with Eq.(7) using  $K_x = 915$  for PC 20:1 and  $K_x = 736$  for PC 14:1.

## 2.5. Discussion

The physical and chemical properties of biological membranes are of critical importance for understanding specific membrane functions. The structure of the membrane plays an important role in membrane partitioning, insertion and folding of membrane proteins. The transport of solutes across membranes is highly important for the functioning of a biological cell, and knowledge about their properties can be of help for developing drug delivery systems etc. X-band ESR in general and the partitioning technique in particular have become standard techniques to study membrane structure and functioning (Severcan and Cannistraro 1988; Severcan, Acar et al. 1997; Peric, Alves et al. 2005). One of the main reasons why application of X-band ESR to the study of membranes has become so popular is that all measurements can be done under physiological conditions. Increasing of the sensitivity of X-band partitioning ESR has primary importance for such studies. Although the application of high field ESR (95GHz and higher) improves the resolution drastically, this approach has some drawbacks. High field spectrometers are not yet available for routine and fast measurements, which would be needed for studying membrane structure and functions

under physiological conditions. However, high field ESR provides a pronounced improvement of reference measurements (Smirnov, Smirnova et al. 1995). High-field ESR requires some specific conditions/restrictions for measurements and sample preparation, such as limited sample size, very high concentrations of spin probe, etc.

The goal of the current work is to develop a new and simple approach: combining high field ESR advantages for reference measurements with X-band partitioning ESR for fast, routine measurements under physiological conditions. To increase the sensitivity of X-band ESR and improve the accuracy of the parameters determined using routine X-band ESR, mathematical simulations were done using constraints for some of the parameters determined with high accuracy from reference measurements at high field ESR.

### 2.5.1. Mathematical model for spectrum simulations

The fits of ESR spectra presented in Fig. 1 allow the extraction of the fraction coefficient  $f$  for the pd-TEMPO and TEMPO spin probes in the lipid ( $f_{lipid}$ ) and the aqueous phase ( $f_{water}$ ). In addition, the isotropic tensor values  $g_{iso}$  and  $a_{iso}$  are obtained that are related to the local polarity/proticity of the environment and the values of the isotropic rotational correlation times  $\tau_R$  that reflect the local viscosity. The parameters obtained from the fitting are summarized in Table 1. Clearly, the accuracy of the data obtained at the X-band is low; however, at the W-band the quality of the parameters is far better. In the first place, this is due to the features of the W-band spectral line shape, allowing an accurate fit. The introduced mathematical model uses an independent line width calculation for the  $m=0, \pm 1$  states of the nitrogen nucleus, based on values of the complete  $a$  and  $g$ -tensors and the correlation time of the isotropic rotation. Changes in  $a_{iso}$  and  $g_{iso}$  are reflected in both the position and line shapes of the individual lines (line amplitude and width). For X-band ESR detectable changes in the line shapes due to e.g. the  $\Delta g_{iso}$  value lie in a range of  $\pm 0.001$ , whereas at W-band line shapes reflect the changes as small as  $\Delta g_{iso} = \pm 0.0001$ , when the  $g_{xx}$  component is varied. Variation of  $g_{yy}$ ,  $g_{zz}$ ,  $a_{xx}$ ,  $a_{yy}$  in the range of  $[\pm 0.001]$  and  $[\pm 0.04G]$  respectively have no effect on line shape and fitting accuracy for the X, Q and W-bands. Therefore, they were kept constant during the simulations.

It is clear from the results of computer simulations that the accuracy of the parameter determination strongly depends on the correlation between the parameters that describe the spectral line broadening, i.e., the rotational correlation time  $\tau_R$  and the residual line width  $\Gamma_r$  (see Eq. 5). For this reason, we assume that the basic line shape of the ESR spectra is given by a Lorentzian/Gaussian convolution function that is determined only by one line-width

parameter, given by Eq. (5). However, in fitting synthesized model spectra, we see that even for a single spectral component at the X-band,  $\tau_R$  and  $\Gamma_r$  are strongly correlated (Fig 2), leading to large errors in the determination of  $\tau_R$  (obtained values range from 9 to 90 ps). At the W-band this correlation is almost gone (Table 3) (obtained values range from 70 to 72 ps). This is due to the fact that the contribution of  $\Gamma_r$  in Eq. (5) becomes smaller at increasing frequencies, and the line broadening of the three ESR lines turns out to be more strongly dependent on  $m$  and  $\tau_R$ . The correlation between  $\tau_R$  and  $\Gamma_r$  decreases the accuracy of the fraction parameter, especially for the simulation of X band spectra ( $\pm 0.1$ , *f* Table 1). It is obvious that such a low sensitivity will affect the quality of the parameters determined with X-band ESR.

**Table 3.** Range of obtained values of the correlation time ( $\tau_R$ ) and the line broadening ( $\Gamma_r$ ) parameters, reflecting the correlation between these parameters in the fitting procedure. Reference one component spectra at X, Q and W-band were calculated using  $\tau_R = 70$  ps,  $\Gamma_r = 0.065$  mT,  $a_{iso} = 1.60$  mT, and  $g_{xx} = 2.00874$ . The range of the parameters was estimated using 500 fits with random starting estimations

	X band	Q band	W band	Reference
Correlation time ( $\tau_R$ ) ps	8.8-89	66 - 77	70 - 72	70
Broadening ( $\Gamma_r$ ), mT	0.064 – 0.072	0.065 – 0.067	0.064 – 0.066	0.065

A direct conclusion from these observations is that the determination of spin probe partition coefficients and  $\tau_R$  in X- and Q-band spectra will lead to large errors and that only at high-field ESR accurate values can be obtained. However, the limitations of HF ESR measurements at physiological conditions, such as sample size and increased concentration of spin probes, restrict its application to routine measurements. On the contrary, the X-band ESR has been well developed and is more suitable for the spin probe ESR approach, but its drawback is the lower sensitivity and resolution for  $g_{iso}$  and correlation time parameters. The combination of HF and X-band ESR is needed to study a membrane under physiological conditions. In this approach HF ESR should be applied to one particular “reference” sample with optimal concentration and ratio of the spin probe in the lipid and aqueous solution, resulting in the determination with high accuracy of the correlation time,  $g_{iso}$  and  $a_{iso}$  parameters. The reference HF ESR measurement has to be done only once for a particular lipid and/or solvent in order to characterize the parameters in this particular system. Subsequently, the set of measurements (at physiological conditions) can be done at X or Q-bands and then fitting is performed using relevant parameter values that were obtained from reference HF ESR measurements.



### 2.5.2. Simulations of High Field spectra

From the analysis of the W-band spectrum of pd-TEMPO, a correlation time of  $\tau_R = 6$  ps in an aqueous environment (Table 1) is determined. This is in good agreement with already published values (Jolicoeur and Friedman 1978). This value is also similar to a rotational correlation time of 10 ps estimated for pd-TEMPO in aqueous environment by the modified Stokes-Einstein equation (Roozen and Hemminga 1990).

The correlation time of pd-TEMPO in the lipid phase ( $\tau_R = 61$  ps) is in the range of previously reported values of TEMPO in various lipid systems [20 – 80 ps] (Jolicoeur and Friedman 1978; Smirnov, Smirnova et al. 1995; Paktas and Sünnetçioğlu 2007). It is important to note that the value of  $\tau_R$  of the lipid component obtained from the 34-GHz simulations is close to the one obtained from the 94-GHz simulations (see Table 1), even with the existing correlation between the parameters in the model. However, the value of  $\tau_R$  of the lipid component obtained from Q-band has a lower accuracy ( $\pm 15$  ps) than the one obtained from W-band ( $\pm 2.5$  ps). This demonstrates once more the importance of a proper combination of multifrequency ESR to study the partitioning of the spin probe in the lipid and aqueous phase and to characterize the lipid and aqueous environment based on the dynamics of the spin probe.

The spin probe rotates with the same rate in both DOPC and DOPG lipid ( $\tau_R = 2.8 \times 10^{-11}$  s, Table 2) indicating a similar local environment/space that is available for the motion. From W-band simulations, pd-TEMPO in DOPG lipids has lower values for  $g_{xx}$  (2.00874) and higher  $a_{iso}$  (1.6 mT) and pd-TEMPO in DOPC has higher a value for  $g_{xx}$  (2.00881) and a lower one for  $a_{iso}$  (1.59 mT). This is in agreement with results from earlier studies of the correlation between  $g_{iso}$  and  $a_{iso}$ . It has been reported that  $g_{xx}$  decreases and  $a_{zz}$  increases at increasing solvent polarity (Owenius, Engstrom et al. 2001; Marsh and Toniolo 2008). The difference in the values determined for  $g_{xx}$  and  $a_{zz}$  indicates a more polar environment for the pd-TEMPO spin probe in DOPG lipids. Dielectric constants near the headgroup region of lipid vesicles have been reported for DOPC ( $\epsilon = 14.0$ ) and a DOPC/DOPG mixture ( $\epsilon = 18.2$ ) (Koehorst, Spruijt et al. 2004). On the contrary, no difference in the polarity ( $\epsilon$ ) was reported for the center of these lipid bilayers (dielectric constant  $\epsilon = 2$  (Koehorst, Spruijt et al. 2004)). Therefore, if the spin probe would be located in the center region of the lipid bilayer, no difference in the  $g_{xx}$  values would be expected for DOPC and DOPG vesicles. Thus, the most probable location of the nitroxide group of TEMPO is close to the lipid headgroup area.

Finally, our data clearly indicate that the spin probe partitioning is larger in DOPG than in DOPC vesicles for the given spin probe and lipid concentrations (Table 1 and 2). This observation, as well as the lower polarity for DOPC head-groups, is consistent with the relatively strong repulsion between the charged DOPG head-groups which results in a larger area per molecule than for DOPC (areas per lipid molecule are  $0.72 \text{ nm}^2$  (Tristram-Nagle, Petrache et al. 1998) and  $0.80 \text{ nm}^2$  for DOPC and DOPG, respectively), and therefore DOPG could provide more free space for TEMPO molecules in these vesicles than in DOPC. The location of the spin probe near the headgroup region and a higher fraction of spin probes in DOPG than in DOPC vesicles due to bigger area per lipid were also reported before for DTNB spin probes (Peric, Alves et al. 2005).

### 2.5.3. Analysis of X band spectra.

The shape of the ESR spectrum of a nitroxide spin probe at X-band frequency is sensitive to re-orientational motions with correlation times of 100 ps to 200 ns (Beier and Steinhoff 2006). As discussed above, both components of the lipid/aqueous system at room temperature are not within the X-band EPR time window. This results in the strong correlation between the rotational correlation time ( $\tau_R$ ) and the line broadening parameters ( $\Gamma_I$ ), and leads to a large inaccuracy for the calculated value of  $f_{lipid}$  (Table 1,2,3). In general, correlated parameters in the model lead to infinite number of solutions with the same goodness of fit (i.e. multiple local minima are found), and the obtained values for these parameters are strongly dependent on the starting values in the fits.

Simulations of the X-band spectra for the DOPC and DOPG lipid/aqueous systems were most of the time satisfactory, but the fraction parameter obtained from the X-band simulations has a lower accuracy ( $\pm 0.05$ ) than the one obtained from the W-band ( $\pm 0.01$ ) (Table 1 (DOPC), Table 2 (DOPG)). Moreover, the accuracy of the obtained correlation time ( $\tau_R$ ) for the aqueous and lipid phase components is very low. Slightly better results were obtained from simulations of the Q-band spectra (Table 1 – DOPC, Table 2 -DOPG), but the values of  $f_{lipid}$  and  $f_{water}$  as well as  $\tau_R$  for the aqueous component are still inaccurate and vary from those obtained from the W-band.

When analyzing the X-band spectra from TEMPO in PC 14:1 and 20:1 lipids using a model with no restrictions for the parameters, we obtained  $f_{lipid}$  as a function of lipid concentration as indicated in Figure 5a.  $f_{lipid}$  increases with lipid concentration for both types of lipids and no significant difference was observed for PC 14:1 and 20:1 due to the large error margins. However, it has been reported (Wimley and White 1993) that the structure of

the lipid bilayer could play a major role in partitioning and changes in the thickness and area per lipid could affect the spin probe partitioning. Therefore, one might expect differences in partitioning in both cases.

If we now use the results obtained from the HF W-band ESR to improve the accuracy of the analysis of the X-band spectra, the error in the parameters can significantly be reduced. Only one HF “reference” measurement is needed, resulting in an accurate value for the line broadening parameter  $\Gamma_r$ . If we now analyze the effect of lipid concentrations on TEMPO partitioning in PC 14:1 and PC 20:1 using  $\tau_{\text{Rwater}}=6.3 \times 10^{-12}\text{s}$  and  $\tau_{\text{Rlipids}}=6.1 \times 10^{-11}\text{s}$  (values obtained from W-band spectrum of pd-TEMPO in DOPC at room temperature) an accuracy of  $\pm 0.01$  for the fraction parameter is obtained (previously it was  $\pm 0.05$  when no HF ESR parameters were used), which is comparable to the accuracy of the W-band analysis (Figure 5b). Even though the difference in partitioning of TEMPO in the lipid phase for short and long lipids is very small, about 5% as determined from our study, our simulations of X-band spectra with fixed (determined from “reference” HF-ESR)  $\tau_R$  for aqueous and lipid components clearly indicate that the partitioning of TEMPO in PC 20:1 lipids is higher than in PC 14:1 for the whole range of lipid concentrations. Moreover, additional experiments with PC 16:1, PC 18:1 and PC 22:1 show the same trend of increasing partitioning of spin probes in the lipid phase when the lipid length is increased (Fig 5 b,  $\Delta$  PC 16:1,  $\blacktriangledown$  PC 18:1 and  $\diamond$  PC 22:1 ). Accurate values of the fraction parameter  $f$  extracted from X-band spectra also allow the determination of the mole fraction partition coefficients (cf. Eq. 7) of TEMPO in PC 20:1 (915) and PC 14:1 (736). The mole fraction partition coefficient  $K_x$  of TEMPO together with Eq. 7 determine the fraction of TEMPO in lipids for arbitrary lipid concentrations. Thus, the fraction coefficient determined from the experiment could always be compared with the theoretical one from Eq. 7 and their difference reflects the changes in the lipid bilayer structure. This is potentially important for spin probe ESR studies of interactions between lipid bilayers and peptides, which are influencing the properties of the lipid bilayer and, therefore, and these changes are also expected to be reflected in changes of the spin probe fraction coefficients (Srivastava, Phadke et al. 1989).

The larger value of  $K_x$  for PC 20:1 is quite an interesting observation, since higher partitioning in these lipids is not correlated with the area per lipid. At a fixed temperature, the area per lipid slightly decreases with increasing acyl chain length, indicating an increased Van der Waals attraction for longer lipid chains (Peric, Alves et al. 2005). Comparing PC 20:1 and PC 14:1, the expected decrease in thickness of the lipid bilayer could be about 12 Angstrom, whereas the increase in area per lipid is  $0.02 \text{ nm}^2$  (Yuan 2007), which should lead to a lower

fraction,  $f_{lipid}$ , of TEMPO in PC 20:1 than in PC 14:1 lipids. Generally, the molecular mechanisms that account for the partitioning of the molecules between the aqueous and the lipid phase are rather complex (Wimley and White 1993) and not well understood. Thus, the driving forces for partitioning of TEMPO in the lipid phase could be not only the lipid bilayer structure, but also the hydrophobic effects of the polarity of the spin probe (TEMPO is a more apolar molecule with a higher chemical affinity for hydrophobic solvent than for example 4-oxo-2, 2, 6, 6-tetramethyl-1-piperidinyloxy, thus TEMPO has higher partitioning in the same type of the membranes) (Buitink, Leprince et al. 2000). Partitioning of TEMPO in PC 20:1 is preferable due to a slightly higher dielectric constant next to the headgroup ( $\epsilon = 12$ ) than in the case of PC 14:1 ( $\epsilon = 11.8$ ) (Koehorst, Spruijt et al. 2004). However, the understanding of this effect will require additional experiments and results will be published later.

Routine X-band measurements with a proper high field reference measurement, can drastically improve the sensitivity of the partitioning technique and can be used e.g. to study lipid-peptide and lipid-protein interactions, drug delivery systems, and the stability of model and physiological membranes.

## 2.6. Conclusions

We have shown that model membranes can be studied with small spin probes at X-band leading to high-precision values of the ESR parameters. The new approach consists of a combination of routine low-frequency (9 GHz, X-band) and accurate high-frequency (94 GHz, W-band) reference measurements and spectral fitting with fixed correlated parameters. This approach can be used for spin probe partitioning studies, which can be very useful in the description of changes in structural properties of phospholipid vesicles. The use of spectra at high frequency (94 GHz) greatly improves the precision in the determination of the values for the rotational correlation time and  $g_{iso}$ . Spectral fitting with the presented model and input values of  $\tau_R$  from the high-frequency measurements, as expected, greatly improves the precision of the partition coefficient extracted from the X-band spectra. Based on  $f_{lipid}$  the mole fraction partition coefficients for TEMPO in PC 20:1 and PC 14:1 were calculated. The method of X-band spectra simulations with parameters obtained from HF ESR can be applied in many other cases as long as a suitable small probe can be found and measured at high frequency in desired experimental conditions.

## ACKNOWLEDGMENTS

We thank Marcus A. Hemminga for valuable discussion about membranes and spin probes.

## REFERENCES

- Bales, B. L., M. Meyer, et al. (2008). "EPR line shifts and line shape changes due to spin exchange of nitroxide-free radicals in liquids 4. Test of a method to measure re-encounter rates in liquids employing  $^{15}\text{N}$  and  $^{14}\text{N}$  nitroxide spin probes." J. Phys. Chem. A **112**(11): 2177-2181.
- Bales, B. L., M. Peric, et al. (1998). "Contributions to the gaussian line broadening of the proxyl spin probe EPR spectrum due to magnetic-field modulation and unresolved proton hyperfine structure." J. Magn. Reson. **132**(2): 279-286.
- Barnes, J. P. and J. H. Freed (1997). "Aqueous sample holders for high-frequency electron spin resonance." Rev. Sci. Instrum. **68**(7): 2838.
- Bartucci, R. and L. Sportelli (1993). "ESR investigation on the phase transitions of DPPC vesicles in presence of high concentration of  $\text{Li}^+$ ,  $\text{Na}^+$ ,  $\text{K}^+$  and  $\text{Cs}^+$ ." Colloid Polym. Sci. **271**(23): 262-267.
- Bartucci, R., Sportelli, L. (1993). "ESR investigation on the phase transitions of DPPC vesicles in presence of high concentration of  $\text{Li}^+$ ,  $\text{Na}^+$ ,  $\text{K}^+$  and  $\text{Cs}^+$ ." Colloid Polym. Sci. **271**: 262-267.
- Beier, C. and H.-J. Steinhoff (2006). "A structure-based simulation approach for Electron Paramagnetic Resonance spectra using molecular and stochastic dynamics simulations." Biophys J. **91**(7): 2647-2664.
- Berliner, L. J. (1976). Spin labeling : theory and applications / edited by Lawrence J. Berliner. New York :, Academic Press.
- Brutlach, H., E. Bordignon, et al. (2006). "High-field EPR and site-directed spin labeling reveal a periodical polarity profile: The sequence 88 to 94 of the Phototransducer NpHtrII in complex with Sensory Rhodopsin, NpSRII." Appl. Magn. Reson. **30**: 359-372.
- Buitink, J., O. Leprince, et al. (2000). "Dehydration-Induced Redistribution of Amphiphilic Molecules between Cytoplasm and Lipids Is Associated with Desiccation Tolerance in Seeds." Plant Physiol. **124**: 1413-1426.
- Burghaus, O., M. Rohrer, et al. (1992). "A novel high-field/high-frequency EPR and ENDOR spectrometer operating at 3 mm wavelength." Meas. Sci. Technol. **3**: 765-774.
- Earle, K. A., J. K. Moscicki, et al. (1994). "250-GHz Electron Spin Resonance studies of polarity gradients along the aliphatic chains in phospholipid membranes." Biophys. J. **66**: 1213-1221.

- Grinberg, O. and L. J. Berliner (2004). Very High Frequency (VHF) ESR/EPR. New York, Kluwer/Plenum Publishers.
- Hatch, G. F. and R. W. Kreilick (1972). "NMR of some nitroxide radicals:  $^{13}\text{C}$  coupling constants." J. Chem. Phys. **57**(9): 3696-3699.
- Hemminga, M. A. (1983). "Interpretation of ESR and saturation transfer ESR spectra of spin labeled lipids and membranes." Chem. Phys. Lipids **32**: 323-383.
- Israelachvili, J., J. Sjöstén, et al. (1975). "ESR spectral analysis of the molecular motion of spin labels in lipid bilayers and membranes based on a model in terms of two angular motional parameters and rotational correlation times." Biochim. Biophys. Acta **382**(2): 125-141.
- Jolicoeur, C. and H. L. Friedman (1978). "ESR lineshapes and kinetic behavior of nitroxide spin probes in micellar solutions." J. Solution Chem. **7**(11): 813-835.
- Khulbe, K. C., F. Hamad, et al. (2003). "ESR spectra of spin probe in PPO membrane." Polymer **44**: 695-701.
- Koehorst, R. B. M., R. B. Spruijt, et al. (2004). "Lipid Bilayer Topology of the Transmembrane  $\alpha$ -Helix of M13 Major Coat Protein and Bilayer Polarity Profile by Site-Directed Fluorescence Spectroscopy." Biophys. J. **87**(3): 1445-1455.
- Kurad, D., G. Jeschke, et al. (2003). "Lipid membrane polarity profiles by high-field EPR " Biophys. J **85**: 1025-1033.
- Lebedev, Y. (1994). "Very-high-field EPR and its applications." Appl. Magn. Reson. **7**(2): 339-362.
- Marsh, D. (1981). Electron spin resonance: spin labels. Berlin, Springer.
- Marsh, D. and C. Toniolo (2008). "Polarity dependence of EPR parameters for TOAC and MTSSL spin labels: Correlation with DOXYL spin labels for membrane studies." J. Magn. Reson. **190**(2): 211-221.
- Mukai, K., C. M. Lang, et al. (1972). "A spin label investigation of some model membrane systems." Chem. Phys. Lipids **9**(3): 196-216.
- Mukai, K., Lang, C. M., Chesnut, D. B. (1972). "A spin label investigation of some model membrane systems." Chem. Phys. Lipids **9**: 196-216.
- Nelder, J. A. and R. Mead (1965). "A simplex method for function minimization." Comp. J. **7**(4): 308-313.
- Owenius, R., M. Engström, et al. (2001). "Influence of solvent polarity and hydrogen bonding on the EPR parameters of a nitroxide spin label studied by 9-GHz and 95-GHz EPR spectroscopy and DFT calculations." J. Phys. Chem. A **105**(49): 10967-10977.

- Paktas, D. D. and M. M. Sünnetçioğlu (2007). "EPR spin probe investigation of irradiated wheat, rice and sunflower seeds." Radiat. Phys. Chem. **76**(1): 46-54.
- Peric, M., M. Alves, et al. (2005). "Precision parameters from spin-probe studies of membranes using a partitioning technique. Application to two model membrane vesicles." Biochim. Biophys. Acta **1669**(2): 116-124.
- Polnaszek, C. F., S. Schreier, et al. (1978). "Analysis of the factors determining the EPR spectra of spin probes that partition between aqueous and lipid phases." J Am Chem Soc **100**(26): 8223-8232.
- Pringle, M. J. and K. W. Miller (1979). "Differential effects on phospholipid phase transitions produced by structurally related long-chain alcohols." Biochemistry **18**(15): 3314-3320.
- Roozen, M. J. G. W. and M. A. Hemminga (1990). "Molecular motion in sucrose-water mixtures in the liquid and glassy state as studied by spin probe ESR." J. Phys. Chem. **94**(18): 7326-7329.
- Santos, N. C., M. Prieto, et al. (2003). "Quantifying molecular partition into model systems of biomembranes: an emphasis on optical spectroscopic methods." BBA - Biomembranes **1612**(2): 123-135.
- Schreier, S., C. F. Polnaszek, et al. (1978). "Spin labels in membranes problems in practice." Biochim. Biophys. Acta **515**(4): 395-436.
- Severcan, F., B. Acar, et al. (1997). "Investigation of the fluidity of biological fluids with a PDDTBN spin probe." J. Mol. Struct. **408-409**: 279-281.
- Severcan, F. and S. Cannistraro (1988). "Use of PDDTBN spin probe in partition studies of lipid membranes." Chem.Phys. Lett. **153**(2-3): 263-267.
- Singer, S. J. and G. L. Nicolson (1972). "The fluid mosaic model of the structure of cell membranes." Science **175**(23): 720-731.
- Smirnov, A. I., T. I. Smirnova, et al. (1995). "Very high frequency electron paramagnetic resonance of 2,2,6,6-tetramethyl-piperidinyloxy in 1,2-dipalmitoyl-sn-glycero-3-phosphatidylcholine liposomes: partitioning and molecular dynamics. ." Biophys. J. **68**: 2350-2360.
- Smirnov, A. I., Smirnova, T. I., Morse, P. D. (1995). "Very high frequency electron paramagnetic resonance of 2,2,6,6-tetramethyl-piperidinyloxy in 1,2-dipalmitoyl-sn-glycero-3-phosphatidylcholine liposomes: partitioning and molecular dynamics. ." Biophys. J. **68**: 2350-2360.

- Srivastava, S., R. S. Phadke, et al. (1989). "Effect of incorporation of drugs, vitamins and peptides on the structure and dynamics of lipid assemblies." *Mol Cell Biochem* **91**(1): 99-109.
- Steinhoff, H.-J., Savitsky, A., Wegener, C., Pfeiffer, M., Plato, M., and Möbius, K. (2000). "High-field EPR studies of the structure and conformational changes of site directed spin labeled bacteriorhodopsin." *Biochim. Biophys. Acta* **1457**: 253-262.
- Stoll, S. and A. Schweiger (2006). "EasySpin, a comprehensive software package for spectral simulation and analysis in EPR." *J. Magn. Reson.* **178**: 42-55.
- Tristram-Nagle, S., H. I. Petrache, et al. (1998). "Structure and interactions of fully hydrated dioleoylphosphatidylcholine bilayers." *Biophys J.* **75**(2): 917-925.
- White, S. H., W. C. Wimley, et al. (1998). [4] Protein folding in membranes: Determining energetics of peptide-bilayer interactions. *Method. Enzymol.*, Academic Press. **Volume 295**: 62-87.
- Wilson, R., Kivelson, D. (1966). "ESR linewidths in solution. I. Experiments on anisotropic and spin-rotational effects." *J. Chem. Phys* **44**(1): 154-168.
- Wimley, W. C. and S. H. White (1993). "Membrane partitioning: Distinguishing bilayer effects from the hydrophobic effect." *Biochemistry* **32**(25): 6307-6312.
- Windle, J. J. (1981). "Hyperfine coupling constants for nitroxide spin probes in water and carbon tetrachloride." *J. Magn. Reson.* **45**(3): 432-439.
- Wisniewska, A., J. Widomska, et al. (2006). "Carotenoid-membrane interactions in liposomes : effect of dipolar, monopolar, and nonpolar carotenoids." *Anglais* **53**(3): 475-484.
- Yuan, C., O'Connell, R. J., Jacob R.F., Mason R.P., Treistman, S.N. (2007). "Regulation of the gating of BKCa channel by lipid bilayer thickness." *J. Biol. Chem.* **282**: 7276-7286.



## Chapter 3

### SPIN TRAPPING STUDY OF THE INFLUENCE OF TAXIFOLIN ON FENTON REACTION IN ETHANOL AND METHANOL

Katerina Makarova, Katarzyna Łastawska, Katarzyna Zawada, Iwona Wawer

Published in *Current Topics in Biophysics Online*, **2010**, vol. 33 (Suplement A), p. 153-156.

#### ABSTRACT

To examine the effect of solvents on the nature and amount of the spin adducts, spin trapping experiments with 4-POBN, the Fenton reagents and taxifolin were performed in solutions of ethanol or methanol and water. The addition of taxifolin resulted in a decrease of the spectrum intensity of the spectrum that was dependent on taxifolin concentration. Computer simulation revealed that 4-POBN/ $\bullet\text{CH}(\text{CH}_3)\text{OH}$  adduct dominated in ethanol whereas 4-POBN/ $\bullet\text{OH}$  and 4-POBN/ $\bullet\text{CH}_2\text{OH}$  adducts are present in methanol.

### **3.1 Introduction**

Flavonoids are a group of compounds abundant in plants and also present in human diet. Many studies confirm the role of flavonoids in preventing diseases like coronary heart disease, cancer and age-related neuropathologies. Flavonoids are able to scavenge free radicals, chelate transition metal ions and interact with other antioxidants (Teixeira, Siquet, Alves, Boal, Marques, Borges, Lima & Reis, 2005). Taxifolin, which is present in the plants from pinus genus (in pinus maritima), in the milk thistle seeds (Kim, Graf, Sparacino, Wani & Wall, 2003), and in citrus fruits, has a flavanone structure and can act as an antioxidant due to reducing properties of its hydroxyl groups. The radical-scavenging activity of fruit extracts, juices and herbal teas was estimated by various methods including ESR technique (Oszmiański, Wolniak, Wojdyło & Wawer, 2007; Wasek, Nartowska, Wawer & Tudruj, 2001; Oszmiański, Wolniak, Wojdyło & Wawer, 2008).

The aim of this research was to study the radicals produced in Fenton reaction with methanol or ethanol and the mechanism of their reaction with taxifolin. The ESR technique, coupled with spin trapping methods and computer simulation has been extensively used for the detection and identification of short-lived free radicals. The method of spin trapping is based on the scavenging of the radicals by a spin trap, leading to the formation of a spin adduct with higher stability. In this work a 4-POBN spin trap was chosen due to its stability and its selectivity toward trapping of carbon-centered radical species. Normally, it is easy to establish the presence of the radical and more of a challenge to identify it. Computer simulation is the most powerful technique in the analysis of multi component ESR spectra.

### **3.2 Experimental details**

#### *3.2.1 ESR spectroscopy*

ESR spectra were measured on a MiniScope MS 200 spectrometer from Magnettech at room temperature (23-24°C) in 50 µl capillary tubes. Typical instrument settings were: microwave attenuation 10 dB, modulation amplitude of 0.5G, sweep time 20s. Measurements of kinetics were performed every 3 minutes unless indicated otherwise. The simulations of fast motion ESR spectra were performed with routines implemented in EasySpin toolbox (Stoll & Schweiger, 2006) for Matlab. The ESR spectra of 4-POBN spin adducts exhibit hyperfine splittings from one  $^{14}\text{N}$  and one  $^1\text{H}$  – nuclei. The hyperfine data provided a good

initial guess for the fitting (Janzen, Wang & Shetty, 2006; Finkelstein, Rosen & Rauckman, 1982; Sridhar, Beaumont & Powers, 1986).

### 3.2.2 Generation of free radicals for ESR

$\alpha$ -(4-Pyridyl N-oxide)-N-tert-butyl nitron (4-POBN) was purchased from Sigma Aldrich. Solutions were prepared using distilled and degassed water. Taxifolin solutions (0.010 M) in methanol and (0.012 M) in 96% ethanol were prepared, kept in a refrigerator and protected from light. Samples were prepared using 20  $\mu$ l of 20mM 4-POBN dissolved in water. POBN was mixed with 20  $\mu$ l of 5mM FeSO<sub>4</sub> prepared freshly from 0.1M stock solution and 20  $\mu$ l of 25mM H<sub>2</sub>O<sub>2</sub> solution, prepared from 30% solution. Finally, 20  $\mu$ l of taxifolin sample (or solvent only) was added. The taxifolin concentration varied from 0.1mM to 2mM.

## 3.3 Results and discussions

The Fenton reaction was the method for generating free radicals. To examine the effect of solvents on the nature and amount of the spin adducts, spin trapping experiments in the Fenton reagents in ethanol, methanol and water were performed first. The second set of experiments was performed in the presence of taxifolin solutions.

### 3.3.1 Spin Trapping in solvents

The 4-POBN/ $\bullet$ OH radical adduct was the only species obtained in the Fenton reactions based on Fe(II) in water. The 4-POBN/ $\bullet$ OH adducts were unstable and decayed fast to ESR silent products. The hyperfine splittings obtained by computer simulations are  $a_N = 14.9$ G and  $a_H = 1.63$  G. These values are in agreement with previous data (Janzen *et al.*, 2006) and were used for further simulations.

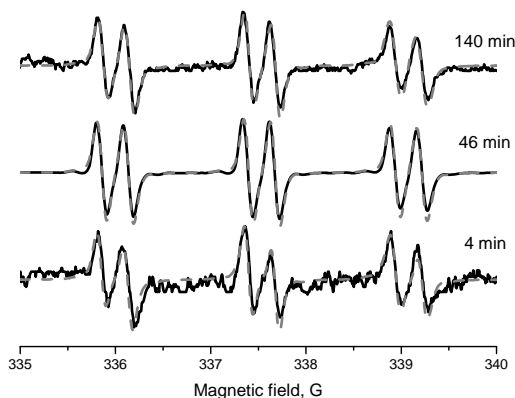


**Figure 1.** X-band ESR spectra of 4-POBN/ $\bullet$ OH and 4-POBN/ $\bullet$ CH<sub>2</sub>OH spin adduct in Fenton reaction with methanol recorded after 4, 46 and 140 minutes of reaction (solid line). The dotted lines are calculated spectra using hyperfine splitting constants from Table 1.

A 6-line ESR spectrum due to 4-POBN radical adducts was recorded when mixing Fe<sup>2+</sup> (as FeSO<sub>4</sub>), H<sub>2</sub>O<sub>2</sub>, 4-POBN and methanol. The spectra were registered every 3 minutes, starting from the 4<sup>th</sup> minute after the addition of H<sub>2</sub>O<sub>2</sub> to the sample. Computer simulation of the spectrum (Fig. 1) revealed a species having hyperfine coupling constants of  $a_N = 15.5$  G and  $a_H = 2.8$  G and  $a_N = 15.0$  G and  $a_H = 1.6$  G (Table 1) values reasonably close to 4-POBN/ $\bullet$ CH<sub>2</sub>OH and 4-POBN/ $\bullet$ OH adducts in aqueous solution (Sridhar *et al.*, 1986). The ESR spectrum measured 4 minutes after the addition of H<sub>2</sub>O<sub>2</sub> to the sample and the spectrum measured after 140 minutes of the reaction had a similar (30%) ratio of 4-POBN/ $\bullet$ OH (Fig. 1). The ESR signal measured 20-80 minutes after H<sub>2</sub>O<sub>2</sub> addition to the sample was dominated by 4-POBN/ $\bullet$ CH<sub>2</sub>OH radical adduct (Fig. 1).

**Table 1.** Isotropic hyperfine splitting of 4-POBN adducts in solutions

System	Adduct	hyperfine splitting, G	
		$a_N$	$a_H$
Fe(II)/H <sub>2</sub> O/4-POBN	4-POBN/ OH	14.9	1.6
Fe(II)/MeOH/4-POBN	4-POBN/ OH	15.0	1.6
	4-POBN/ CH <sub>2</sub> OH	15.4	2.8
Fe(II)/EtOH/4-POBN	4-POBN/ CH(CH <sub>3</sub> )OH	15.5	2.5

The Fenton reaction in ethanol can generate a number of radicals (Bosnjakovic and Schlick, 2006). Computer simulation of radicals that were trapped by 4-POBN revealed a

mixture of C-centered radical adducts. The 4-POBN/ $\bullet\text{CH}(\text{CH}_3)\text{OH}$  adduct, the most commonly detected, dominates the spectrum with hyperfine splittings: of  $a_{\text{N}} = 15.5$  G and  $a_{\text{H}} = 2.5$  G (Table 1). However, the 4-POBN/ $\bullet\text{OH}$  radical adduct was not detected in Fenton reaction with ethanol. This result suggested that  $\bullet\text{OH}$  radicals rather react with ethanol producing  $\bullet\text{CH}(\text{CH}_3)\text{OH}$  radicals, and then they are trapped by 4-POBN. It is important to note that the reaction of ferryl radical, usually produced in Fenton reaction, with ethanol (Yamazaki and Piette, 1990) is another mechanism of  $\bullet\text{CH}(\text{CH}_3)\text{OH}$  radicals production.

### 3.3.2 Spin trapping in Fenton reagents in the presence of taxifolin solutions

Taxifolin concentration had a significant effect on the intensity of the ESR signal and kinetics of its decay. The taxifolin concentration of 0.1mM decreased the intensity by about 50% in comparison with the reference. The concentration of 2mM caused signal decay during 15 minutes. The spin adducts which were detected in the presence of taxifolin in methanol were similar to the situation in the absence of taxifolin, i.e. 4-POBN/ $\bullet\text{OH}$  and 4-POBN/ $\bullet\text{CH}_2\text{OH}$  appeared. The first stage of the reaction, where  $\bullet\text{OH}$  radicals were formed and trapped by 4-POBN remained unchanged, however higher concentrations of taxifolin decreased the intensity of carbon-centered radical adduct signal and shortened the period of carbon-centered radical domination in the spectrum (Fig. 2).

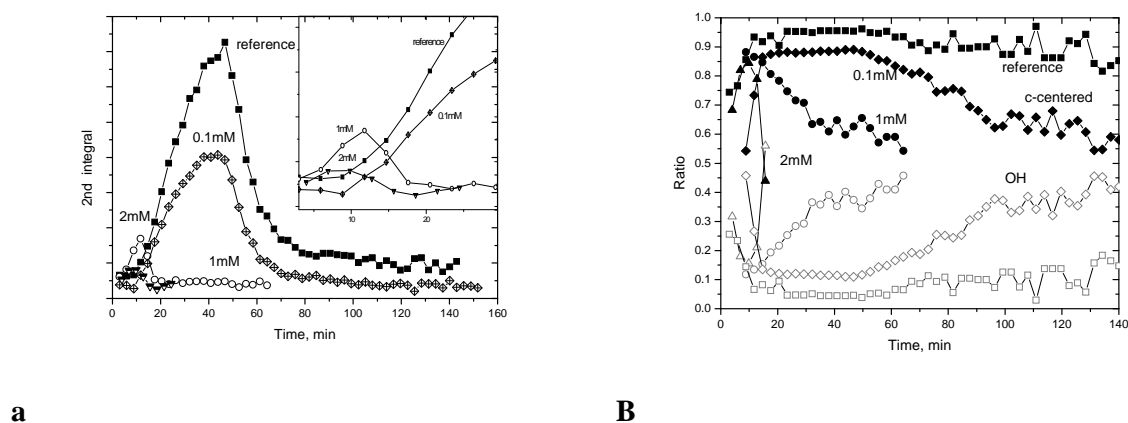


**Figure 2.** (a)  $2^{\text{nd}}$  integral of ESR signal intensity of 4-POBN radical adducts from Fenton reaction with methanol (■) in the presence of 0.1mM (◇), 1mM (○) and 2mM (▼) of taxifolin. (b) ratio between 4-POBN/OH (grey symbols) and 4-POBN/ $\text{CH}_2\text{OH}$  (black symbols) components in reference (■) system and in the presence of 0.1mM (◇), 1mM (○) and 2mM (▼) of taxifolin.

The same dominating adduct (4-POBN/ $\bullet\text{CH}(\text{CH}_3)\text{OH}$ ) was identified in the presence of taxifolin in ethanol. The effect of taxifolin concentration on the ESR signal intensity was similar to the system with methanol. The taxifolin concentration of 0.1mM decreased the intensity by about 50 % in comparison with the reference, higher concentrations (1mM and 11.7mM) caused a very fast decay of the ESR signal (Fig.3).

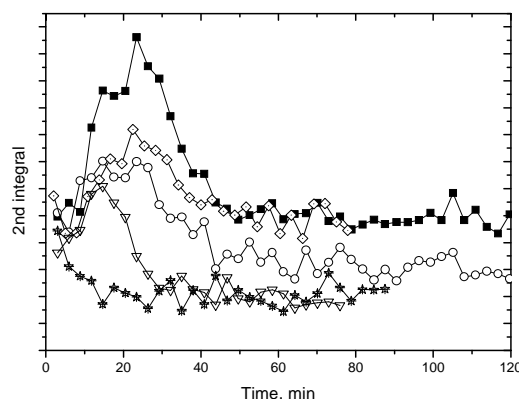


**Figure 3.** 2<sup>nd</sup> integral of ESR signal intensity of 4-POBN radical adduct from Fenton reaction with ethanol (■) in the presence of 0.05mM (◇), 0.1mM (○), 1mM (▼) and 11.7mM (★) of taxifolin.

The general conclusion is that the presence of taxifolin affects the intensity of carbon-centered 4-POBN adduct component. There are several possible explanations for this effect: (i) taxifolin could react with 4-POBN radical adducts resulting in ESR silent products; (ii) taxifolin could react with radicals formed in the experimental systems (scavenging), and (iii) the reaction of taxifolin with Fe(II) or intermediate radicals that are involved in 1-hydroxyethyl or hydroxymethyl radical production.

### 3.4 Conclusions

The radicals formed in the Fenton reaction with methanol and ethanol were studied with ESR spin trapping technique and analyzed with the aid of computer simulations. The fitting of experimental spectra made it possible to identify radical adducts that were formed in these reactions and to follow the kinetics of each component. It was shown that the presence of taxifolin decreased the ESR signal intensity, affecting mainly the c-centered radical adduct component. Taxifolin mechanism of the reaction with free radicals requires further investigation. Further experiments are in progress.

## **ACKNOWLEDGMENTS**

EPR measurements were accomplished at the Structural Research Lab., Medical University of Warsaw, Faculty of Pharmacy, Poland. SRL was established with financial support from European Regional Development Fund in the Sectoral Operational Programme "Improvement of the Competitiveness of Enterprises, years 2004-2006" project no: WKP\_1/1.4.3./1/2004/72/72/165/2005/U

## REFERENCES

- Bosnjakovic A. and Schlick S. (2006). "Spin Trapping by 5,5-Dimethylpyrroline-N-oxide in Fenton Media in the Presence of Nafion Perfluorinated Membranes: Limitations and Potential." J. Phys. Chem. B, **110**, 10720-10728.
- Finkelstein E., Rosen G. M. and Rauckman E.J. (1982). "Production of hydroxyl radical by decomposition of superoxide spin trapped adducts." Mol. Pharmacol., **21**, 262–265.
- Janzen E.G., Wang Y.Y. and Shetty R.V. (2006). "Spin trapping with alpha-pyridyl 1-oxide N-tert-butyl nitrones in aqueous solutions. A unique electron spin resonance spectrum for the hydroxyl radical adduct." J. Am. Chem. Soc., **100**, 2923-2925.
- Kim N.C., Graf T.N., Sparacino C.M., Wani M.C. and Wall M.E. (2003). "Complete isolation and characterization of silybins and isosilybins from milk thistle (*Silybum marianum*)." Org. Biomol. Chem., **1**, 1684-1689.
- Oszmiański J., Wolniak M., Wojdyło A. and Wawer I.(2007). "Comparative study of polyphenolic content and antiradical activity of Cloud and clear apple juices." J. Sci. Food Agric., **87**, 573-579.
- Oszmiański J., Wolniak M., Wojdyło A. and Wawer I.(2008). "Influence of apple puree preparation and storage on polyphenol contents and antioxidant activity." Food Chem., **107**, 1473-1484.
- Sridhar R., Beaumont P. and Powers E., J. (1986). "Fast kinetics of the reactions of hydroxyl radicals with nitron spin traps." Radioanal. Nucl. Chem., **101**, 227-237.
- Stoll S. and Schweiger A.(2006). "EasySpin, a comprehensive software package for spectral simulation and analysis in EPR." J. Magn. Reson., **178(1)**, 42-55.
- Teixeira S., Siquet Ch., Alves C., Boal I., Marques M. P., Borges F., Lima J.L.F.C. and Reis S.(2005). "Structure–property studies on the antioxidant activity of flavonoids present in diet." Free Rad. Biol. Med., **39**, 1099 – 1108.
- Wasek M., Nartowska J., Wawer I. and Tudruj T.(2001). "Electron spin resonance assessment of the antioxidant potential of medicinal plants. Part I. Contribution of anthocyanosides and flavonoids to the radical scavenging ability of fruit and herbal teas." Acta Pol. Pharm. Drug Res., **58**, 283-288.
- Yamazaki I. and Piette L.H. (1990). "ESR Spin-trapping Studies on the Reaction of Fe<sup>2+</sup> Ions with H<sub>2</sub>O<sub>2</sub>-reactive Species in Oxygen Toxicity in Biology." J. Biol. Chem., **265**, 13589-13594.



## Chapter 4

### A COMBINATION OF NEURAL NETWORKS AND DFT CALCULATIONS FOR COMPREHENSIVE ANALYSIS OF FDMPO RADICAL ADDUCTS FROM FAST ISOTROPIC ELECTRON SPIN RESONANCE SPECTRA

Katerina Makarova, Ekaterina V. Rokhina, Elena A. Golovina, Henk Van As,  
Jurate Virkutyte

To be submitted

#### ABSTRACT

The 4-hydroxy-5,5-dimethyl-2-trifluoromethylpyrroline-1-oxide (FDMPO) spin trap is very attractive for spin trapping studies of free radicals due to its high stability and high reaction rates with various free radicals. However, the identification of FDMPO radical adducts is a challenging task, since they have very comparable ESR spectra. Here we propose a new method for the analysis and interpretation of the ESR spectra of FDMPO radical adducts. As the first step the strongly overlapping ESR spectra were analyzed with the aid of computer simulations. As a result of simulations the N- and F-hyperfine splitting constants that include both interactions of the electron spin with the nearby nuclei and interactions with the solvent were obtained. During the second step an artificial neural network (ANN) was adopted to identify the radical adducts formed in the variety of chemical systems (e.g. Fenton reaction, cleavage of the powerful disinfectant peracetic acid over  $\text{MnO}_2$ , etc). The introduced ANN operates excellently on both “known” FDMPO radical adducts measured in slightly different solvents and not *a priori* “known” FDMPO radical adducts. Finally, the N- and F-hyperfine splitting constants of  $\text{OH}^*$ ,  $\text{CH}_3^*$ ,  $\text{CH}_2\text{OH}^*$  and  $\text{CH}_3(\text{C}=\text{O})\text{O}^*$  radical adducts of

FDMPO were calculated using density functional theory (DFT) at the B3LYP/6-31G//B3LYP/6-31G++ level of theory to confirm the experimental data.

#### 4.1 Introduction

Production of free radicals is essential in normal metabolism. However, in unregulated concentrations, they have been widely regarded as a cause of cell injury and death (Blake, Allen et al. 1987). Understanding of biological mechanisms that involve free radicals requires efficient radical detection and accurate characterization. Electron Spin Resonance (ESR) spectroscopy has been extensively used for the detection and identification of short-lived free radicals. However, the short lifetime, the high reactivity and as a consequence the low concentration of free radicals limit their direct detection. To overcome these drawbacks the spin trapping method was introduced (Janzen 1971). It is based on the trapping of radicals by a spin trap, leading to the formation of a more stable radical, a so called spin adduct, that can be easily detected by ESR spectroscopy. Moreover, the shape of ESR spectra of a spin adduct can be used to identify the trapped radical. The spin trapping technique has found application in the study of the *in vitro* and *in vivo* formation of free radicals (Dikalova, Kadiiska et al. 2001).

However, the application of the spin trapping technique to investigate radical formation in complex systems (e.g. biological systems) also meets two important limitations: (1) a different trapping efficiency of particular types of radicals, and (2) a short lifetime of some spin adducts (e.g. superoxide) (Finkelstein, Rosen et al. 1979). To overcome these limitations, a number of novel spin traps have been introduced and evaluated for qualitative analysis of radical-generating systems. One of them, 4-hydroxy-5,5-dimethyl-2-trifluoromethylpyrroline-1-oxide (FDMPO), a fluorinated analogue of 5,5-dimethylpyrroline-N-oxide (DMPO), is potentially important for the study of radical production due to the high stability of the FDMPO radical adducts (up to several days) and the high trapping rate for a wide range of free radicals (including C-centered, OH, O<sub>2</sub> and other free radicals) (Khramtsov, Reznikov et al. 2001; Bacic, Spasojevic et al. 2008). High FDMPO spin-trapping efficiency and its application to the trapping of oxygen and c-centered free radicals in chemical and biological systems have been studied previously (Khramtsov, Reznikov et al. 2001). However, the identification of FDMPO radical adducts is a challenging task, since the relation between the structure and the ESR spectral parameters (splitting pattern) for FDMPO spin adducts is not unique. In most cases the different radical adducts exhibit very comparable splitting patterns: a triplet of which each line is split in a 1:4:4:1 quartet due to the interaction

of the electron spin with the nuclear spins of the nearby N- and F-nuclei. Structural assignment of spectral components can be based on comparison of the ESR parameters of spin adducts produced in alternate ways, e.g in different solvents (Janzen, Zhang et al. 1995). However, the differences found between the different spin adducts may be quite small and the changes in the ESR parameters due to a change in the solvent may be larger than the differences between the various radicals (Janzen, Zhang et al. 1995; Janzen 1998).

These above mentioned drawbacks are important in complex biological systems if more than one type of radical is generated. In that case, the measured ESR spectrum is a linear superposition of the spectra of the different spin adducts. Such a superposition of overlapping spectra often causes difficulties for qualitative and quantitative analysis of the ESR spectra and complicates the direct extraction of hyperfine splitting constants. Such multi-component ESR spectra can be analyzed with the aid of simulation based fitting (SBF), which allows the most accurate extraction of hyperfine splitting constants. In this approach the experimental ESR spectrum is approximated by a simulated one. The simulated ESR spectrum is obtained via mathematical modeling. The choice of the mathematical model for simulation determines which parameters are obtained after the fit and their accuracy. A fast isotropic motion model is successfully used for the simulation of the ESR spectra of various spin traps (Busi, Travagli et al. 2010; Rokhina, Makarova et al. 2010). The difference between experimental and simulated spectra is characterized by an error function or the residuals. So the goal of SBF is to minimize the error function (or residuals) by adjusting ESR parameters, such as hyperfine splitting constants ( $a_{\text{iso}}$ ),  $g_{\text{iso}}$ , correlation time and fractions of the components. The experimental and simulated spectra are cyclically compared until the error function is minimal. The set of ESR parameters, which corresponds to the minimum error, is used for identification of the trapped radical. This type of analysis is usually performed by a special program (for example EasySpin toolbox for Matlab (Budil, Lee et al. 1996; Stoll and Schweiger 2006), or a home developed program (Kirste 1992; Budil, Lee et al. 1996)).

An alternative approach to identify radical adducts is the comparison between the theoretical ESR parameters calculated on the basis of Density Functional Theory (DFT) optimized geometries, and the experimental ESR parameters of the studied radical adduct (Jerzykiewicz, Cwielag-Piasecka et al.). DFT calculations allow in particular to estimate both the structure of the trapped radical and to predict its ESR spectral parameters, such as hyperfine splitting constants and  $g_{\text{iso}}$ . Good agreement with experiments was achieved for DEPMPO and DMPO radical adducts and TEMPO using DFT calculations at B3LYP, EPR-II, PBE level of theory (Owenius, Engstrom et al. 2001; Fau and Bartlett 2003; Villamena,

Hadad et al. 2004). The computed parameters depend on the molecular geometry, method and basis set of the calculation. In addition, both solvent and vibrational effects change the hyperfine splitting constants of a molecule by a few percent with respect to the nonvibrating gas phase values. In extreme cases, solvent effects may introduce 10 % deviations, and vibrational effects (large amplitude motions) deviations as large as 37 % (Fau and Bartlett 2003). Solvent effects can be approximated by taking into account the Polarized Continuum Model (PCM) with inclusion of several solvent molecules (Owenius, Engstrom et al. 2001), but vibrational effects are expensive to calculate (Fau and Bartlett 2003). Thus, it is more practical to determine trends in the dependence of the the calculated hyperfine splitting constants on structure and solvent than to compare absolute values with experimental results (Owenius, Engstrom et al. 2001).

Despite the continuing improvement of accuracy and speed of DFT calculations, there is still a need for a new strategy to radical adducts identification. Key aspects for a new identification method are its applicability to a large number of radical adducts and its robustness to solvent effects on hyperfine splitting constants. However, the correlation between ESR parameters and FDMPO radical adduct structure is hard to express explicitly. The artificial neural network (ANN) approach (Wasserman 1989; Bishop 1995) is a powerful tool for approximating functions. Here we explore its applicability for FDMPO radical adduct identification with the use of ESR parameters. Due to its flexibility in dealing with different types of input data and with nonlinearity, artificial neural networks have been successfully applied to a variety of classification, pattern-recognition and function-approximation tasks in industry, business and science (Roth 1990; Corne, Johnson et al. 1992). Unlike the standard methods for function approximation, the ANN approach does not require the explicit specification of a specific function. In ANNs, which were inspired real biological neural networks, the synaptic connections between neurons are represented by numerical weights, which measure the strength of a connection, and by a transfer function that emulates the firing of the neuron. The training of a network involves the establishing of a set of numerical weights that successfully connects the training input (FDMPO adduct hyperfine splitting constants) to the desired output (a predefined group of radicals). Once being trained, an artificial neural network can be an effective and rapid tool for identification of unknown radical adducts formed in a reaction.

The goal of the present work was to develop a new comprehensive approach for the analysis of ESR spectra from FDMPO spin adducts to identify trapped radicals. The new approach combines simulation of experimental ESR spectra from FDMPO spin adducts and

identification of radical adducts by ANN based on obtained N- and F- hyperfine splitting constants (hfsc). To support spin adduct identification theoretical DFT calculations were undertaken. The proposed approach was applied to the analysis of FDMPO spin adducts generated in the Fenton reaction with DMSO, methanol, ethanol and cleavage of the powerful disinfectant peracetic acid (PAA) over  $\text{MnO}_2$ . Optimized geometries and theoretical ESR parameters are reported for FDMPO/OH, FDMPO/ $\text{CH}_3$ , FDMPO/ $\text{CH}_2\text{OH}$  and FDMPO/ $\text{CH}_3\text{COO}$  radical adducts.

## 4.2 Materials and Methods

### 4.2.1 ESR spectra simulation

An SBF approach was used to analyse the ESR spectra. The fast isotropic motion model (Israelachvili, Sjösten et al. 1975) was used to simulate ESR spectra from FDMPO spin adducts and to extract parameters. The superimposed ESR spectrum arises from different FDMPO radical adducts in the same media, resulting in triplets of which each line is split in a 1:4:4:1 quartet. In this case changes in the hyperfine splitting constant values ( $a_F$  and  $a_N$ ) and  $g_{\text{iso}}$  are attributed only to the radical adduct structure. The radical adduct geometry also influences the rotational correlation time  $\tau_R$ , which defines the broadening of the ESR line shape. The additional broadening of ESR line shape, originating from the presence of paramagnetic oxygen, influences all spectral lines of different components in the same way so only one parameter,  $\Gamma_r$ , is needed to describe it. The experimental ESR line shape was described by a Voigtian line shape (a convolution of a Gaussian and Lorentzian line shape with a 1:1 ratio). A fitting program, based on the simplex optimization method of Nelder and Mead (Nelder and Mead 1965), was employed to extract the g-factor, nitrogen and fluorine hyperfine splitting parameters as well as the rotational correlation time and the fraction of each radical adduct component. In order to eliminate the correlation between parameters (described in chapter 2) and improve the accuracy of fraction parameter the simulations were performed using one value of  $\Gamma_r$  for all spectral components.

### 4.2.2 Neural Network Modeling.

A small artificial neural network was programmed with Matlab R2009a software using the “newp” routine. A multi-layer feedforward neural network, also known as a multilayer perceptron (MLP) (Rosenblatt 1958), was used in this study. This is a fully connected neural network since a neuron in any layer of the network is connected with all the neurons/nodes of

the previous layer. The output signals from the first layer form the input signals for the output layer. The layers between the input and output layers are known as hidden layers (neurons in these layers are called hidden neurons). An MLP with sigmoid activation functions (Mitchell 1997) and one hidden layer was used. A simple scheme of the network structure and the behavior is shown in Figure 1. The N- and F-hfsc values were used as input for the ANN. The output of the ANN is a pre-defined group of the radical adducts with similar structure. In this study 4 groups of radical adducts were pre-defined. The use of a combination of 1 and 0 signals for the ANN output results enables the use of only 2 output nodes for the coding of the 4 groups, i.e. group 1 corresponds to the [0;0] output of the ANN, group 2 – [1,0], group 3 – [0,1] and group 4 – [1,1]. The MLP was trained by the back propagation algorithm (BPA) (Rumelhart, Hinton et al. 1986). During the neural network learning process, the weights of the connections were adjusted by backward propagation of the error signals at the output of the neural network, layer by layer, until the error between the predicted outputs and the actual outputs was minimized to the target value, Sum Squared Error (SSE) of 0.001 (William 1986).

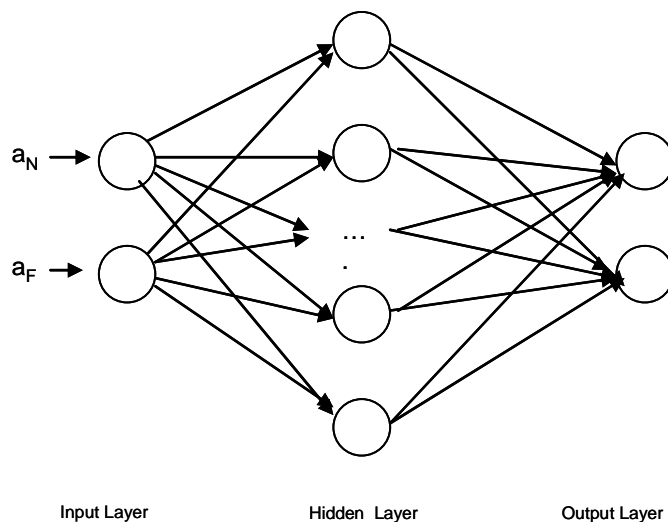


**Figure 1.** Multi Layer Perceptron with one hidden layer.

#### 4.2.3 Training and testing data sets.

The data sets for training and validating the neural network model consists of input data, i.e. nitrogen and fluorine hyperfine splitting constants, and corresponding output data, i.e. the group of radical adducts. The input data consisted of nitrogen and fluorine hyperfine splitting constants reported by Khramtsov et al (Khramtsov, Reznikov et al. 2001) for the

FDMPO spin trap and was extended with data published by Janzen et al (Janzen, Zhang et al. 1995) for 5,5-dimethyl-2-(trifluoromethyl)-1-pyrroline N-oxide (2-TFDMPO). Hydrogen hyperfine splitting constants were not included as parameters since spectra from radical adducts where hydrogen hyperfine constants could be extracted were not considered for the classification problem. For a better performance of the neural network the input data was scaled in the interval [0; 1] to avoid that higher input values (nitrogen hyperfine splitting constants) had a higher weight in the learning process than the smaller input values (fluorine hyperfine splitting constants). The neural network was trained on F- and N-hfsc values of 2-TFDMPO spin adducts (Table 1, 2-TFDMPO), and then the performance of the trained ANN was tested on data not presented in the training set (Table 1, FDMPO).

**Table 1.** Training and testing set of input (hyperfine splitting constants of various FDMPO and 2-TFDMPO spin adducts) and output (groups of radical adducts) data.

FDMPO* - testing set			
$a_N$	$a_F$	Group	Radical adduct
13.9	2.75	2	OH
14.9	2.05	4	CH <sub>3</sub>
14.75	2.4	3	CH <sub>2</sub> OH group
2-TFDMPO** -training set			
13.14	2.8	1	O <sub>2</sub>
13.98	2.7	2	OH
14.37	2.64	3	HOCH <sub>2</sub> CHCHOH
14.47	2.87	3	HOCHCH <sub>3</sub>
14.52	2.74	3	HOCHCH <sub>2</sub> CH <sub>3</sub>
14.22	2.33	3	HOCH <sub>2</sub>
14.9	2.05	4	CH <sub>3</sub>
14.42	2.33	3	HOCH <sub>2</sub>
14.32	2.93	3	CH <sub>3</sub> CH <sub>3</sub> COH
14.91	1.76	4	HC≡C
13.14	2.8	1	OOH

\*Data from Khramtsov et al. 2001(Khramtsov, Reznikov et al. 2001)

\*\* Data form Janzen et. al. 1995 (Janzen, Zhang et al. 1995)

#### *4.2.4 DFT calculations*

To obtain independent support for the interpretation of ESR spectra, quantum chemistry calculations using density functional theory (DFT) were performed on a set of FDMPO radical adducts to obtain F-hfcs and N-hfcs values. All calculations were carried out using the GAUSSIAN 03 program (Frisch, Trucks et al. 2003). Optimized geometries of FDMPO/OH, FDMPO/CH<sub>3</sub>, FDMPO/CH<sub>2</sub>OH and FDMPO/CH<sub>3</sub>COO radical adducts were obtained with DFT at the B3LYP/6-31G level of theory. Stationary points for geometry optimization of FDMPO radical adducts were determined to have zero imaginary vibrational frequencies as derived from a harmonic vibrational frequency analysis at the level of theory at which the stationary points were optimized. The atomic coordinates of the geometry optimized radicals were subsequently used to perform a scan over the dihedral angle of the trifluoromethyl group and the pyrroline ring. For each dihedral angle (rotation of CF<sub>3</sub>), the total energy and the F-hfcs and N-hfcs were calculated with the B3LYP/6-31++G basis set. The solvent effect on the hyperfine splitting values was considered using the polarizable continuum model (PCM) to include the effect of the solvent dielectric constant and two solvent molecules to include the effect of hydrogen bonding (Owenius, Engstrom et al. 2001; Tomasi, Mennucci et al. 2005).

#### *4.2.5 Sample preparation*

MnO<sub>2</sub>, PAA (40%), EDTA, methanol, ethanol, DMSO and other chemicals were purchased from Sigma Aldrich and Merck & Co., Inc. FDMPO was purchased from Alexis Biochemicals (USA). All chemicals were of laboratory reagent grade and were used without further purification. Distilled water was used in all the experiments. The Fenton reaction was carried out using 5 µl of 0.5 mM FeSO<sub>4</sub> and 5 µl of 5 mM H<sub>2</sub>O<sub>2</sub>. The samples were prepared by adding 5 µl of 10 mM FDMPO and 5 µl of ethanol or methanol.

#### *4.2.6 ESR measurements*

ESR measurements were carried out using an X-band Bruker E500 Elexsys SuperX spectrometer with 100 kHz field modulation. Typical instrument settings were 5 mW microwave power, 0.5 G modulation amplitude, 20 s time constant, and 4 scans were accumulated.



## 4.3 Results and discussion

### 4.3.1 ESR spectra simulation

In Fig 2. the ESR spectra of FDMPO adducts (solid line) recorded for the Fenton reaction with DMSO (1), methanol (2), ethanol (3) and for the PAA cleavage over  $\text{MnO}_2$  (4) in the presence of FDMPO, immediately after the addition of all reagents, are presented. For these systems, the ESR spectral shapes result from the superposition of at least two spectra originating from two different radical species. The generated free radical species are characterized by hyperfine splitting constants from fluorine and nitrogen, F-hfsc ( $a_F$ ) and N-hfsc ( $a_N$ ), respectively. However, these parameters could not be extracted directly from the experimental spectra, due to the spectral overlap. For an accurate interpretation of the experimental spectra of FDMPO radical adducts and the identification of the trapped radicals analysis using the SBF technique is needed. Based on SBF different components in the experimental ESR spectra (Fig. 2) were separated on the basis of the N- and F-hfsc values. In general the simulated spectra (Fig. 2, spectra b) are in a good agreement with the experimental ones (Fig. 2, spectra a), indicating that the proposed model for spectra simulations (Israelachvili, Sjösten et al. 1975) that considers only the nitrogen complete hyperfine splitting tensor and the g-tensor, can be used for the simulation of X band ESR spectra of the FDMPO radical adducts. The fits allowed to extract the fraction coefficient  $f$  for the two FDMPO spin adducts and the isotropic nitrogen and fluorine hyperfine splitting constants ( $a_N$  and  $a_F$ ) (Fig. 2, spectra d,e).  $f$  is defined as the ratio of the integrated intensity of one of the spectral components and the total integrated intensity of the ESR spectrum. In addition, the isotropic tensor values  $g_{iso}$  and the values for the isotropic rotational correlation times  $\tau_R$  were obtained. These parameters are also related to the structure of the radical adduct. However, they are usually not used for the identification of the radical adduct because values of  $g_{iso}$  and  $\tau_R$  extracted from X-band ESR spectra are not accurate enough to show the pronounced difference for various spin adducts. According to the SBF, the hyperfine coupling constants determined for one of the radical adducts were  $a_F = 2.60\text{-}2.77$  G and  $a_N = 13.6\text{-}13.7$  G (Table 2). These constants are characteristic for FDMPO/ $\text{OH}^*$  (Fig. 2 spectra d). The hyperfine coupling constants of the second radical adduct (Fig. 2, spectra e) were  $a_F = 1.93\text{-}2.6$  G and  $a_N = 13.8\text{-}14.6$  G, values that are typical for carbon centered radicals (Khramtsov, Reznikov et al. 2001).

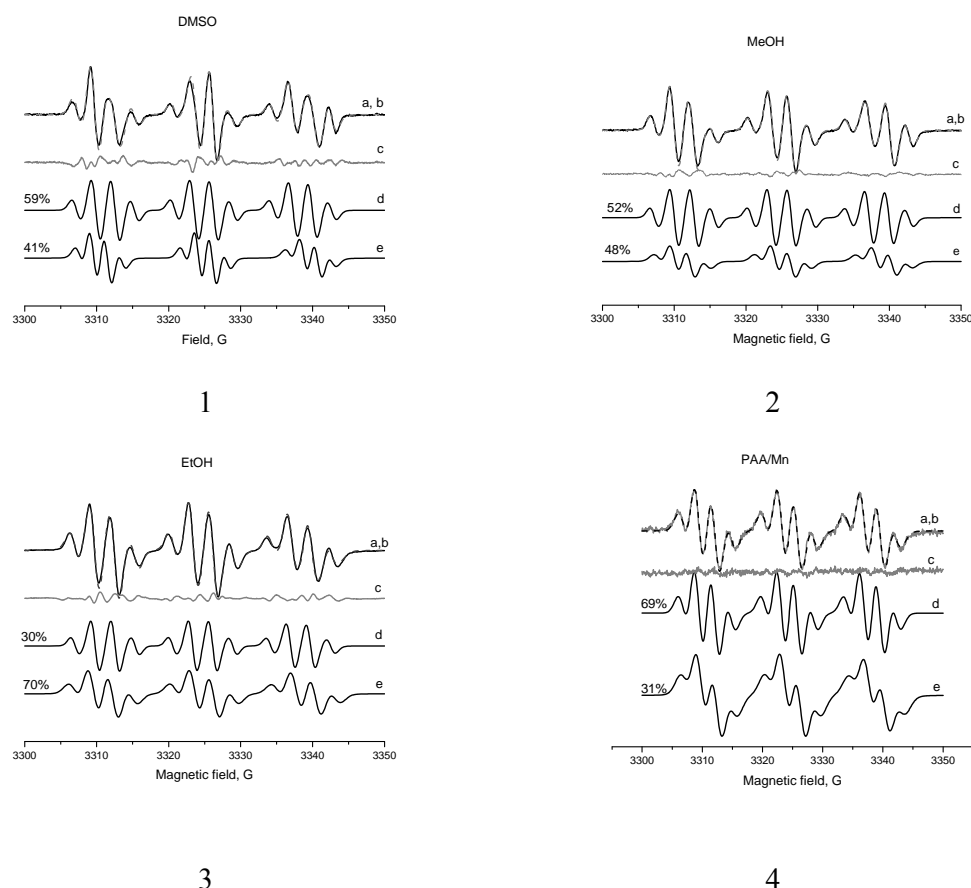


**Figure 2.** Experimental and simulated spectra of FDMPO spin adducts. (1) DMSO; (2) methanol (3) ethanol, (4) PAA cleavage of  $\text{MnO}_2$ ; (a,b) Experimental and simulated spectrum of the FDMPO radical adducts; (c) residuals; (d) FDMPO/OH radical adduct component; (e) c-centered FDMPO radical adduct component

**Table 2.** The results of ANN identification of groups of FDMPO radical adducts. The input values of experimental hyperfine splitting constants are obtained by SBF of ESR spectra of various FDMPO spin adducts from the Fenton reaction with methanol, ethanol and DMSO and the PAA/Mn system.

Experimental		System	ANN output	
$a_N$ , G	$a_F$ , G		Group	Radical adduct
13.6	2.77	Fenton with methanol	2	$\text{OH}^*$
14.08	2.13	Fenton with methanol	3	$\text{CH}_2\text{OH}^*$
13.6	2.7	Fenton with ethanol	2	$\text{OH}^*$
14.1	2.59	Fenton with ethanol	3	$\text{CH}_3\text{CH}_2\text{OH}^*$
13.7	2.59	Fenton	2	$\text{OH}^*$
14.6	1.93	Fenton with DMSO	4	$\text{CH}_3^*$
13.7	2.68	Fenton with DMSO	2	$\text{OH}^*$

13.8	2.46	PAA	3	CH <sub>3</sub> COO*
13.7	2.6	PAA	2	OH*

#### 4.3.2 Development of ANN for identification of radical adducts on the basis of spectral parameters according to the chemical structure

Traditionally, for the majority of spin traps the assignment of radical adducts is based on the formation of the same adducts from known sources. However, the available spectral parameters sometimes do not vary enough to provide structural information about groups attached further away than two or three bonds from the nitroxyl group (Janzen and Liu 1973). This certainly holds for FDMPO (Khramtsov, Reznikov et al. 2001). The identification of FDMPO trapped radicals is mainly based on precise hfsc values originating from the spin trap moiety (in particular, the N- and F-hfsc values), which act as spectral fingerprints of the trapped radical. For instance, c-centered radical adducts have larger N-hfsc values than oxyl adducts (Janzen and Liu 1973; Khramtsov, Reznikov et al. 2001). In addition, the magnitude of F-hfsc can also be a useful marker for the identification of the FDMPO spin adducts, though it is not likely to vary in an easily predictable manner (i.e. not linearly dependent on the trapped radical adduct type).

Therefore, the primary goal of the development of an ANN is to create an effective tool to correlate N- and F-hfsc values with the structure of radical adducts. So, N- and F-hfsc values of the variety of radical adducts are used as input for the ANN. The output of the ANN is the pre-defined group of radical adducts. However, prior to the analysis of experimental data the ANN requires training. Training a network involves establishing a set of numerical weights that successfully connect a training input (FDMPO adduct hyperfine splitting constants) with a desired output (predefined group of radicals). Once trained, an artificial neural network can be an effective and rapid tool to reveal radical adducts that are not *a priori* known.

In order to provide a systematic manner for the classification of the radical adducts according to their chemical structure, several representative FDMPO radical adducts with well-determined parameters were taken from previously published data (Khramtsov, Reznikov et al. 2001) (Table 1). However, this data set was too small for the efficient training of the ANN, so the training set was extended with hyperfine splitting constant of 2-TFDMPO (Janzen, Zhang et al. 1995). The chemical structure of the 2-TFDMPO spin trap is similar to that of FDMPO. Therefore, the hyperfine splitting constants corresponding to the same radical adducts have similar values. For example,  $a_N = 13.9$  and  $a_F = 2.75$  of FDMPO/OH\* are very

comparable to  $a_N = 14.0$  and  $a_F = 2.7$  of 2-TFDMPO/OH\*, as well as hyperfine splitting constants of FDMPO/CH<sub>3</sub>\* ( $a_N=14.6$  and  $a_F=2.05$ ) and 2-TFDMPO/CH<sub>3</sub>\* (Figure 3, Table 1).

In Figure 3  $a_F$  has been plotted versus  $a_N$  for several FDMPO and 2-TFDMPO radical adducts (data from Table 2). One can clearly observe four groups based on a similar electronegative character of the free radical group attached to carbon-2 atom.

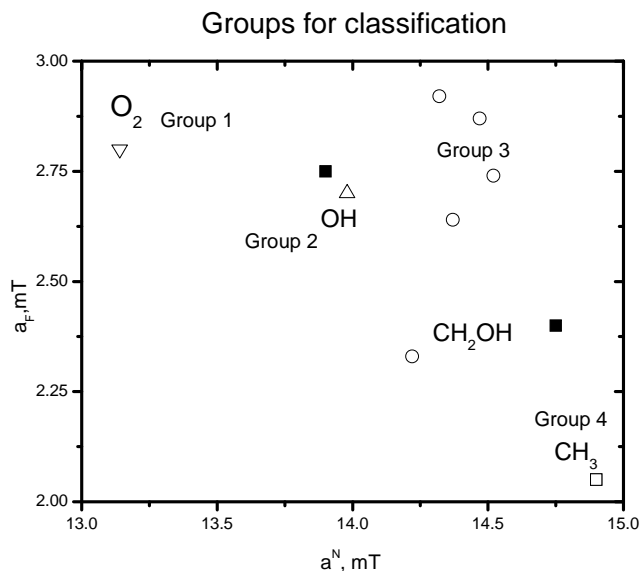


**Figure 3.** Plot of  $a_F$  vs  $a_N$  for groups of 2-TFDMPO (open symbols) and FDMPO (filled squares) radical adducts based on published F- and N-hfsc values (Janzen, Zhang et al. 1995; Khramtsov, Reznikov et al. 2001).

Group 1 (coded as [0,0] output of ANN) contains oxygen O<sub>2</sub>\* and OOH\* radicals.

Group 2 (coded as [1,0] output of ANN) includes only the hydroxyl (OH\*) radical where oxygen goes in combination with hydrogen. The radical adducts in group 1 and 2 with two electronegative (polar) groups attached to carbon-2 give relatively small N-hfsc values (Table 1). Radical adducts from Group 2 (OH\*) and Group 1 (O<sub>2</sub>\* and OOH\*) spin adducts could be distinguished based on N-hfsc values, since hydroxyl N-hfsc values are about 0.8 G larger than those of superoxide spin adducts. F-hfsc values are insensitive to changes in the trapped-radical structure showing a difference of approximately 0.1G for these two groups.

Group 3 (coded as [0,1] output of ANN) includes carbon-oxygen radical adducts with a CO (alkoxyl) group attached to carbon-2 i.e. hydroxymethyl radical (CH<sub>2</sub>OH\*), 1-hydroxyethyl radical (CH<sub>3</sub>CHOH\*) and etc. For this group only a small change is found in the N-hfsc values with different radical adduct structure, although the variation in F-hfsc values is about 0.6 G. The N-hfsc values of this group of radical adducts are 0.5 G smaller than the N-

hfsc values of group 4, and 0.5-1.5 G larger than the N-hfsc values of the 1st and the 2<sup>nd</sup> group.

Group 4 (coded as [1,1] output of ANN) includes radicals with the largest N-hfsc and the smallest F-hfsc values, and includes the carbon-centered spin adducts without oxygen (e.g.  $-\text{CH}_3^*$  and  $\text{CH}\equiv\text{C}^*$ ). The N-hfsc values are about 1-1.8 G larger (compared in the same solvent) and the F-hfsc values about 0.7 G smaller as compared to those from  $\text{OH}^*$  and  $\text{O}_2^*$  spin adducts.

Thus, in the case of FDMPO and 2-TFDMPO, the variation of the nitrogen and fluorine hyperfine splitting of radical adducts provides structural information mainly about the group attached not further away than three – four bonds from the nitrogen and fluorine atoms (e.g. CH, CO, OH and OO). The free radical groups can be described qualitatively as electron-donating groups or electron-withdrawing groups (Church 1986). Spin adducts with electron-donating free radicals favor a positive imbalance of spin density on  $^{14}\text{N}$  and exhibit larger N-hfsc values, whereas spin adducts with progressively stronger electron-withdrawing groups have smaller N-hfsc values and a smaller positive imbalance of spin density on  $^{14}\text{N}$ . This effect was studied for PBN-nitronyl- $\text{C}^{13}$  adducts (Haire, Krygsman et al. 1988), which exhibited larger N-hfsc values in case of a nonpolar  $\text{CH}_3^*$  radical adduct and smaller N-hfsc values in case of an  $\text{OH}^*$  radical adduct.

In addition to the chemical structure information, N- and F-hfsc values also reflect the polarity and proticity of the radical adduct environment. Generally, there is an increase in the N-hfsc with an increase in the polarity of the solvent (Owenius, Engstrom et al. 2001). Indeed, the N-hfsc value reported for the 2-TFDMPO/ $\text{CH}_2=\text{CH}$  spin adduct in water solvent ( $\epsilon=79$ ) is 1.5 G higher than the N-hfsc value in benzene ( $\epsilon=2.27$ ) (Janzen, Zhang et al. 1995). In case of the Fenton reaction and the Fenton reaction with DMSO, ethanol and methanol the changes in the polarity are rather small (Yang, Yang et al.; Harvey and Prausnitz 1987), so only a small variation of the N-hfsc values is expected.

The main advantage of an ANN is its ability to operate well on *a priori* “unknown” data, which makes the ANN a valuable and attractive tool for the analysis of systems generating new type of free radicals or systems in different solvents. An MLP with one hidden layer consisting of 55 nodes was always accurate enough for the identification of the group of similar FDMPO radical adduct structures on the basis of experimental N- and F-hfsc values. The network was trained with the training set for around 600 iterations, until the SSE between desired output and actual output of the ANN reached its lowest point (0.001). Being

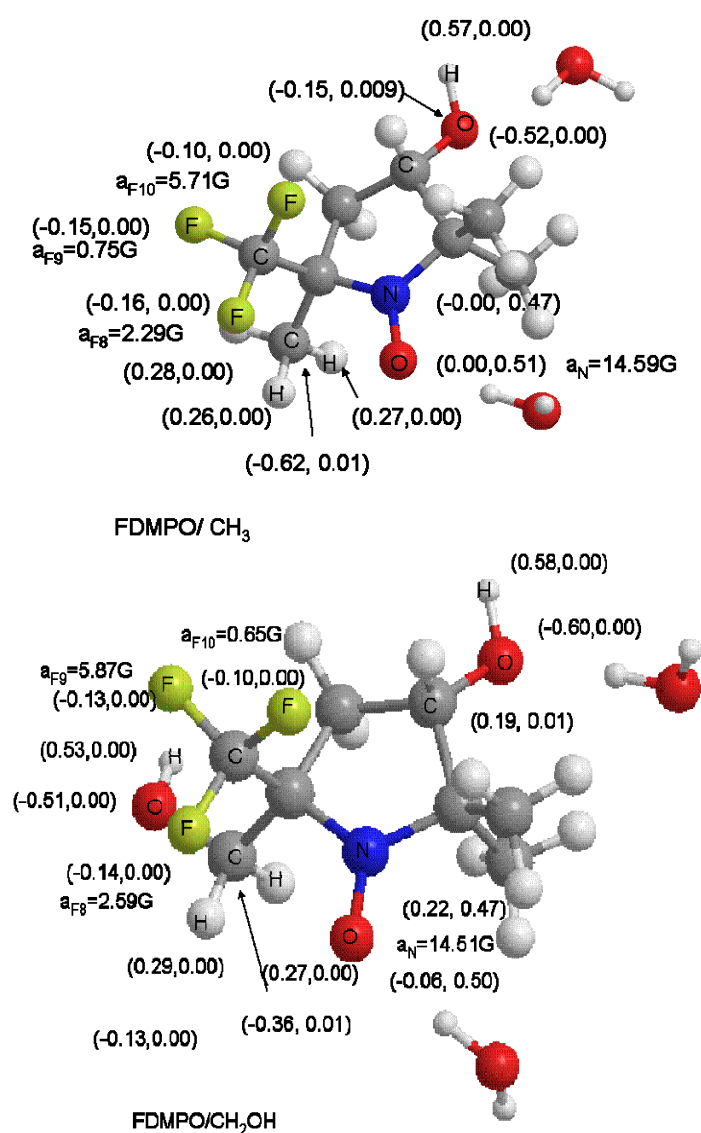
trained on the 2-TFDMPO data set, the ANN, due to its ability to generalize, performs well on the testing set of hyperfine splitting constants of FDMPO radical adducts from Table 1.

Subsequently, the F- and N-hfsc values extracted from the experimental ESR spectra of FDMPO spin adducts formed in the Fenton reaction with DMSO, methanol and in the PAA cleavage over MnO<sub>2</sub> (Table 2) were analyzed with this ANN. These experimental data contain additional details which are not captured in the training set. Such details include imperfect knowledge of the hyperfine splitting constants due to simulation error (0.05 G) and due to the different polarity of the solvents used. It was reported that the polarities of water/DMSO (Yang, Yang et al.), water/ethanol and water/methanol mixtures are slightly lower ( $\epsilon \sim 70$ ) than those of pure water ( $\epsilon = 79$ ). In any case, it appears that the MLP is very robust and quite capable of dealing with both indicated problems. The FDMPO/OH radical adduct was observed and successfully recognized by the ANN in all studied experimental systems, namely Fenton, Fenton reaction with methanol, ethanol, DMSO and also in the Mn/PAA system. The N- and F-hfsc values extracted by SBF varied in the range from 13.6 to 13.74 G and 2.59 to 2.84 G, respectively. In all cases the MLP performed well and assigned these pairs of hyperfine values to FDMPO/OH radical adduct (Table 2). The assignment of the c-centered radicals was also successful (Table 2). The c-centered radical adduct from the Fenton reaction with DMSO was assigned to group 4, and was associated with the FDMPO/CH<sub>3</sub> spin adduct. The c-centered radical adducts observed in the Fenton reaction with methanol and ethanol, FDMPO/CH<sub>2</sub>OH\* and FDMPO/CH<sub>3</sub>CH<sub>2</sub>OH\*, were successfully assigned by the MLP to the 3<sup>rd</sup> group. The c-centered spin adduct observed in the PAA system, namely FDMPO/CH<sub>3</sub>COO\*, was also assigned to group 3, notwithstanding the fact that the MLP was not trained to recognize this type of FDMPO spin adduct. However, in order to identify the radical adducts within the assigned group other methods are needed.

#### *4.3.3 ESR parameters of FDMPO spin adducts calculated by DFT*

DFT calculations are used to predict ESR parameters based on the chemical structure of a radical adduct. DFT calculations can be used as the next step of analysis within the group of radical adducts identified by ANN. The prediction of spin densities and N-hfsc values for various compounds bearing a nitroxyl moiety, for example, nitronyl nitroxides pyrrolidine *N*-oxides and piperidine *N*-oxide, has been reported using computational DFT methods. The B3LYP/EPR-II//B3LYP/6-31G(d)//B3LYP6-31++G level of theory has been employed previously to predict N-hfsc for various nitronyl nitroxides and they were found to be in good agreement with experimental values (Villamena, Hadad et al. 2004).

Figure 4 shows the optimized structures together with the charge and spin density distribution of FDMPO radical adducts as a result of DFT calculations. The calculated electron spin density is localized mainly on the nitroxide fragment (NO), whereas the spin densities on atoms of the pyrroline ring and the methyl and trifluoromethyl groups are insignificant. One can also observe in Figure 4 that the redistribution of the electron spin density induced by the trapped radical structure occurs mainly in the NO bond. Thus, only the nitroxide fragment of the FDMPO spin adducts was considered in more detail. With variation of radical adduct structure the total spin density (sum of N and O spin densities) in the nitroxide fragment slightly decreases (from 0.97 to 0.96 for  $\text{CH}_3^*$  and  $\text{OH}^*$  radicals, respectively).



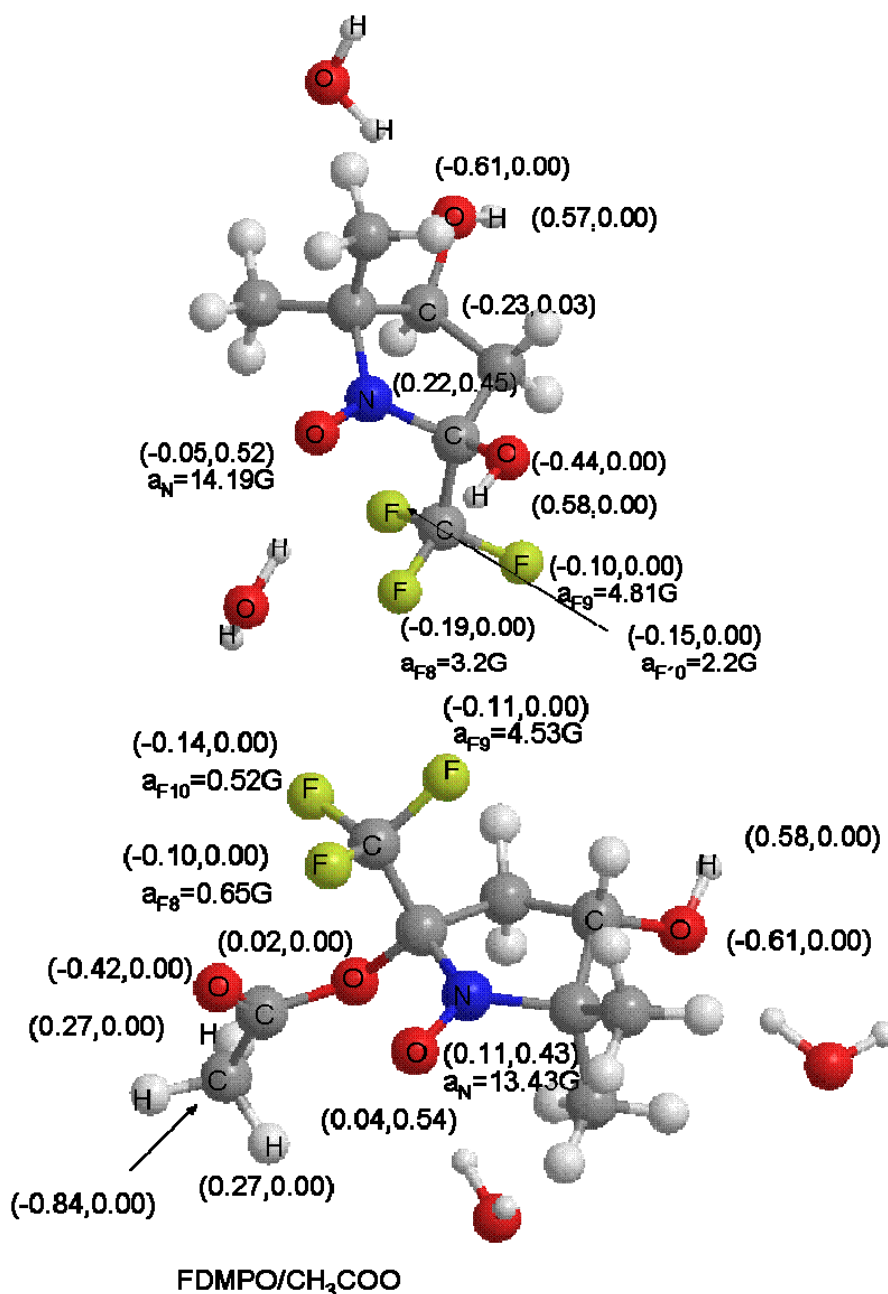


**Figure 4.** *F* and *N* hyperfine splitting constant values, charge and spin density populations (in parentheses) of CH<sub>3</sub>, OH, CH<sub>2</sub>OH and CH<sub>3</sub>COO spin adducts of FDMPO spin trap and two water molecules calculated at the B3LYP/6-31++G level of theory.

Qualitative interpretation of the spin density distribution in the nitroxide group is based on the localization/delocalization of the unpaired electron on the N and O atoms. An electron-withdrawing group (OH) removes electron density from the system and causes a decrease in the spin density of the N atom (0.44). In contrast, an electron donating group (CH<sub>3</sub>) adds electron density to the system and results in an increase of the spin density on N (0.47). The analysis of obtained N-hfsc values follows the general trend i.e. FDMPO spin



adduct with progressively stronger electron-withdrawing radicals (OH) exhibit smaller N-hfsc values (13.18G), while FDMPO with electron-donating CH<sub>3</sub> group exhibit an N-hfsc of 14.3 G.

The results of the calculation are shown in Table 3. Interestingly, the DFT calculations result in 3 different values for  $a_F$  for the trifluoromethyl group (2.28, 5.28 and 1.82 G for FDMPO/OH\*, respectively as shown at Figure 4). This is the consequence of the fact that the DFT calculations consider only one orientation of the trifluoromethyl group, whereas in an experimental system the trifluoromethyl group is allowed to rotate freely, so the F-hfsc values are averaged, resulting in the typical spectrum of a triplet, of which each line is split into a quartet with a 1:4:4:1 intensity ratio (Janzen, Zhang et al. 1995). However, when the rotation of the CF<sub>3</sub> group is limited due to interaction with solvent or with trapped radical, the spectrum will change dramatically. The phenyl adduct of 2-TFDMPO (Janzen, Zhang et al. 1995) exhibits an entirely different type of spectrum that consists of three groups of doublets with unresolved peaks, due to three different F-hfsc values.

In order to improve the results of the single point calculation, the dihedral angle of the trifluoromethyl group and of the pyrroline ring was changed, allowing rotation of the trifluoromethyl group only, as was done for bis-di(trifluoromethyl) nitroxide (Mattar, 2009). For each dihedral angle the single point calculations of the hyperfine splitting constants were performed using B3LYP/6-31++G level of theory. Subsequently, the Maxwell-Boltzman distribution was applied to calculate numerical values of the rotationally averaged hyperfine couplings. The total energy of the optimized geometries,  $E_{tot}$ , was used to determine the probability,  $p$ , that the radical adduct exists in a certain conformation with a specific dihedral angle  $\varphi$ :

$$p(\varphi) = \frac{\exp(-\frac{E_{tot}(\varphi)}{kT})}{\sum_{\varphi=0}^{120} \exp(-\frac{E_{tot}(\varphi)}{kT})} \quad (1)$$

These probabilities are used to weight the contribution of the hfsc at that angle in the calculation of the averaged isotropic hyperfine coupling constants via the mean value expression:

$$\langle a_{iso} \rangle = \sum_{\varphi=0}^{120} p(\varphi) a_{iso}(\varphi) \quad (2)$$

Subsequently, the averaged values from the  $\text{CF}_3$  group were used for comparison with experimental values. Rotation of the  $\text{CF}_3$  group influenced N-hfcs as well. The rotation averaged values of  $a_{\text{N}}$  and  $a_{\text{F}}$  are presented in the Table 3. Indeed, the averaging over the dihedral angle drastically improves the results of hyperfine splitting calculations. The averaged values of F-hfsc are only slightly overestimated by 0.1 and 0.4 G for FDMPO/OH and FDMPO/ $\text{CH}_3$  radical adducts respectively in comparison with the experimental values from Table 2.

**Table 3** Hyperfine splitting constants of various FDMPO spin adducts from DFT calculations at the B3LYP/6-31++G level of theory using the PCM model for the water solvent and 2 water molecules.

FDMPO radical adduct	$a_{\text{N}}, \text{G}$	$a_{\text{F}}, \text{G}$
$\text{CH}_3^*$	14.63	2.52
$\text{CH}_2\text{OH}^*$	14.43	2.45
$\text{OH}^*$	13.3	2.6
$\text{CH}_3\text{COO}^*$	13.27	1.99

In general, the ANN provides the direct assignment of an unknown radical adduct to the predefined group with similar structure. In contrast, the accurate and time consuming DFT calculations are generally applied to the known radical adduct structure in order to get more information about optimal geometry and the spin density distribution of the radical adduct. Additional calculations of spin adduct varying the optimized geometry allow to study in detail all the factors that influence magnetic parameters and evaluate their contributions.

#### 4.4 Conclusions

The N- and F-hyperfine splitting constants of FDMPO radical adducts were obtained via computer simulations. Identification of the FDMPO radical adducts observed in the Fenton reaction with methanol, ethanol, DMSO and the PAA cleavage over  $\text{MnO}_2$  was performed with an ANN. The ANN performed well with experimental data and tolerated the solvent effect on N- and F-hyperfine splitting constants. To verify the results of the ANN identification DFT calculations of the minimum energy geometry of  $\text{OH}^*$ ,  $\text{CH}_3^*$ ,  $\text{CH}_2\text{OH}^*$  and  $\text{CH}_3\text{OO}^*$  radical adducts of FDMPO spin trap have been performed. The charge and spin densities on N and O atoms as well as the N- and F-hyperfine splitting constants were calculated. Spin densities on N (0.47) are higher for the c-centered radical adducts as compared to those of hydroxyl adducts (0.44). This results in smaller N-hfsc values (13.18 G)

for the FDMPO/OH radical adduct and larger N-hfsc values for the FDMPO/CH<sub>3</sub> (14.6 G), FDMPO/CH<sub>2</sub>OH (14.5 G) and FDMPO/CH<sub>3</sub>OO radical adducts.

This study demonstrates that a combination of computer simulation based fitting of ESR spectra, ANN and DFT calculations allows a comprehensive analysis of FDMPO radical adducts. Computer simulations were used for the decomposition of the ESR spectra and extraction of hyperfine splitting constants. Then ANN-based identification was used for preliminary estimation of the radical adduct chemical structure. And finally the chemical structure could be verified by DFT calculations of hyperfine splitting constants. This approach is potentially important for the analysis of multi-component free radical systems with a variety of free radicals. The approach outlined here can easily be generalized to other radical adducts which exhibits overlapping ESR spectra.

## ACKNOWLEDGMENTS

This research was supported by the European Community activity Large-Scale Facility Wageningen NMR Center (FP6-2004-026164 (2006-2009). The ab initio calculations were performed with Gaussian 03 package in the Interdisciplinary Centre for Mathematical and Computational Modelling (Warsaw, Poland) under the computational Grant G14-6.



## REFERENCES

- Bacic, G., I. Spasojevic, et al. (2008). "Spin-trapping of oxygen free radicals in chemical and biological systems: New traps, radicals and possibilities." Spectrochim. Acta Mol. Biomol. Spectros. **69**(5): 1354-1366.
- Bishop, C. M. (1995). Neural networks for pattern recognition, Oxford University Press, Inc.
- Blake, D. R., R. E. Allen, et al. (1987). "Free radicals in biological systems: a review orientated to inflammatory processes." Br. Med. Bull. **43**(2): 371-385.
- Budil, D. E., S. Lee, et al. (1996). "Nonlinear-least-squares analysis of slow-motion EPR spectra in one and two dimensions using a modified Levenberg-Marquardt algorithm." J. Magn. Reson. **120**(2): 155-189.
- Busi, E., V. Travagli, et al. (2010). "Simulation of EPR spectra as a tool for interpreting the degradation pathway of hyaluronan." Appl. Magn. Reson. **37**(1): 325-337.
- Church, D. F. (1986). "Substituent effects on nitroxide hyperfine splitting constants." J. Org. Chem. **51**(7): 1138-1140.
- Corne, S. A., A. P. Johnson, et al. (1992). "An artificial neural network for classifying cross peaks in two-dimensional NMR spectra." J. Magn. Reson. **100**(2): 256-266.
- Dikalova, A. E., M. B. Kadiiska, et al. (2001). "An in vivo ESR spin-trapping study: Free radical generation in rats from formate intoxication—role of the Fenton reaction." PNAS **98**(24): 13549-13553.
- Fau, S. and R. J. Bartlett (2003). "Gaussian Basis Sets for Highly Accurate Calculations of Isotropic Hyperfine Coupling Constants at Hydrogen." J. Phys. Chem. A **107**(34): 6648-6655.
- Finkelstein, E. L. I., G. M. Rosen, et al. (1979). "Spin Trapping of Superoxide." Mol. Pharmacol. **16**(2): 676-685.
- Frisch, M. J., G. W. Trucks, et al. (2003). Gaussian 03, Revision C.02.
- Haire, L. D., P. H. Krygsmann, et al. (1988). "Correlation of radical structure with EPR spin adduct parameters: utility of the proton, carbon-13, and nitrogen-14 hyperfine splitting constants of aminoxyl adducts of PBN-nitronyl-13C for three-parameter scatter plots." J. Org. Chem. **53**(19): 4535-4542.
- Harvey, A. H. and J. M. Prausnitz (1987). "Dielectric constants of fluid mixtures over a wide range of temperature and density." J. Solution Chem. **16**(10): 857-869.
- Israelachvili, J., J. Sjösten, et al. (1975). "ESR spectral analysis of the molecular motion of spin labels in lipid bilayers and membranes based on a model in terms of two angular

- motional parameters and rotational correlation times." Biochim. Biophys. Acta **382**(2): 125-141.
- Janzen, E. G. (1971). "Spin trapping." Acc. Chem. Res. **4**(1): 31-40.
- Janzen, E. G. (1998). Spin trapping. Foundations of modern EPR. G. R. Eaton, S. S. Eaton and K. M. Salikhov, Singapore: World Scientific.
- Janzen, E. G. and G. Liu (1973). "Factors influencing hyperfine splitting in the ESR spectra of five-membered ring nitroxides." J. Magn. Res. **9**: 513-517.
- Janzen, E. G., Y.-K. Zhang, et al. (1995). "Synthesis and spin-trapping chemistry of 5,5-dimethyl-2-(trifluoromethyl)-1-pyrroline n-oxide." J. Org. Chem. **60**(17): 5434-5440.
- Jerzykiewicz, M., I. Cwielag-Piasecka, et al. "EPR spin trapping and DFT studies on structure of active antioxidants in bioglycerol." Chem. Phys. Lett. **497**(1-3): 135-141.
- Khramtsov, V. V., V. A. Reznikov, et al. (2001). "NMR spin trapping: detection of free radical reactions with a new fluorinated DMPO analog." Free Radic. Biol. Med. **30**(10): 1099-1107.
- Kirste, B. (1992). "Methods for automated analysis and simulation of electron paramagnetic resonance spectra." Anal. Chim. Acta **265**(2): 191-200.
- Nelder, J. A. and R. Mead (1965). "A simplex method for function minimization." Comp. J. **7**(4): 308-313.
- Owenius, R., M. Engstrom, et al. (2001). "Influence of solvent polarity and hydrogen bonding on the EPR parameters of a nitroxide spin label studied by 9-GHz and 95-GHz EPR spectroscopy and DFT calculations." J. Phys. Chem. A **105**(49): 10967-10977.
- Rokhina, E. V., K. Makarova, et al. (2010). "Free radical reaction pathway, thermochemistry of peracetic acid homolysis, and its application for phenol degradation: spectroscopic study and quantum chemistry calculations." Environ. Sci. Technol. **44**(17): 6815-6821.
- Rosenblatt, F. (1958). "The perceptron: a probabilistic model for information storage and organization in the brain." Psychol. Rev. **65**(6): 386-408.
- Roth, M. W. (1990). "Survey of neural network technology for automatic target recognition." Neural Networks, IEEE Transactions on **1**(1): 28-43.
- Rumelhart, D. E., G. E. Hinton, et al. (1986). "Learning representations by back-propagating errors." Nature **323**(6088): 533-536.
- Stoll, S. and A. Schweiger (2006). "EasySpin, a comprehensive software package for spectral simulation and analysis in EPR." J. Magn. Reson. **178**: 42-55.
- Tomasi, J., B. Mennucci, et al. (2005). "Quantum mechanical continuum solvation models." Chem. Rev. **105**(8): 2999-3094.

- Villamena, F. A., C. M. Hadad, et al. (2004). "Theoretical study of the spin trapping of hydroxyl radical by cyclic nitrones: a Density Functional Theory approach." J. Am. Chem. Soc. **126**(6): 1816-1829.
- Wasserman, P. D. (1989). Neural computing: theory and practice / Philip D. Wasserman. New York :, Van Nostrand Reinhold.
- William, M. (1986). Introduction to probability and statistics (7th ed.), Duxbury Press.
- Yang, L.-J., X.-Q. Yang, et al. Dielectric Properties of Binary Solvent Mixtures of Dimethyl Sulfoxide with Water, Molecular Diversity Preservation International (MDPI).





## Chapter 5

### FREE RADICAL REACTION PATHWAY, THERMOCHEMISTRY OF PERACETIC ACID HOMOLYSIS AND ITS APPLICATION FOR PHENOL DEGRADATION: SPECTROSCOPIC STUDY AND QUANTUM CHEMISTRY CALCULATIONS

Ekaterina V. Rokhina, Katerina Makarova, Elena A. Golovina, Henk Van As,  
Jurate Virkutyte

Published in *Environmental Science and Technology*

#### ABSTRACT

The homolysis of peracetic acid (PAA) as a relevant source of free radicals (e.g.  $\bullet\text{OH}$ ) was studied in details. Radicals formed as a result of chain radical reactions were detected with electron spin resonance and nuclear magnetic resonance spin trapping techniques and subsequently identified by means of the simulation based fitting approach. The reaction mechanism, where hydroxyl radical was a primary product of O-O bond rupture of PAA was established, with a complete assessment of relevant reaction thermochemistry. Total energy analysis of the reaction pathway was performed by electronic structure calculations (both *ab initio* and semiempirical methods) at different levels/basis sets (e.g. HF/6-311g(d), B3LYP/6-31G(d), etc.). Furthermore, the heterogeneous  $\text{MnO}_2$ /PAA system was tested for the elimination of a model aromatic compound - phenol. An artificial neural network (ANN) was designed to associate the removal efficiency of phenol with the process parameters such as concentration of both the catalyst and PAA and the reaction time. Results were used to train and test ANN to identify an optimized network structure which represented the correlations between the operational parameters and the removal efficiency of phenol.

## 5.1 Introduction

Advanced oxidation processes (AOPs) is a group of chemical oxidation processes, which use various oxidants (mainly ozone ( $O_3$ ) and hydrogen peroxide ( $H_2O_2$ )) to produce hydroxyl radicals ( $\bullet OH$ ). Hydroxyl radical is known as one of the most powerful oxidizing agents, capable of attacking a wide range of organic pollutants with rate constants in the order of  $10^6$  to  $10^9 \text{ M}^{-1} \text{ s}^{-1}$  (Rey, Faraldos et al. 2009). Despite of a great number of currently available AOPs (e.g.  $O_3$  and  $H_2O_2$ , ultraviolet (UV) and ultrasound (US) irradiations as well as their combinations), there is still a continuous search for the new and more effective strategies to generate hydroxyl radicals.

Peracetic acid (PAA) has been known as a disinfectant agent due to its bactericidal, virucidal, fungicidal, and sporicidal effectiveness as demonstrated in various applications (Koivunen and Heinonen-Tanski 2005). The desirable attributes of peracetic acid are the ease of treatment implementation, broad spectrum of activity, absence of persistent toxic or mutagenic residuals as well as by-products, small dependence on pH fluctuation, and short contact time (Kitis 2004). However, the exact PAA oxidation mechanism is still controversial due to the complexity of the reaction pathway. Recently, Adeola and co-workers (2004) compared the use of hydrogen peroxide – activated acetic acid and commercially available PAA for the disappearance of  $\alpha$ -methylnaphthalene or benzo[*a*]-pyrene in the aqueous phase. They reported that peracetic acid degraded parent compounds faster than the combination of acetic acid and hydrogen peroxide, probably due to the different reaction pathways, unfortunately not yet understood (N'Guessan, Carignan et al. 2004). Therefore, a systematic comprehension of basic reactions involved in the PAA oxidation process is critically needed to evaluate the potential of peracetic acid as a relevant  $\bullet OH$  source. Generally speaking, homolysis of peracetic acid is much more complex process in terms of free radicals generation in comparison to the traditional AOPs, due to that several radical species with different reaction abilities are produced (Lubello, Gori et al. 2004). A rate constant of  $6 \times 10^{-12} \text{ s}^{-1}$  can be estimated for O-O bond rupture of PAA at 25 °C that is consistent with a very low rate of bond dissociation in the gas phase or in the absence of a catalytic influence (Bach, Ayala et al. 1996). Moreover, in the presence of UV irradiation, PAA undergoes UV photodissociation in a manner similar to the hydroperoxides based upon the likelihood of the stepwise O-O reaction (Keller, Wojcik et al. 2008). Subsequently, a similar principle can be suggested for PAA dissociation in the presence of the eligible catalyst (as in widely accepted and researched Fenton reaction) leading to the formation of various radical species with

different reactivity, which are able to attack the target compound and oxidize it to less hazardous products. However, there is a lack of studies of the radical reactions occurring during PAA oxidation of organic contaminants. Therefore, the profound understanding of PAA homolytic cleavage and the subsequent reactions is essential due to the use of such a specific oxidant that is able to produce radicals with different activity may have a great utility (N'Guessan, Carignan et al. 2004).

Emerging evidence of the radical reaction pathway may be obtained by means of the spin trapping (ST) technique with electron spin resonance (ESR) and nuclear magnetic resonance (NMR) spectroscopy (Bacic, Spasojevic et al. 2008). The ST technique is based on the trapping of short-lived/unstable free radical by a nitrono compound (spin trap) to form a relatively stable paramagnetic product – spin adduct, which can be easily detected by the conventional spectroscopic methods. High sensitivity renders ESR useful for free radical investigations in a great number of chemical and biological systems (Bacic, Spasojevic et al. 2008). However, the major limitation of ESR ST technique is the accurate interpretation of the generated spectra (Villamena, Locigno et al. 2006). ESR spectra often require simulations to extract parameters, needed for the interpretations of the spin trapping results. One of the approaches is simulation-based fitting (SBF), a standard tool for the analysis of experimental spectra obtained in complex chemical and biophysical systems (Nazarov, Apanasovich et al. 2004). The purpose of SBF is the approximation of experimental data by the available synthetic data obtained via mathematical modeling.

Another drawback of the ESR methods is the finite lifetime of the paramagnetic species (spin adducts), which are formed as a result of spin trapping. Many degradation/decomposition reactions of spin adducts lead to the formation of diamagnetic products, which are undetectable by the ESR, however they can be detected by NMR spectroscopy (Khramtsov, Berliner et al. 2001). Contrary to the ESR spectra, the NMR spectra are represented as distinct sharp peaks at various chemical shifts, which ease the identification of the detected species even for the complex systems (Argyropoulos, Li et al. 2006). Thus, both methods compensate each other's drawbacks – the ESR detectable spin adducts are stable over a long period of time after a conversion into their final diamagnetic forms and thus, are suitable for NMR measurements (Argyropoulos, Li et al. 2006).

In this study, phenol was chosen as a model aromatic molecule. The major aims of the current research were to comprehensively study the homolysis of PAA, including theoretical and practical approaches. The primary aim was to assess the generated radical species using both, ESR and NMR spectroscopy spin trapping (ST) with the subsequent identification by

simulation-based fitting (SBF) technique. The secondary aims were: (1) to develop the thermodynamically justified reaction mechanism based on the experimental results and quantum chemistry calculations, such as semiempirical and *ab initio* density functional theory (DFT) calculations; and (2) to estimate main practical aspects of phenol oxidation with PAA catalyzed by MnO<sub>2</sub>, such as the influence of the reaction parameters as encoded relationships between the process variables organized as inputs and outputs of an artificial neural network (ANN). Shortly, ANN is the comprehensive approach of the data treatment by detecting the patterns and relationships in data, which allows to account the interaction effects between the optimized parameters. Herein, ANN was build and trained to predict the process efficiency based on the variability of the process parameters.

## 5.2 Experimental Section

### 5.2.1 Instrumental.

The experiments were carried out in a 100 mL batch reactor equipped with a magnetic stirrer and a temperature controller. The reaction mixture was stirred at a speed of 800 rpm for 0-180 min. to provide a complete mixing for uniform distribution and full suspension of the catalysts particles (MnO<sub>2</sub>). The commercially available MnO<sub>2</sub> ( $S_{\text{BET}} = 3.375 \text{ m}^2 \text{ g}^{-1}$ ), peracetic acid (PAA), phenol and DTPA (diethylene triamine pentaacetic acid) were purchased from Sigma Aldrich and the nitron spin trap DIPPMPO (5-diisopropoxyphosphoryl-5-methyl-1-pyrroline N-oxide) from Alexis Biochemicals. All the chemicals were of laboratory reagent grade and used without further purification. Solutions were prepared using high purity deionized water (>17.7 MΩ). The reactants were added simultaneously at the beginning of each run. For experiments, unless specified otherwise, untreated catalyst (0.1–3 gL<sup>-1</sup>) was introduced as a suspension to the reaction medium with the following PAA (0.5-10 %) addition at various concentrations. Samples were taken at regular intervals (10 min.) for the subsequent analysis and filtered through a syringe filter (0.45 μm hydrophilic Millipore filter) to separate the catalyst particles from the solution. Control experiments were conducted for the optimum concentrations of reagents and samples were taken every 5 minutes. The pH of the filtrate was then determined by a pH meter (3401 WTW, Germany). The degradation of phenol was monitored by UV–Vis spectroscopy at  $\lambda = 268.4 \text{ nm}$  (Perkin Elmer UV–Vis Spectrometer Lambda 45, US) (Rokhina, Lahtinen et al. 2009). The specific surface area of the catalyst was measured and calculated according to the BET method on a Quantachrome Autosorb 1 analyzer (Quantachrome instruments, UK) with liquid nitrogen at -196 °C.

X-band ESR spectra were recorded on an ELEXYS E500 (Bruker, Germany) spectrometer with 100 kHz field modulation. Typical instrument settings were 5 mW microwave power and a modulation amplitude of 1 G or less. Spectra simulations were performed with the “EasySpin” toolbox for MATLAB distributed by Stefan Stoll (Stoll and Schweiger 2006).

For  $^{31}\text{P}$  spectra 560 scans were recorded at room temperature on a 7.1 T Bruker Avance NMR spectrometer using a basic single pulse sequence without proton decoupling. Trimethylphosphate was used as the internal standard for quantification and was added to the sample prior to measurement. Ascorbate (10 mM) was added to the reaction system before NMR study in order to convert radical adducts to the NMR detectable diamagnetic hydroxylamines.

### 5.2.2 ANN computation.

For the details see Supporting Information.

### 5.2.3 Quantum Chemistry Calculations.

All the calculations were carried out with 6-31G(d) and 6-311G(d) at the B3LYP level of theory using Gaussian 03 suite of programs. The optimized structures were set at minimum of the potential energy hypersurfaces by the vibrational frequency analysis. Enthalpies of the reactions were calculated as described elsewhere (Ochterski 2000). PAA heat of formation was calculated by an atomization method (Ochterski 2000). These calculations determined the total atomization enthalpy, and the computed heat of formation was then obtained in combination with the calculated and experimental heat of formation of the atoms C, H and O. The experimental data used were the JANAF values of C ( $169.73 \text{ kcal mol}^{-1}$ ), H ( $50.62 \text{ kcal mol}^{-1}$ ), O ( $58.99 \text{ kcal mol}^{-1}$ ) (Curtiss, Raghavacharin et al. 1997).

## 5.3 Results and Discussion

### 5.3.1 Detection of Free Radicals.

In highly complex free radical systems it is of paramount importance to use techniques, such as ESR that enable an accurate identification of formed radicals. However, an extreme caution must be exercised when interpreting the results of ESR experiments with spin traps, since several routes exist, whereby various radical adducts may arise (Clément, Gilbert et al. 1998). To overcome the aforementioned drawbacks, the performance of phosphorylated spin trap DIPPMPO (5-diisopropoxy-phosphoryl-5-methyl-1-pyrroline-N-oxide) was evaluated,

because of its ability to differentiate between various trapped radicals due to the additional  $^{31}\text{P}$  hyperfine splitting constant (Mojovic, Spasojevic et al. 2005). The presence of the  $\beta$ -isopropoxyphosphoryl group shielded the unpaired electron of the NO in a spin adduct, thus increasing the stability of adducts that can be detected by EPR spectroscopy (Figure S1). Moreover, DIPPMPO contained NMR active  $^{31}\text{P}$ , which facilitated NMR spectroscopy in addition to ESR. The reaction mechanism of spin trapping with the subsequent assignment of diamagnetic and paramagnetic products is shown in the Supporting Information (Scheme S1).

Representative  $^{31}\text{P}$ -NMR spectrum of the reaction medium after the addition of all the reagents to the reaction system is shown as an inset in Figure 1. The spectrum consists of two main peaks at different chemical shifts. The small peak at 25.3 ppm can be attributed to the reduced hydroxyl adduct DIPPMPO/OH (Khramtsov, Berliner et al. 2001), while another peak at 22.2 ppm originates from diamagnetic DIPPMPO itself (Argyropoulos, Li et al. 2006). These data confirm the presence of hydroxyl radical in the reaction system as a primary radical product of PAA homolytic cleavage. To establish the secondary products of the subsequent radical chain reactions, the system was further studied with ESR.

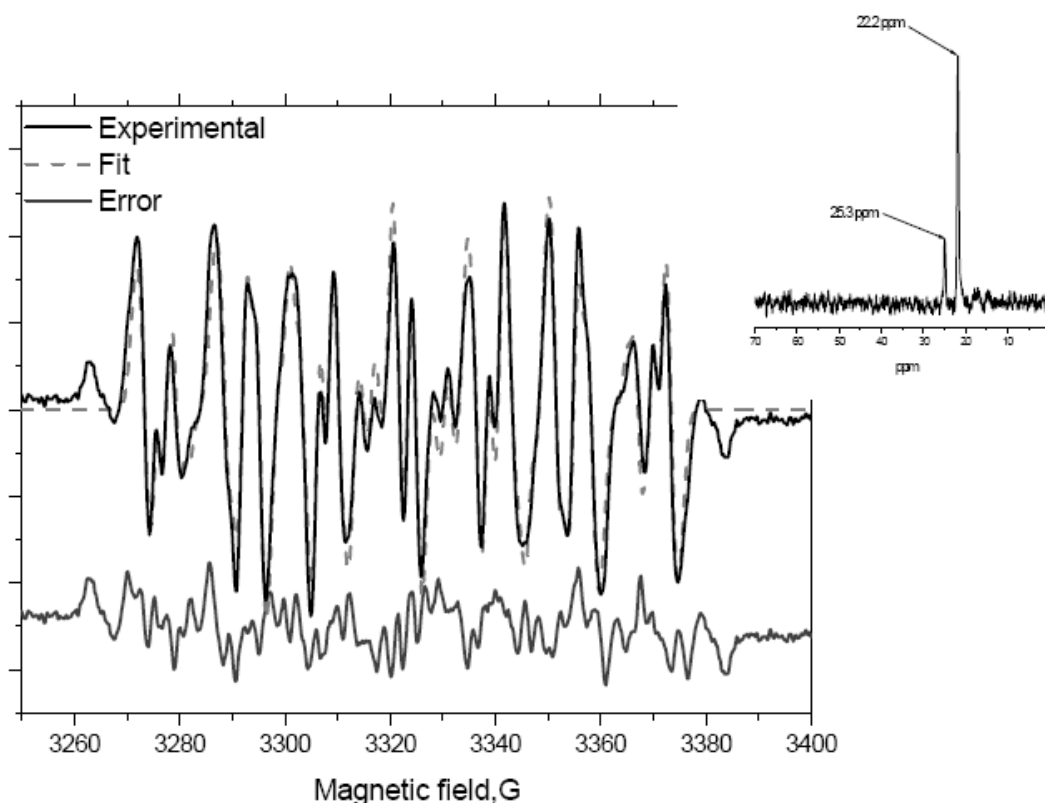


**Figure 1** Experimental and simulated ESR spectra of PAA cleavage over  $\text{MnO}_2$  with DIPPMPO with incorporated NMR spectra (ESR parameters were as follows: 20 mW microwave power, 20.48 ms time constant, 81.92 conversion time, 0.5 G modulation)

amplitude, sweep width 100G,  $^{31}\text{P}$  NMR parameters were recorded with 256 of total scans with acquisition time of 1.60 s.).

Figure 1 shows the ESR spectrum (solid line) recorded for the reaction system containing PAA,  $\text{MnO}_2$  and DTPA in the presence of DIPPMPO. The spectra consisted of 12 major ESR lines, which were composite due to superposition of the signal of the different adducts. Simulations were performed to extract the values of hyperfine splitting constants ( $a_{\text{P}}$ ,  $a_{\text{N}}$  and  $a_{\text{H}}$ ) for the radical identification (see Supporting Information for details). Based on this approach, the values of the simulated splitting constants of spectral components indicate the hydroxyl adduct as the main component and several carbon centered adducts (Table 1). The simulated spectrum (Fig. 1, dash line) does not significantly differ from the experimental spectra (Fig. 1, solid line). There were some additional spectral lines detected, which could be seen at the bottom of Figure 1b, however, their contribution to the overall spectral intensity was negligible and therefore was ignored.

**Table 1.** ESP parameters of DIPPMPO spin trapping for the assessment of free radicals in  $\text{MnO}_2/\text{PAA}$  system

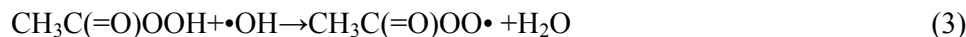
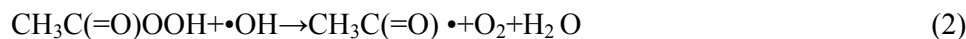
Compound	Spin adduct parameters			Reference
	$a_{\text{P}}, \text{G}$	$a_{\text{N}}, \text{G}$	$a_{\text{H}}, \text{G}$	
Compound 1	47.1	14.8	22.3	Current study
$\bullet\text{CH}_3$	47.1	14.4	22.6	Charlier and Tordo, 2002
Compound 2	49.5	14.8	22.2	Current study
$\bullet\text{CH}_3\text{C}(=\text{O})$	49.0	14.2	21.2	Charlier and Tordo, 2002
Compound 3	46.7	14.1	13.3	Current study
$\bullet\text{OH}$	46.8	14.0	13.2	Charlier and Tordo, 2002
	46.5	14.1	13.5	Villamena et al. 2003
Compound 4	49.7	14.0	11.0	Current study
$\text{CH}_3\text{OO}\bullet$	50.2	13.2	11.1	Charlier and Tordo, 2002
Compound 5	50.9	10.2	13.9	Current study
$\text{CH}_3\text{C}(=\text{O})\text{O}\bullet$				

### 5.3.2 Formation Mechanism of Detected Radicals.

Herein, the radical formation mechanism that is significant to the overall AOP efficiency is introduced. Relatively short chains are involved in the homolytic cleavage of peracetic acid. The initiation reaction involves the homolysis of PAA peroxy bond into two primary radicals: acyloxy and hydroxyl radicals according to the reaction proposed by Heywood and colleagues in 1961 (Heywood, Phillips et al. 1961):



As a result, formed hydroxyl radical is able to attack not only the organic pollutant but also the PAA molecule as well:



Meanwhile, the primary acyloxy radical, which is very unstable, tends to dissociate to methyl radical and carbon dioxide according to monomolecular decarboxylation:



However, in the reactions where the carbon-centered radical is resonance stabilized, the reaction is reversible and is followed by the interaction of methyl radicals with oxygen to produce a weak peroxy radical (El-Agamey and McGarvey 2003):



This reaction is relatively fast in oxygen saturated environments and therefore, the amount of methyl radicals in the reaction system is limited (Shi and Li 2007).

Hydroxyl radical formed as a primary radical, simultaneously reacts with  $\text{CH}_3\text{C}(=\text{O})\text{O}\bullet$  to generate a new PAA molecule, therefore re-starting the new oxidation cycle (Ciotti, Baciocchi et al. 2008):



It is important to note that all the generated radical species are able to interact with the target organic compound (e.g. phenol), contributing to its oxidation.

### 5.3.3 Thermochemistry of free radicals formation in $\text{MnO}_2/\text{PAA}$ system.

Peracetic acid is weaker than carboxylic acids, which can be attributed to intra-molecular hydrogen bonding (Keller, Wojcik et al. 2008). Moreover, the electrophilic activity of PAA highly depends on an opportunity of both, the heterolytic and homolytic ruptures of the O-O bond. Therefore, in order to assess the homolytic cleavage of PAA, the thermochemistry of the proposed free radical reaction was estimated.

The making and breaking of bonds is the basis of all the chemical transformation. A sound knowledge of energies required to break bonds and energies released upon their formation is fundamental to understand the chemical processes (Blanksby and Ellison 2003). The molecular bond lengths used in the current study (Table S4) were in a good agreement with the previously reported values (Sicilia, Maio et al. 1993). Heat of formation that was assessed by the group additivity methods (accuracy of calculation was within  $1\text{--}2 \text{ kcal mol}^{-1}$ ) was  $-82 \text{ kcal mol}^{-1}$  for PAA, where the O-O bond dissociation energy was  $42.5 \text{ kcal mol}^{-1}$ .



These two values were used to determine the energy of PAA homolysis that produced radicals. However, calculations performed by adopting the atomization approach at HF/6-31g(d) level of theory, indicated the heat of formation of PAA nearly  $-76.7$  kcal mol $^{-1}$ , whereas the O-O bond dissociation energy was 48 kcal mol $^{-1}$ . It was reported that the heat of formation of PAA and its radical products might vary by more than 1–2 kcal mol $^{-1}$ , but this should have little effect upon the relative available energies (Rokhina, Lahtinen et al. 2009). The obtained data allowed to construct the energy diagram for the radical reaction pathway (Figure 2). As could be seen in Figure 2, secondary decomposition was the major source of energy in this pathway. The heat of formation of C(O)OOH was determined by subtracting the methyl radical heat of formation from that of PAA and by adding 94 kcal mol $^{-1}$  for the C-C bond strength.

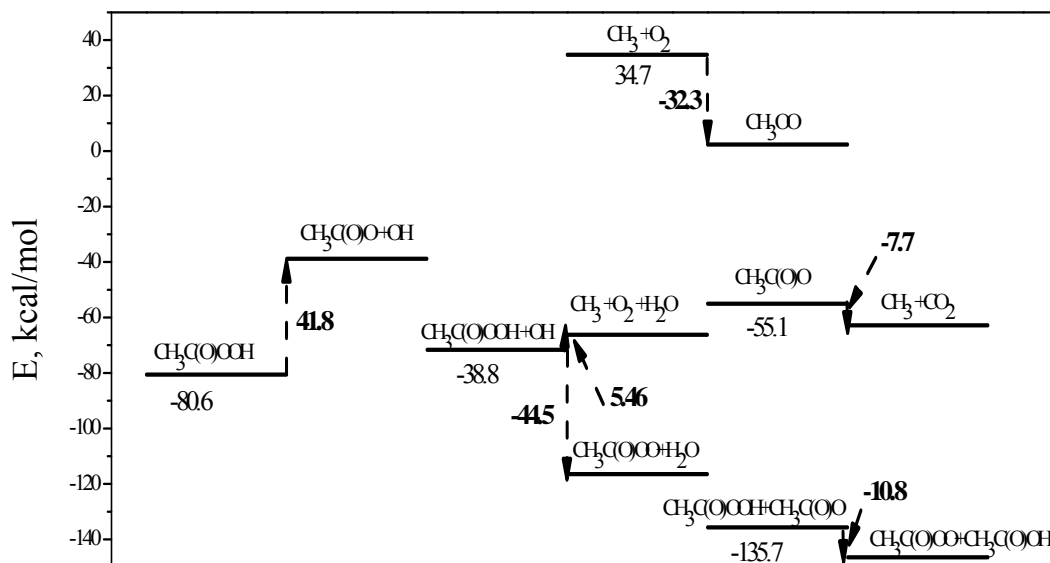


**Figure 2** Energy profile of free radicals formation scheme in heterogeneous MnO<sub>2</sub>/PAA system.

The calculation revealed that all the proposed reactions were thermodynamically possible. The homolysis of the PAA peroxy bond produced two primary radicals with unknown activation barrier (Shi and Li 2007). The subsequent formation of secondary radicals (reactions [2-5]) was nearly spontaneous. In the MnO<sub>2</sub>/PAA radical system, the attack of the target molecule by the hydroxyl and acyloxy radicals was a process with low activation barrier (Shi and Li 2007). Therefore, the rate determining step in the catalytic PAA oxidation

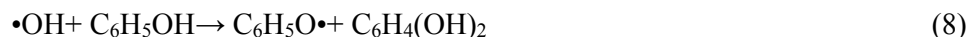
process should be the formation of primary radicals via reaction [1]. Furthermore, such formation of primary radicals can be caused by the higher barriers required for the peroxy bond homolysis (Shi and Li 2007).

#### 5.3.4 Phenol oxidation by MnO<sub>2</sub>/PAA system.

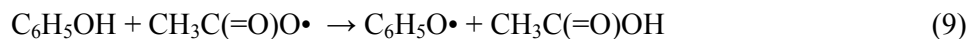
According to the reactions [1 – 5], free radicals that participated in the oxidation of phenol were •OH, CH<sub>3</sub>C(=O)O• and •CH<sub>3</sub>. However, the input of •CH<sub>3</sub> was rather limited due to the lower reaction constant (in the range of 10<sup>6</sup> s<sup>-1</sup> and 10<sup>9</sup> s<sup>-1</sup> for k<sub>•CH<sub>3</sub></sub> and k<sub>•OH</sub>, respectively) and limited availability in oxygen saturated environments (Shi and Li 2007). Indeed, •CH<sub>3</sub> reaction rate complemented the hypothesis that the competition between the interaction of •CH<sub>3</sub> radical and phenol as well as •CH<sub>3</sub> disappearance occurred. The primary mechanism of phenol decomposition was via abstraction of an H-atom from the substrate:



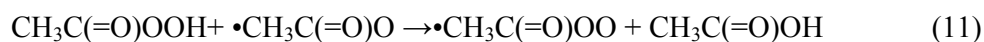
The substrate radical (C<sub>6</sub>H<sub>5</sub>O•) can also be formed by the attack of hydroxyl and acyloxy radicals. The thermochemistry of MnO<sub>2</sub> catalyzed reaction revealed the electrophilic attack of the •OH radical in *para* position with the subsequent formation of an unstable dihydroxyphenyl radical. During the next step, hydrogen abstraction occurred through another •OH radical, giving rise to the stable intermediates 1,2-benzenediol (catechol) and 1,4-benzenediol (hydroquinone) (Morales-Roque, Carrillo-Cárdenas et al. 2009).



It should be noted that formed acyloxy radicals can also attack phenol and initiate the formation of ring-cleavage products (Gonzalez Cuervo, Kozlov et al. 2004):



Acetic acid can also be formed as a result of the recombination between the organic radicals leading to the formation of coupling products:



#### 5.3.5 ANN Model Development.

In the absence of either catalyst or PAA, no phenol removal was observed and both reagents were found to be completely inert towards the degradation of phenol, when applied separately. Due to the complexity of the system under study, only the most significant process

parameters such as the reagent concentrations and the reaction time were considered as essential for the experimental design.

The optimized ANN structure is depicted in Figure 3. For the ANN modeling, one layer of hidden-neurons was used. The developed ANN was characterized by one hidden layer containing seven neurons. Correlations were obtained from the database with a confidence level of 98.64%. The overall optimization error was less than 5%. After optimization it was possible to quantify the effect of each experimental variable and collect the removal efficiencies.

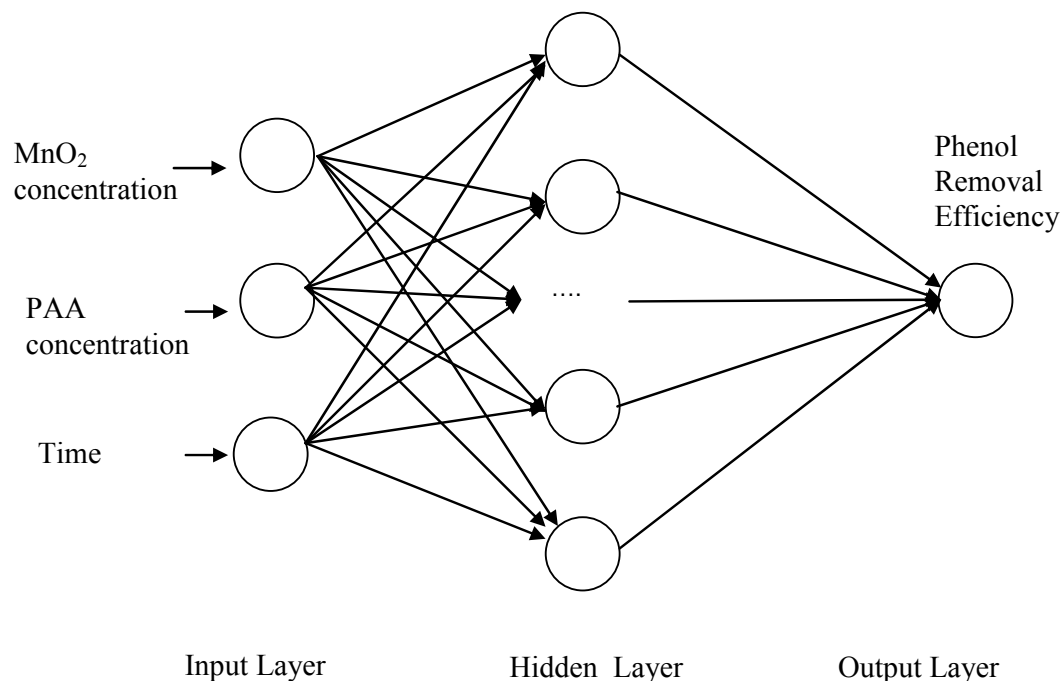
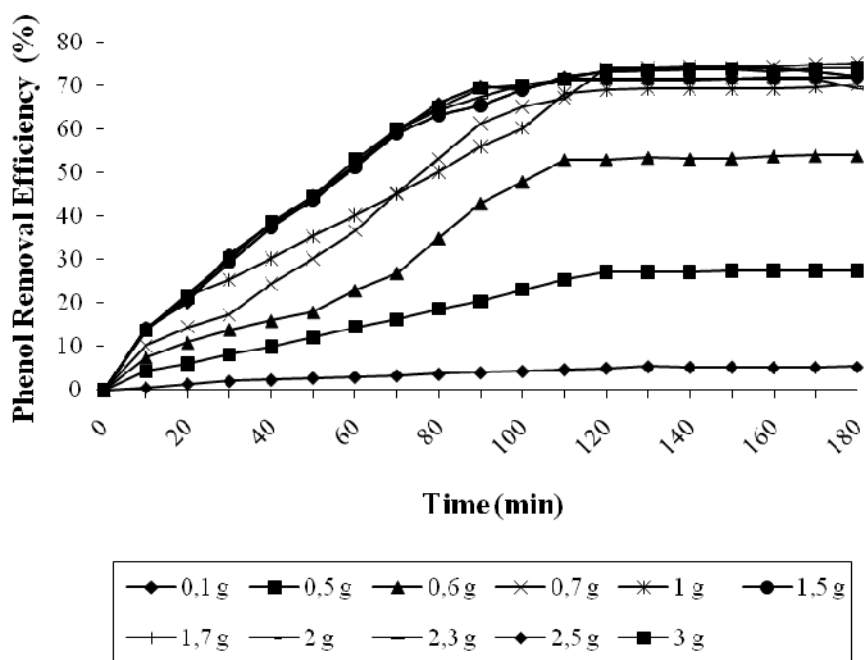
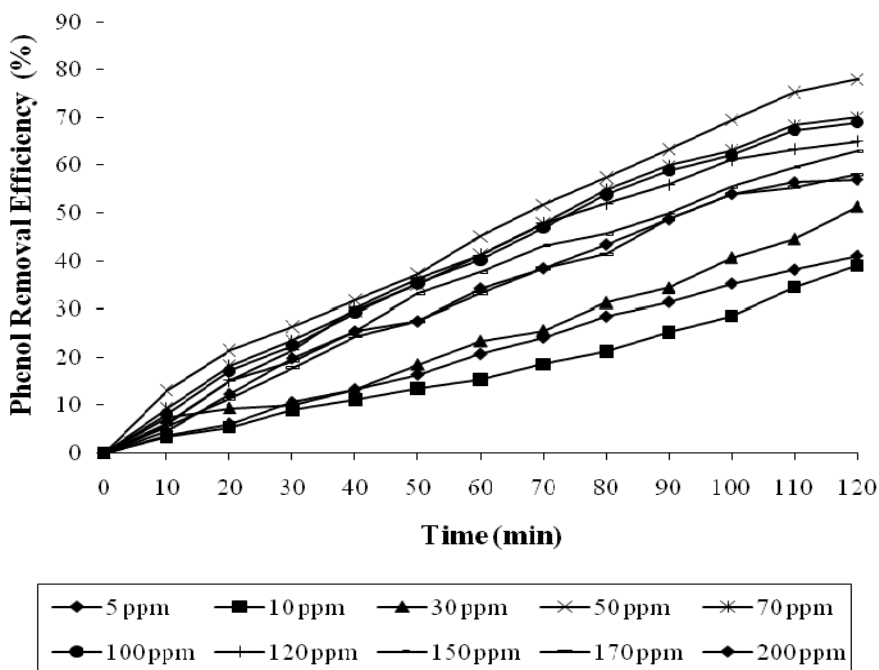


**Figure 3** ANN optimized structure.

Figure 4 (a, b) presents the predicted phenol removal efficiency with PAA and in the presence of heterogeneous catalyst  $\text{MnO}_2$ , for a wide range of the catalyst and PAA concentrations and for different treatment durations. It was observed that an increase in the process parameters significantly decreased the removal efficiency. The increase in the removal efficiency was observed only when the reaction proceeded for 120 min., therefore 120 min. was adopted as the optimal process time. The plots summarizing the main effects are depicted in Figure 5.



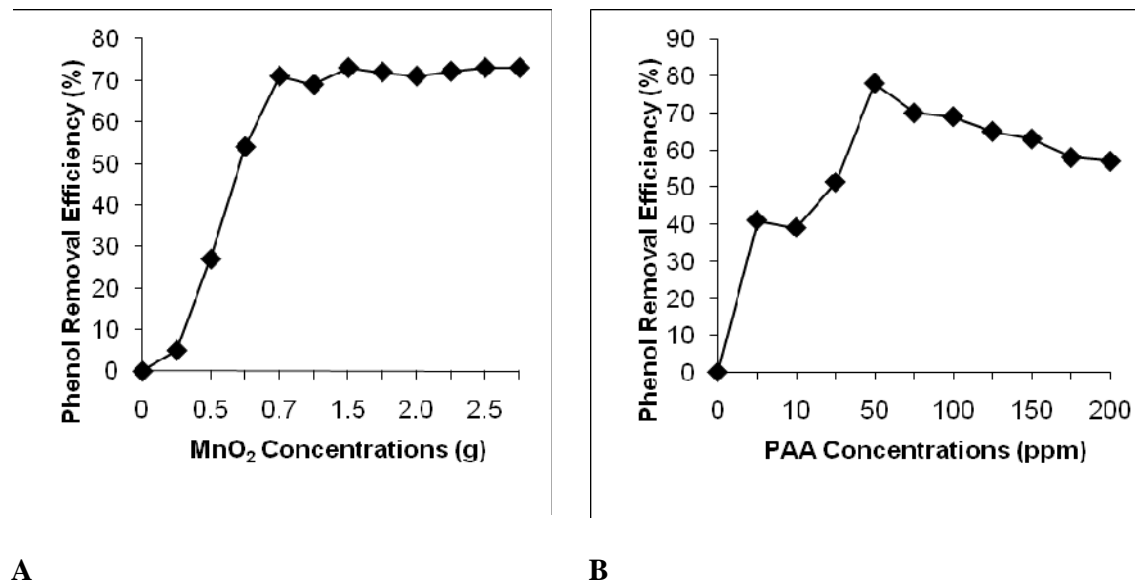
A

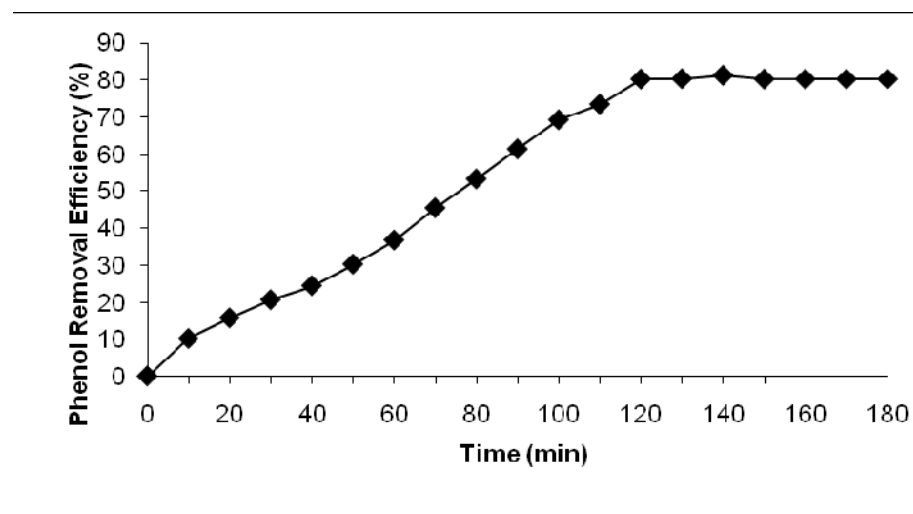


B

**Figure 4** ANN predicted curve of phenol removal rates for different concentrations of (a) MnO<sub>2</sub> and (b) PAA for different time intervals (120 and 180 min).

The catalyst concentration was determined to be the most essential parameter. The removal efficiency increased with an increase in the catalyst load until the optimal value of 70 % was reached. After that, phenol degradation remained nearly the same, regardless the catalyst load. This may be attributed to that the increase in phenol oxidation rate occurred with an increase in the catalyst concentration, because the catalyst activated peracetic acid to form free radicals (Mijangos, Varona et al. 2006). Thus, the maximum removal of phenol was about 70 % for 0.7–3 g L<sup>-1</sup> catalyst load and 100 ppm of PAA, whereas the lowest removal efficiency of 5–6 % was observed for the lowest (0.1 g L<sup>-1</sup>) catalyst concentration and 100 ppm of PAA (Figure 5a). The following analysis of PAA concentration effect revealed that PAA was more effective oxidant at average (e.g. 50 ppm) concentrations (Figure 5b). It is well documented that for so-called Fenton-like processes that involve the homolysis of the oxidizing agent in the presence of the catalyst, the excess of the oxidizing agent acts as a radical scavenger (Mijangos, Varona et al. 2006). The optimal ratio between the catalyst and the oxidizing agent, at which the production of radicals and radical scavenging was well balanced for 0.7 g L<sup>-1</sup> of MnO<sub>2</sub> and 50 ppm of PAA and led to the highest removal efficiency of the target compound (80 %) in 120 min (Figure 5c). It was also determined that the catalyst with the surface area ( $S_{\text{BET}}$ ) of 3.4 m<sup>2</sup> g<sup>-1</sup> exhibited the catalytic activity of 0.042 mM m<sup>-2</sup>s<sup>-1</sup> per surface area.





C

**Figure 5** Plots of main effects on phenol removal efficiency: a) reagent concentrations, b) reaction time.

The efficacy of the proposed experimental modeling with ANN is demonstrated in Figure 6. Figure 6 compares the results obtained from the phenol degradation tests under optimized process parameters with those acquired from neural computation after 120 min. of the treatment in the presence of PAA. The computed results were selected at the intermediate points that were not considered in the experiments and were found to be very close to the interpolation curves. A good agreement between data was obtained with a standard deviation less than 3%.

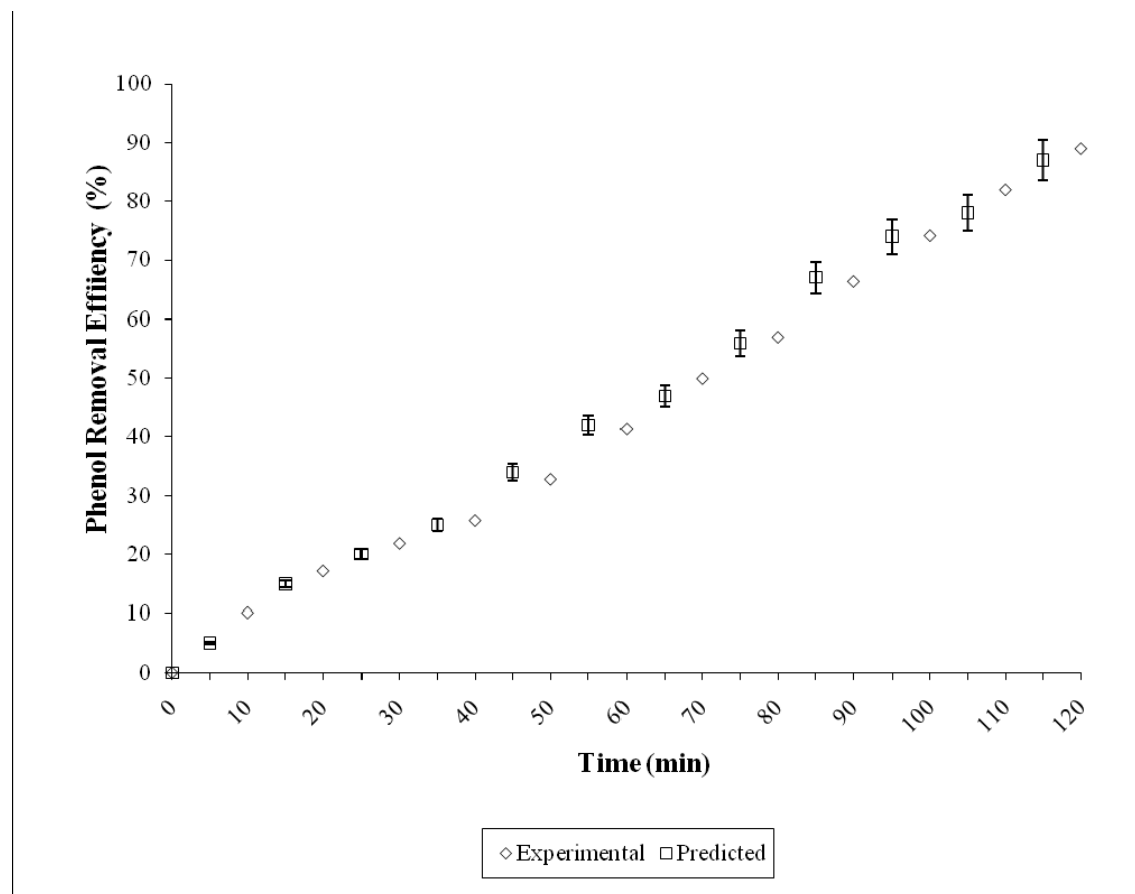


**Figure 6** Comparison between the experimental and simulated results for the removal efficiency of phenol with optimized parameters ( $C[\text{MnO}_2]=0.7 \text{ g L}^{-1}$ ,  $C[\text{PAA}]=50 \text{ ppm}$ , time 120 min.)

## ACKNOWLEDGMENTS

This research was supported by the European Community activity Large-Scale Facility Wageningen NMR Center (FP6–2004–026164 (2006–2009). Maa- ja vesi tekniikaan tuki (MVT) foundation and Academy of Finland (decision number 212649) are acknowledged for their financial support of the research. Dr. Pieter de Waard is thanked for  $^{31}\text{P}$  NMR measurements. The *ab initio* calculations were performed with the Gaussian 03 package in the Interdisciplinary Centre for Mathematical and Computational Modelling (Warsaw, Poland) under the computational Grant G14-6.

## SUPPORTING INFORMATION

### ANN computation.

The ANN feed-forward network was built to analyze the effects of catalyst and PAA concentrations and reaction time to the removal efficiency of phenol. Such a network encodes the relationships between I/O variables through a large set of neurons, which act as mathematical decision centers. All the variables were connected by weights as assigned numbers translating the strength of neuron connections. Weights were assigned to these connections between the neurons of the neighboring layers. In order to predict phenol removal efficiency with the least possible error, these values must be optimized. Therefore, the back-propagation perceptron multilayer has been used to model system dependencies. A more detailed ANNs description can be found elsewhere (Másson and Wang 1990; Nazarov, Apanasovich et al. 2004). Input variables were looked as number of fluxes, which fed the network structure and reached the output pattern. The ANN optimization process was based on a training procedure to eliminate the error between the ANN and experimental responses for a given set of input variables. Such optimization considered neuron number and weight updates. Network training was a process by which the connection weight and bias on the ANN were adapted through a continuous process of simulation by the environment in which the network was embedded (Kasiri, Aleboyeh et al. 2008). The number of experiments to feed the ANN structure was 325. The ANN processing stages were divided into three steps: training, validation and test. The validation and test sets were randomly selected from the experimental data to assess, validate and model power of the nets. The ANN performance was stabilized after the inclusion of 10 nodes in the hidden layer. The network was then tested and validated by comparing its predicted output values with the experimental ones using an independent set of data. The training data set can be found in Tables S2 and S3. Thus, the network input contained three neurons representing catalyst concentration, PAA concentration and the reaction time, respectively. The output pattern comprised one neuron representing the removal efficiency of phenol. Experimental sets were organized in training and test samples. Optimization parameters and ANN characterization data are summarized in Table S2. The ANN used was designed by STATISTICA7 software (StatSoft, USA). The statistical analyses were carried out by Statgraphics Plus (Version 5.1).

**Table S1.** ANN optimization parameters



Parameter	Value	Comments		
		Variable type	Minimum	Maximum
Input variables	3	PAA concentration (ppm)	0	200
		MnO <sub>2</sub> concentration (gL <sup>-1</sup> )	0	3
		Time (min)	0	240
Output variables	1	Phenol removal efficiency (%)	0	100
Architecture	Perception model	See (Másson and Wang 1990) for definition		
	Back propagation			
Training algorithm	propagation	See (Másson and Wang 1990) for definition		
Database	325 samples	Category	Sample number	
		Train	105	
		Test	105	
Optimization cycle number	2000	One cycle corresponds to training and testing of the whole database passage		
Number of hidden layers	3	Suitable for non linear correlations.		
Number of neurons in each layer	Varied	This number is calculated from the optimization procedure		

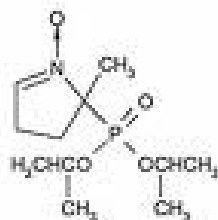
**Table S2.** Training set for ANN: the effect of MnO<sub>2</sub> concentration and the reaction time on the removal efficiency

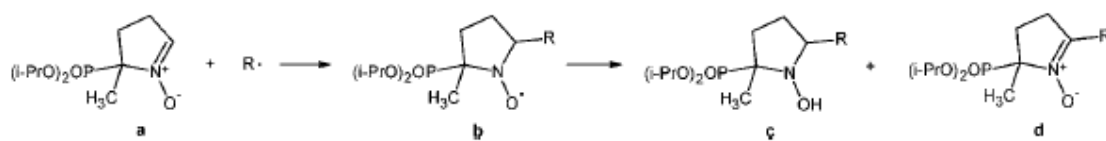
Time (min)/MnO <sub>2</sub> concentration (g L <sup>-1</sup> )	RR,%								
	0	0,1	0,5	0,7	1,0	1,5	2,0	2,5	3,0
0	0	0	0	0	0	0	0	0	0
10	0	0,59	4,3	10,12	13,7	14,1	13,9	14,2	13,8
20	0	1,47	6,1	14,5	21,54	21,2	22,2	20,2	21,8
30	0	2,12	8,2	17,34	25,45	29,3	30,3	31,3	30,3
40	0	2,43	9,97	24,4	30,24	37,5	38,5	37,9	38,6
50	0	2,89	12,1	30,2	35,4	43,8	43,4	44,8	44,6
60	0	3,1	14,5	36,7	40,23	51,23	52,23	51,9	53
70	0	3,42	16,3	45,4	45,1	59,12	59,87	59,42	60,12
80	0	3,78	18,7	53,2	50,24	63,12	64,46	65,9	65
90	0	4,1	20,43	61,3	56,1	65,5	67,32	70	69,5

100	0	4,4	23,12	65,2	60,32	69,12	70,12	69,12	70,12
110	0	4,8	25,45	67,2	68,2	71,45	71,3	72	71,45
120	0	5,11	27,13	74	69,1	71,54	71,34	73,23	73,56
130	0	5,446	27,23	74,2	69,3	71,63	71,38	73,46	73,67
140	0	5,34	27,24	74,4	69,4	71,72	71,42	73,69	73,78
150	0	5,36	27,45	74,3	69,3	71,71	71,46	73,92	73,89
160	0	5,25	27,43	74,4	69,4	71,9	71,5	73,95	73,14
170	0	5,34	27,45	75	69,7	71,99	71,54	73,38	74
180	0	5,4	27,42	75,3	70,4	71,98	69,45	72,13	74,12

**Table S3.** Training set for ANN: the effect of PAA concentration on the removal efficiency

Time (min)/PAA concentration (ppm)	RR,%							
	0	5	10	50	70	100	150	200
0	0	0	0	0	0	0	0	0
10	0	3,7	3,4	13,1	9,3	8,1	6,3	4,5
20	0	6,1	5,4	21,5	18,2	17,2	15,2	12,3
30	0	10,6	9,1	26,4	23,5	22,5	19,2	19,8
40	0	13,3	11,2	31,78	29,7	29,3	25,6	25,4
50	0	16,4	13,5	37,3	35,1	35,3	33,2	27,5
60	0	20,7	15,4	45,1	41,2	40,2	37,6	34,21
70	0	24,1	18,6	51,7	47,9	46,9	43,2	38,4
80	0	28,5	21,3	57,45	54,93	53,93	45,6	43,4
90	0	31,4	25,3	63,23	59,91	58,91	49,98	48,67
100	0	35,2	28,6	69,45	63,12	62,12	55,47	53,98
110	0	38,1	34,5	75,21	68,34	67,34	59,6	56,4
120	0	41	39	78	70	69	63	57

**Figure S1.** Chemical structure of DIPPMPO (diisopropoxy-phosphoryl-5-methyl-1-pyrroline-N-oxide)



**Scheme S1.** The general trapping chemistry of the DIPPMPO spin trap system

The radical ( $R^\bullet$ ) reacts with the nitron spin trap DIPPMPO (a) to form stable paramagnetic adduct (b), which is Electron Paramagnetic Resonance (EPR) detectable. The paramagnetic species (b) decays with time and undergoes unimolecular and/or bimolecular decomposition producing the corresponding diamagnetic species, the hydroxylamine (c) and the nitron (d) via a disproportionation reaction. The stable diamagnetic products (c+d), derived from the radical adducts were Nuclear Magnetic Resonance (NMR) detectable (in the present case  $^{31}\text{P}$  NMR).

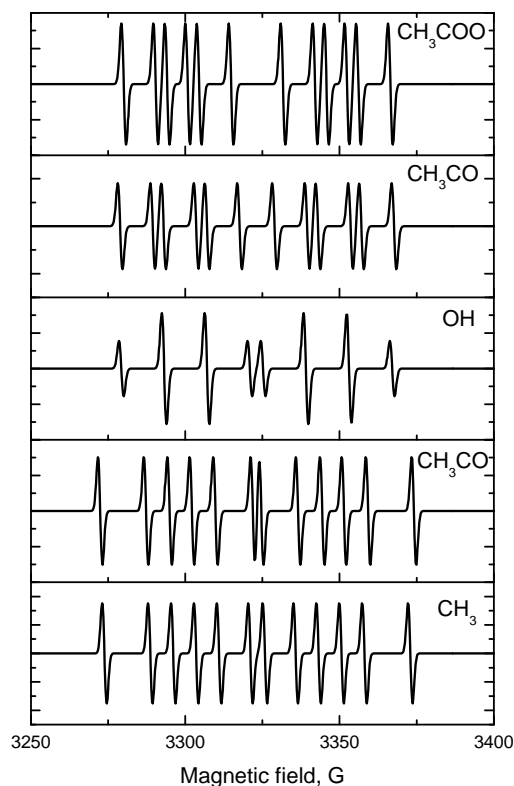


**Figure S2.** Simulation details

The simulations of fast motion ESR spectra were performed with routines implemented in EasySpin toolbox (Stoll, 2006) for Matlab. The splitting pattern for single DIPPMPO radical

adduct originated from one nitrogen, one proton and one phosphor. The fitting of multicomponent experimental spectra DIPPMPO radical adducts by the simulations were performed by simplex method developed by Nelder and Mead (Nelder, 1965). This optimization routine was chosen due to its fast convergence; however it requires a good starting guess, especially in the case of large set of fitted parameters (many component spectra). The hyperfine data from (Charlier and Tordo, 2002) provided a good starting guess for fitting. To decrease the number of fitted parameters, the line positions (splitting pattern) was adjusted first. As the next step, all hyperfine values were fixed and only linewidth parameters and ratio of the components were fitted. Parameters obtained from the best fit of the experimental spectra were: the isotropic hyperfine coupling constants ( $a_N$ ,  $a_H$ ,  $a_P$ ), g-tensor (with respect to 2.00569 for DIPPMPO OH radical adduct (Culcasi,2006)) and ratio of the component.

**Table S4.** Optimized bond length (Å) and angles (deg)

Species	Parameters	Level of theory B3LYP/6-31g(d)
CH <sub>3</sub> C(O)OOH	CC	1.504
	H'C	1.091
	HC	1.094
	CO	1.215
	CO'	1.355
	O'O''	1.442
	O''H''	0.99
	H'CC	111.7
	HCC	108.7
	CCO	127.0
	CCO'	110.9
	CO'O''	111.0
	O'O''H''	99.8
CH <sub>3</sub> C(O)OO•	CC	1.501
	H'C	1.090
	HC	1.095
	CO	1.189
	CO'	1.446

---

CH <sub>3</sub> C(O)O•	O'O''	1.328
	H'CC	109.2
	HCC	110.0
	CCO	129.9
	CCO'	107.6
	CO'O''	113.0
	CC	1.496
	H'C	1.093
	HC	1.096
	CO	1.261
CH <sub>3</sub> CO•	H'CC	110.1
	HCC	109.1
	CCO	124.1
	CC	1.517
	H'C	1.096
	HC	1.095
	CO	1.189
	CCO	1.276
	H'CC	111.5
	HCC	108.7
	H'CCO	0.07

---



## REFERENCES

- Argyropoulos, D. S., H. Li, et al. (2006). "Quantitative  $^{31}\text{P}$  NMR detection of oxygen-centered and carbon-centered radical species." Bioorg. Med. Chem. **14**(12): 4017-4028.
- Bach, R. D., P. Y. Ayala, et al. (1996). "A reassessment of the bond dissociation energies of peroxides. An ab Initio study." J. Am. Chem. Soc. **118**(50): 12758-12765.
- Bacic, G., I. Spasojevic, et al. (2008). "Spin-trapping of oxygen free radicals in chemical and biological systems: New traps, radicals and possibilities." Spectrochimica Acta Part A-Mol. Biomol. Spectr. **69**(5): 1354-1366.
- Blanksby, S. J. and G. B. Ellison (2003). "Bond dissociation energies of organic molecules." Acc.Chem.Res **36**: 255-263.
- Ciotti, C., R. Baciocchi, et al. (2008). "Peroxy-acid as an innovative oxidant for the remediation contaminated sediments." 10th International UFZ/TNO Conference on Soil-Water Systems (CONSOIL).
- Clément, J.-L., B. C. Gilbert, et al. (1998). "Use of a phosphorylated spin trap to discriminate between the hydroxyl radical and other oxidising species." J. Chem. Soc., Perkin Trans. 2: 1715-1717.
- Curtiss, L. A., K. Raghavacharin, et al. (1997). "Assessment of Gaussian-2 and density functional theories for the computation of enthalpies of formation." J. Chem. Phys. **106**: 1063-1079.
- El-Agamey, A. and D. J. McGarvey (2003). "Evidence for a lack of reactivity of carotenoid addition radicals towards oxygen: a laser flash photolysis study of the reactions of carotenoids with acylperoxyl radicals in polar and non-polar solvents." J. Am. Chem. Soc. **125**(11): 3330-3340.
- Gonzalez Cuervo, L., Y. N. Kozlov, et al. (2004). "Oxidation of saturated hydrocarbons with peroxyacetic acid catalyzed by vanadium complexes." J.Mol. Catal. A- Chem. **218**(2): 171-177.
- Heywood, D., B. Phillips, et al. (1961). "Communications. Free radical hydroxylations with peracetic acid." J. Org. Chem. **26**(1): 281-281.
- Kasiri, M. B., H. Aleboyeh, et al. (2008). "Modeling and Optimization of Heterogeneous Photo-Fenton Process with Response Surface Methodology and Artificial Neural Networks." Enviro. Sci. Technol. **42**(21): 7970-7975.

- Keller, B. K., M. D. Wojcik, et al. (2008). "A directly-dissociative stepwise reaction mechanism for gas-phase peroxyacetic acid." J. Photochem. Photobiol. A- Chem. **195**(1): 10-22.
- Khramtsov, V. V., L. J. Berliner, et al. (2001). New approaches in spin labeling and spin trapping part two: NMR detects free radicals. Supramolecular Structure and Function **7**. G. Pifat, Kluwer/Academic/Plenum Publishers: 107-118.
- Kitis, M. (2004). "Disinfection of wastewater with peracetic acid: a review." Environ. Int. **30**(1): 47-55.
- Koivunen, J. and H. Heinonen-Tanski (2005). "Peracetic acid (PAA) disinfection of primary, secondary and tertiary treated municipal wastewaters." Water Res. **39**(18): 4445-4453.
- Lubello, C., R. Gori, et al. (2004). "Municipal-treated wastewater reuse for plant nurseries irrigation." Water Res. **38**(12): 2939-2947.
- Másson, E. and Y.-J. Wang (1990). "Introduction to computation and learning in artificial neural networks." European J. Oper. Res. **47**(1): 1-28.
- Mijangos, F., F. Varona, et al. (2006). "Changes in solution color during phenol oxidation by Fenton reagent." Enviro. Sci. Technol. **40**(17): 5538-5543.
- Mojovic, M., I. Spasojevic, et al. (2005). "Detection of hydrogen atom adduct of spin trap DEPMPO. The relevance for studies of biological systems." J. Chem. Inf. Mod. **45**(6): 1716-1718.
- Morales-Roque, J., M. Carrillo-Cárdenas, et al. (2009). "Theoretical and experimental interpretations of phenol oxidation by the hydroxyl radical." J. Mol. Struct.-THEOCHEM **910**: 74-79.
- N'Guessan, A. L., T. Carignan, et al. (2004). "Optimization of the peroxy acid treatment of  $\alpha$ -methylnaphthalene and benzo[a]pyrene in sandy and silty-clay sediments." Enviro. Sci. Technol. **38**(5): 1554-1560.
- Nazarov, P. V., V. V. Apanasovich, et al. (2004). "Artificial neural network modification of simulation-based fitting: application to a protein-lipid system." J. Chem. Inf. Comput. Sci. **4**: 568-574.
- Ochterski, J. W. (2000). "Thermochemistry in Gaussian." from [www.gaussian.com](http://www.gaussian.com).
- Rey, A., M. Faraldos, et al. (2009). "Catalytic wet peroxide oxidation of phenol over Fe/AC catalysts: Influence of iron precursor and activated carbon surface." Appl. Catal. B-Environ. **86**(1-2): 69-77.



- Rokhina, E. V., M. Lahtinen, et al. (2009). "The influence of ultrasound on the RuI3-catalyzed oxidation of phenol: Catalyst study and experimental design." Appl. Catal. B-Environ. **87**(3-4): 162-170.
- Shi, H.-C. and Y. Li (2007). "Formation of nitroxide radicals from secondary amines and peracids: A peroxy radical oxidation pathway derived from electron spin resonance detection and density functional theory calculation." J.Mol. Catal. A- Chem. **271**(1-2): 32-41.
- Sicilia, E., F. P. M. Maio, et al. (1993). "Heats of formation of oxygen-containing radicals from local spin density computations " J. Phys. Chem. **97**: 528-530
- Stoll, S. and A. Schweiger (2006). "EasySpin, a comprehensive software package for spectral simulation and analysis in EPR." J. Magn. Res. **178**: 42-55.
- Villamena, F. A., E. J. Locigno, et al. (2006). "Theoretical and experimental studies of the spin trapping of inorganic radicals by 5,5-dimethyl-1-pyrroline N-oxide (DMPO). 1. Carbon dioxide radical anion." J. Phys. Chem. A **110**(49): 13253-13258.



## **Chapter 6**

### **A NEURAL NETWORK APPROACH TO THE RAPID ANALYSIS OF THE KINETICS OF FDMPO FREE RADICAL SPIN ADDUCTS FROM ISOTROPIC ESR SPECTRA**

Katerina Makarova, Igor Borovykh, Elena A. Golovina, Wawer Iwona, Henk Van As.

To be submitted

#### **ABSTRACT**

In this work, an artificial neural network (ANN) is explored for its ability to extract the fractions of radical adducts from narrow line ESR spectra. The ANN trains fast and performs well on signals with signal/noise of 200. The obtained fraction coefficients are in agreement with the ones obtained by an iterative fitting approach. The time needed for data processing by the ANN was in the order of seconds and it did not increase with the number of analyzed spectra.

This approach was shown to be rapid and highly efficient for the analysis of two component ESR spectra from 4-hydroxy-5,5-dimethyl-2-trifluoromethylpyrroline-1-oxide (FDMPO) radical adducts formed in the Fenton reaction in the presence of DMSO or methanol. The anti-oxidant properties of the DMSO or methanol extracts from long-lived pine pollen and short-lived narcissus pollen are shown by their influence on the kinetics of FDMPO adducts formation in the Fenton reaction. These findings suggest neural network offers a promising approach for the study of antioxidant activity of plant extracts.

## 6.1 Introduction

The spin-trapping technique is used for the *in vitro* and *in vivo* study of the kinetics and mechanisms of reactions in which short-lived free radicals are formed. Spin trapping utilizes the reaction of unstable free radicals with nitron or nitroso spin traps, resulting in the production of spin adducts that can be detected by Electron Spin Resonance (ESR) spectroscopy (Janzen 1971; Janzen, Stronks et al. 1985). The resulting spin adducts are nitroxide radicals which have an ESR spectra with a hyperfine structure characteristic for the type of trapped free radical. This can be used for identification of that free radical. The time evolution of the ESR spectra is used to study the mechanism of reactions resulting in these free radicals.

The ESR spin trapping technique has some limitations. One of them is the short lifetime of most spin adducts. One of the most commonly used spin traps, 5,5-dimethylpyrroline-N-oxide (DMPO) forms very short-lived spin adducts with  $O_2^*$ ,  $OH^*$  and alkyl radicals. The lifetime of a DMPO-OOH\* adduct is approximately 50 s (Finkelstein, Rosen et al. 1979). Recently, a new class of spin traps has been developed. These are DMPO derivatives (Frejaville, Karoui et al. 1995; Khramtsov, Reznikov et al. 2001) that have improved properties for trapping of free radicals and an extended lifetime from several minutes (5-diethoxyphosphoryl-5-methyl-1-pyrroline-N-oxide (DEPMPO)) to several hours (4-hydroxy-5,5-dimethyl-2-trifluoromethylpyrroline-1-oxide (FDMPO)) (Khramtsov, Reznikov et al. 2001; Chalier and Tordo 2002; Khan, Wilmot et al. 2003; Bacic, Spasojevic et al. 2008).

Another limitation was the ability of some spin traps to form spin adducts with different radicals. DEPMPO and FDMPO can trap different types of free radicals in the system under study, resulting in an ESR spectrum, which is a linear superposition of the spectra of the various radical adducts.

Generally, the splitting patterns of the various radical adducts are not significantly different, when their lifetimes are long (Janzen 1998). Although DEPMPO or FDMPO form relatively stable spin adducts, the identification and analysis of the kinetics of trapped radicals from ESR spectra is difficult. On the contrary, the spectra from different DMPO free radical adducts are well resolved, but study of the kinetic of the radical formation is difficult because of the short lifetime of the spin adducts.

The kinetics of each radical adduct in a mixture can be analyzed either (i) by following the time-evolution of a single peak intensity of the given adduct in a multi-component ESR

spectrum (Staško, Raptá et al. 1993) or (ii) by Simulation Based Fitting (SBF). The method of a single peak analysis is only applicable for non-overlapping spectral components, or partly overlapping components with fully resolved peaks, as in the case of DMPO spin adducts. When both OH radicals and carbon-centered radicals are trapped by FDMPO, none of the peaks are well resolved, and decomposition of the spectrum is needed.

The SBF method is widely used for the decomposition of any multi component ESR spectrum. The idea of SBF is approximation of the experimental spectrum by a simulated one based on the mathematical model. The fitting algorithm minimizes the error (difference) between two spectra by varying parameters for simulation of the artificial spectra. The fast isotropic motion model is successfully used for the simulation of ESR spectra of spin probes (Israelachvili, Sjösten et al. 1975; Smirnov, Smirnova et al. 1995) and spin traps (Busi, Travagli et al. 2010; Rokhina, Makarova et al. 2010). The spectral parameters (hyperfine splitting constants and correlation time) together with the fraction of each component are determined by SBF. Subsequently, trapped radicals are identified based on extracted hyperfine splitting constant values of radical adducts. Thus, the time evolution of each component in multi component ESR spectra could be followed based on accurate fitting and extraction of the fraction at every time point.

Simulation of one ESR spectra is relatively fast and takes a couple of minutes on a pc and routines and programs for simulations are available (Kirste 1992; Budil, Lee et al. 1996; Stoll and Schweiger 2006). When analyzing a set of spectra (e.g. from kinetic measurements), each spectrum is fitted iteratively, and the time needed for the analysis of all the spectra is linearly dependent on the number of spectra. The use of new spin traps with prolonged lifetimes of spin adducts results in an extension of the time over which the reaction can be studied by the spin trapping approach, and thus, increases the number of spectra for the analysis. The development of a method, which uses a non-iterative approach for analyzing spin adduct spectra, would be quite helpful because it will perform faster than an iterative approach. Such a method could be applied for real time analysis of ESR spectra during kinetics measurements, directly providing information about both integrated intensities of each spectral component and, therefore, concentrations of paramagnetic species. For that purpose the use of Artificial Neural Networks (ANNs) were explored (Wasserman 1989; Bishop 1995; Haykin 1998).

ANNs have emerged as a remarkable tool for signal processing. ANNs have been developed as generalizations of mathematical models of biological nervous systems. The basic processing elements of neural networks are called artificial neurons or nodes. In a

simplified mathematical model of the neuron, the effect of the synapses is represented by connection weights that modulate the effect of the associated input data. The nonlinear characteristic exhibited by neurons is represented by transfer function.

In this study two types of ANN, the Radial Basis Function (RBF) network and Multi Layer Perceptron (MLP) network, were explored for their ability to extract the fraction of radical adducts from narrow line ESR spectra (fast isotropic motion model). Our results show that the RBF network trains very rapidly and performs well both with artificial and experimental data, whereas MLP trains slowly and performs well only with data from testing set, so only RBF network was used for analysis of experimental spectra. Once trained, the RBF network requires nearly the same time to extract the fraction coefficient at any number of spectra. The accuracy of this ANN approach and the time needed for data processing are compared with those of an iterative fitting approach. RBF is applied to the decomposition of multi-component ESR spectra from FDMPO radical adducts formed in the Fenton reaction in the presence of dimethylsulfoxide (DMSO) or methanol (MeOH). The anti-oxidant properties of the DMSO or MeOH extracts from long-lived pine pollen and short-lived narcissus pollen are shown by their influence on the kinetics of FDMPO adducts formation in the Fenton reaction. This experiment reveals the possible application of this method to study antioxidant activity of plant extracts.

## **6.2 Material and methods**

### *6.2.1 Sample preparation*

All chemicals, except the spin trap FDMPO, were purchased from Sigma Aldrich and Merck & Co., Inc. FDMPO was purchased from Alexis Biochemicals (USA). The chemicals were of laboratory reagent grade and used without further purification. Distilled water was used in all the experiments.

Fenton's reagents (5  $\mu$ l of 0.5 mM  $\text{FeSO}_4$  and 5  $\mu$ l 5mM  $\text{H}_2\text{O}_2$ ) were used to generate hydroxyl radicals in a primary reaction. 5  $\mu$ l of 10 mM FDMPO was added to trap free radicals. 5  $\mu$ l of plant extracts in dimethylsulfoxide (DMSO) or methanol were added to study their antioxidant activity. In the control 5  $\mu$ l of DMSO or methanol were added instead of plant extract in the respective solvents.

### 6.2.2 Plant material

Pine and narcissus pollen were collected locally near Wageningen, The Netherlands, in May-June 2009, sieved, air-dried on the laboratory bench and subsequently stored at -20°C until used. 1 mg of air-dried pollen was soaked in 5 ml ethanol for 1 day. After extraction pollen was separated from the solvent by filtration through filter paper. The filtrate was collected and the solvent was removed by evaporation. The dry extract was dissolved in 5 ml of DMSO or methanol, and the solution was filtered.

### 6.2.3 ESR

ESR measurements were performed on a Bruker E500 Eleksys SuperX. The typical settings for kinetic measurements were 5 mW microwave power, modulation amplitude of 1 G, 20 s time constant, single scan measurements. The number of recorded spectra is specified for each experiment, the time delay between measurements was 300 s.

In order to obtain high accuracy parameters from spectra fitting, reference ESR spectra for simulation were recorded separately from the kinetic measurements. These reference spectra were recorded with 0.2 G modulation amplitude, 5 mW microwave power, 20 s time constant and 20 scans were accumulated for a better signal to noise ratio. All ESR experiments were performed at room temperature.

### 6.2.4 Simulation based fitting

Simulation of FDMPO spin adduct spectra was performed using the mathematical model for fast isotropic motion (Israelachvili, Sjösten et al. 1975) of nitroxide spin probes and the Nelder and Mead optimization routine (Nelder and Mead 1965). The spectral line shape was described as a convolution of a Lorentzian and Gaussian function in a 1:1 ratio, i.e. the same value of broadening was used for simulation of the Lorentzian and Gaussian lineshapes (Israelachvili, Sjösten et al. 1975). Hyperfine splitting values published by Khramtsov (Khramtsov, Reznikov et al. 2001) were used as a starting point for spectra simulations. Fraction coefficients were determined as the ratio between the double integral of a single component and the double integral of the total ESR spectra. Thus, the sum of all fraction coefficients extracted from a multi-component spectrum is equal to 1. Hyperfine splitting constants together with  $g_{iso}$  and the rotational correlation time were obtained from simulation of the reference ESR spectra (see Table 1). For the analysis of the time evolution of the ESR spectra the number of tuning parameters was reduced and only the fraction coefficients were fitted.

### 6.2.5 Artificial Neural Network

Using the Matlab Neural Network Toolbox both types of ANN were designed with “newrb” (RBF) and “newp” (MLP) routines.

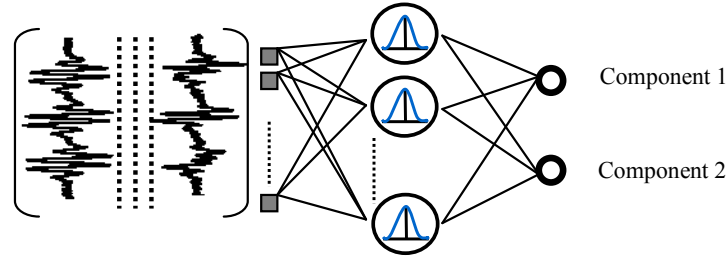


**Figure 1.** RBF Neural network architecture. The spectrum matrix consists of 20 columns of ESR spectra (simulated or experimental), each represented by  $R = 512$  points. These spectra are presented to the network and the weights of  $S$  hidden layer nodes and the output nodes are adjusted to correctly predict the value of fraction coefficient  $f$ .

The general architecture for the RBF network is shown in Fig. 1. According to theory the RBF network has three layers: an input layer, a hidden layer with a non-linear RBF activation function and a linear output layer. The input layer  $\mathbf{I}$  is a vector that consists of  $R = 512$  points of an ESR spectrum. In this type of ANN the input layer is sometimes not considered as a layer since it makes no processing, so in Matlab description of “newrb” function only two-layers (the hidden layer with RBF activation functions and output layer with linear transfer function) are described. Then, at each node of the  $S$  nodes in the hidden layer, the Euclidian distance is used to compare the weight vector  $\mathbf{W}_i$  to  $\mathbf{I}$ , and the value then passes through a Gaussian function characterized by a spread constant  $p$ . The output of each node in the hidden layer is thereby given as

$$O_i = f(\|\mathbf{W}_i - \mathbf{I}\| \times \sqrt{\log(2) / p}) \quad (1)$$

where  $i$  varies from 1 to  $S$ . The output layer implements a weighted sum of the hidden layer outputs. The collection of  $S$  scalars resulting from the  $S$  nodes in the hidden layer is then passed as a vector to the two nodes of the output layer yielding values for the fraction coefficients. The spread constant is adjusted empirically. The number of nodes in the hidden layer,  $S$ , is determined dynamically during the training process (Haykin 1998).

Another type of ANN, an Multi Layer Perceptron (MLP) is composed of  $M$  layers, i.e. input, output and one or more hidden layers (Rosenblatt 1958). Each layer  $m$  has  $N_m$  neurons. Each neuron  $i$  in one layer connects with a certain weight  $W^m_i$  to every neuron in the following layer. The output  $O_i$  of a neuron  $i$  is an activation function  $F_m$  of the weighted sum



of the outputs coming from the neurons in the previous layer  $N_{m+1}$  (output layer has  $m=1$ , the input layer has  $m=M$ ).

$$O_i = F_m \left( \sum_{i=0}^{N_{m+1}} I_i W_i^m \right) \quad (2)$$

The number of hidden layers, number of neurons in each layer and type of activation function are adjusted empirically, whereas the weights  $W_i^m$  are adjusted during the training procedure. Usually, a supervised training method, called back propagation, is used to train the MLP (Rumelhart, Hinton et al. 1986).

During the training procedure the performance of ANN is determined based on (i) Minimum Sum Squared Error (SSE) (William 1986) and (ii) the smallest maximum percent error for each fraction in the set. The percent error for each value was calculated using

$$E_i = \frac{O_i - \bar{O}_i}{O_i} \quad (3)$$

where  $O_i$  are the expected output values,  $\bar{O}_i$  - the modeled output values. The SSE was calculated as the sum of the percent errors. The training of the ANN stops when the SSE reaches a pre-defined value. Then the ANN was tested for its ability to generalize the new data whose underlying statistics is similar to that of the training set. This step allows to avoid the situation that ANN is over-fitting, i.e. ANN performs well only on training set, however it fails on new data.

### 6.2.6 Training set construction

ESR spectra were simulated as described above. Values chosen for parameters depended on the system under study (Table 1). A matrix of 20 two-component ESR spectra was generated with fraction coefficients ranging from 0 to 1 for each experimental system, i.e. the Fenton reaction with methanol and the Fenton reaction with DMSO. Two matrices of 20 spectra (Figure 2) were constructed for training. The two matrices of spectra for the testing set were simulated following the same procedure. However, other values for the fraction coefficients, not presented in the training set, were used, i.e. the fraction coefficients for the training set was 0.0, 0.1, 0.15, 0.2 and etc., whereas for testing set we used fraction coefficients 0.02, 0.08, 0.12 etc. To improve the performance and robustness of the neural network on experimental data, a 5% random noise was added to the simulated spectra. Then,

spectra in the training, testing and experimental sets were normalized by setting the double integral of the spectrum equal to one before introduced to the network.

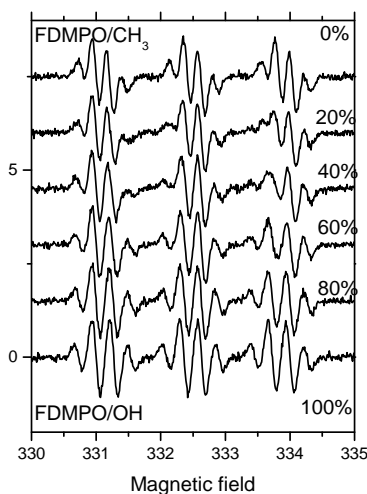
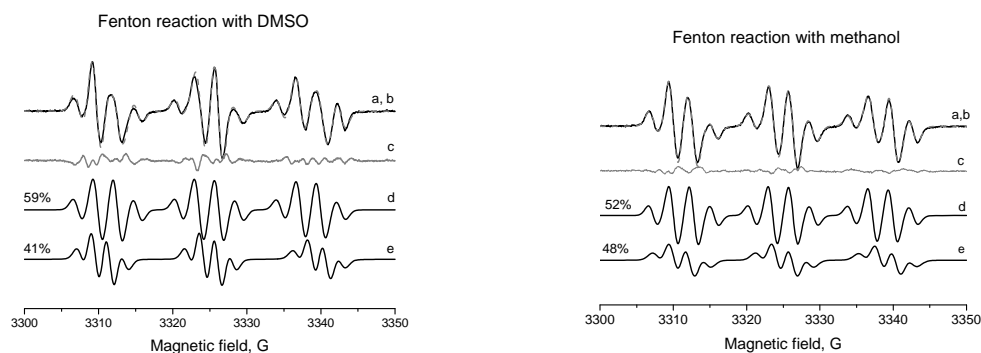


**Figure 2.** Six spectra out of a training set of 20 with different fractions of FDMPO/CH<sub>3</sub>\* and FDMPO/OH\*, where 0% corresponds to FDMPO/CH<sub>3</sub>, 100% to FDMPO/OH\*. The parameters used for simulations were determined from experimental reference spectra of FDMPO/OH\* and FDMPO/CH<sub>3</sub>\* adducts and are summarized in Table 1.

## 6.3 Results and discussion

### 6.3.1 Spectra analysis using simulations

Fitting of a typical ESR spectrum of FDMPO radical adducts obtained in the Fenton reaction with DMSO (Fig. 3 A-a, b) shows the presence of two spectral components with different splitting patterns. One component with  $A_F = 2.68$  G and  $A_N = 13.7$  G corresponds to the FDMPO/OH\* adduct (Fig 3A-d). A second component with  $A_F = 1.93$  G and  $A_N = 14.6$  G corresponds to the FDMPO/CH<sub>3</sub>\* adduct (Fig. 3A-e). The same two FDMPO radical adducts were detected in the Fenton reaction in the presence of pine pollen extract dissolved in DMSO (data not shown).



A

B

**Figure 3.** Experimental (a) and simulated spectra (b) of FDMPO adducts from Fenton reaction with DMSO (A) or methanol (B). (A) The two components are assigned to FDMPO/OH\* (d) and FDMPO/CH<sub>3</sub>\* (e) spin adducts. (B) The two components are assigned to FDMPO/OH\* (d) and FDMPO/CH<sub>2</sub>OH\* (e) spin adducts. (c) Represents the difference between the experimental spectrum (a) and the simulated one (b).

The simulation of ESR spectra of the spin adducts obtained in the Fenton reaction with methanol (pure solvent or plant extract in methanol) also shows the presence of two radical adducts - OH\* ( $A_F=2.77$  G,  $A_N=13.6$  G, Fig.3 B-d)) and CH<sub>2</sub>OH\* ( $A_F=2.13$  G,  $A_N=14.08$  G, Fig. 3 B-e)) (Table 1).

**Table 1.** Magnetic parameters of FDMPO adducts from a Fenton reaction with DMSO and with methanol, determined from simulation based fitting of experimental reference ESR spectra.

Source	FDMPO adducts	Parameters		
		$a_N$ (G)	$a_F$ (G)	$\tau$ (s)
Fenton reaction in DMSO	FDMPO/OH	13.7	2.6	$1 \cdot 10^{-11}$
	FDMPO/CH <sub>3</sub>	14.6	1.93	$2 \cdot 10^{-11}$
Fenton reaction in methanol	FDMPO/OH	13.7	2.6?	$1 \cdot 10^{-11}$
	FDMPO/CH <sub>2</sub> OH	14.08	2.13	$5 \cdot 10^{-11}$

Generally, the simulated spectra (Fig 3, b) are in good agreement with the experimental ones (Fig 3, a) and the obtained hyperfine splitting values are in good agreement with previously published ones (Khramtsov, Reznikov et al. 2001). Once magnetic parameters were extracted from reference ESR spectra and the components were identified, there was no need to perform the fitting of all parameters at each point of the time evolution of the ESR spectra. So, for the analysis of the time evolution of the ESR spectra the number of parameters was reduced to the fraction coefficient only.

### 6.3.2 Choice of ANN architecture

Before being applied to the analysis of experimental data both types of ANN, RBF and MLP, need to be trained on a set of inputs and desired outputs. The RBF and MLP neural networks were trained on 20 simulated ESR spectra, six of which are shown in Fig. 2. Subsequently, the MLP and RBF performance was checked on 30 simulated ESR spectra from the testing set. The training of MLP was quite slow (around 20 minutes on a standard pc). Several hidden layers (1 to 10) and different number of nodes (1 to 20) in each of the hidden layers were tested for the error goals 0.01 and 0.001. The maximum percent error for each spectrum and the total SSE for the whole set were calculated by varying the number of hidden layers, number of nodes in hidden layers and epochs of training. It was found that the training process reached the error goal 0.001 after around 6000 epochs for the MLP with 2 hidden layers with 5 and 15 nodes and sigmoid activation function. However, the MLP failed on testing set, what indicates over-fitting of the MLP, when ANN loses the ability to generalize. In case of MLP, over-fitting of the network is mainly caused by a large number of training epochs. However, other configurations of MLP and/or smaller number of training epochs did not result in reaching the error goal 0.001.

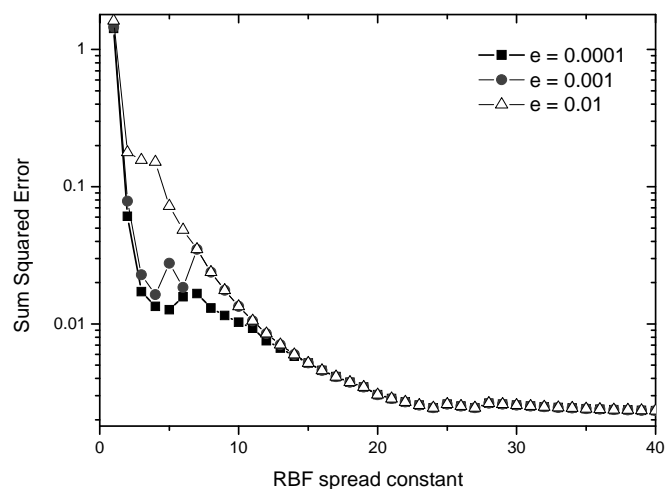


**Figure 4.** Sum square errors as a function of the RBF spread constant for different error goals.

Contrary to MLP, the training for the RBF network was fast (in the order of a minute on a standard pc). Several values of the spread constant were examined (Fig. 4) for error goals 0.01 and 0.001. The maximum percent error for each spectrum and the total SSE for the whole set were calculated by varying the spread constants (Table 2). The smallest SSE and the smallest error percent were obtained when the spread constant was 20. In general spread

constants larger than 8 were already enough for a good performance of our RBF network ( $SSE = 0.175$ ), however a large maximum percent error value (25%) indicates that some fraction coefficients are determined with large error. The RBF with spread constant 20 had the best performance based on SSE and maximum percent values, however, a further increase in spread constant decreased the accuracy of the RBF (Table 2) and resulted in over-fitting. In case of RBF network, the over-fitting of the network is caused by the number of nodes in the hidden layer and a too large spread constant. As explained elsewhere (Hagan, Demuth et al. 1996), a small spread constant results in a steep radial basis curve, forcing a small number of neurons to respond to an input, while a large spread constant results in a smooth radial basis curve, allowing more neurons to respond to an input. Once training was completed to a goal error of 0.001, the testing set was presented to the network and the fraction coefficients  $f$  were compared to the correct values. The correlation between the correct and output values was used to quantify the goodness of fit. Fig 5 shows the network output plotted against the correct  $f$  for spread constant 2, 8, 20 and 30. Clearly, too small values of the spread constant (2 and 8) result in large errors in extracted fraction coefficients in the ranges  $[0 \ 0.1]$  and  $[0.9 \ 1]$  of the fraction coefficients.

**Table 2.** Dependence of RBF network performance on the spread constant.

Spread constant	Maximum Percent error	Sum Square Error	Goal error achieved
2	0.44	0.225	0.00139
8	0.258	0.175	0.00183
20	0.099	0.0318	0.00143
30	0.122	0.0455	0.00079

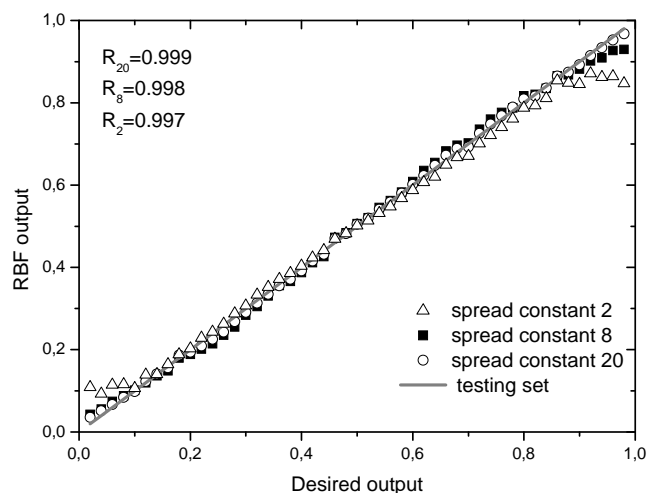
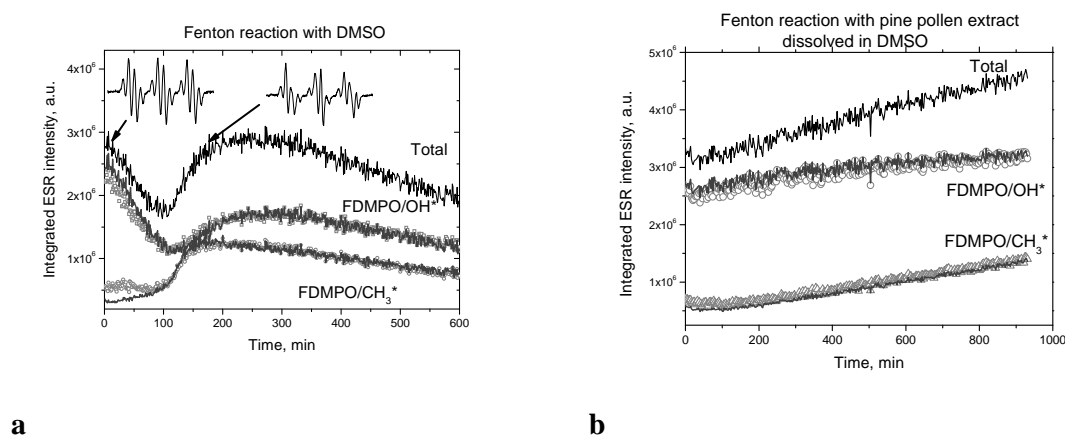


**Figure 5.** Correlation between RBF network output and actual fraction coefficients from the testing set for spread constants of 2, 8 and 20.

The failure of MLP to extract the fractions of components from ESR spectra could be due to the nature of ESR spectra. A typical ESR spectrum of FDMPO spin adducts is sparse, i.e. it has relatively few non-zero values (relatively narrow ESR peaks). In this case RBF has an advantage due to radial basis activation function which computes the output of a neuron based on calculated distance (Eq.1), so the further a neuron is from the point being evaluated, the less influence it has. This property probably is responsible for the robustness of RBF for the analysis of such ESR spectra. In MLP all neurons contribute equally, thus the noise has strong influence on the performance of such ANN. Therefore, for the analysis of experimental spectra only RBF networks were created using spread constant 20 and error goal 0.001. For each experimental system, such as the Fenton reaction in methanol and in DMSO, a new RBF neural network was trained on an input set of spectra simulated with parameters determined from experimental spectra of the corresponding system (Table 1). The outputs of the RBF network were the fraction coefficients of hydroxyl and c-centered radical adducts of FDMPO.

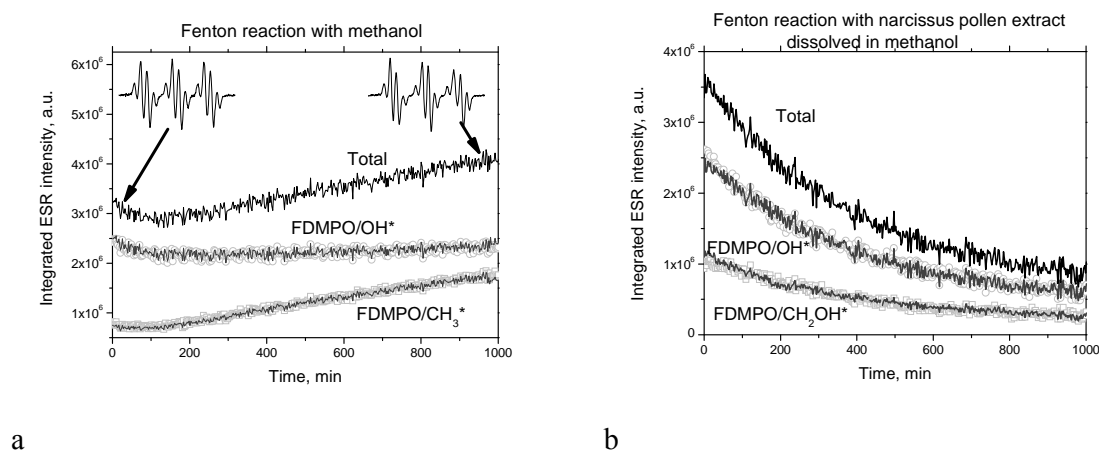
### 6.3.3 Analysis of spectra observed during Fenton reactions

Fig. 6 shows the time evolution of the integrated intensity of the total ESR spectrum and of its spectral components (FDMPO/OH\* and FDMPO/CH<sub>3</sub>\*) obtained in the Fenton reaction with DMSO (Fig. 6a) and with pine pollen extract dissolved in DMSO (Fig. 6b). Peaks of both spectral components in the total spectra overlap heavily (Figure 3a), and the direct quantification of both adducts from ESR spectra is practically impossible



**Figure 6.** Time evolution of the double integrals of the total experimental ESR spectra from FDMPO spin adducts and of the two spectral components FDMPO/CH<sub>3</sub>\* and FDMPO/OH\*, determined by iterative fitting of spectra (lines) and by RBF (symbols). *a* – Fenton reaction with DMSO, *b* – Fenton reaction with pine pollen extract dissolved in DMSO.

To obtain the time evolution of both spectral components, the fractions of components from the spectra were automatically extracted by (i) iterative simulation based fitting and (ii) from the RBF network trained to recognize FDMPO/OH and FDMPO/CH<sub>3</sub> radical adducts. Then, the extracted fraction coefficients were multiplied by the total integrated spectral intensity. The same approach was used for the analysis of spin adduct ESR spectra observed in the Fenton reaction in the presence of methanol (Fig. 7a) and in the presence of narcissus pollen extract dissolved in methanol (Fig. 7b).



**Figure 7.** Time evolution of the double integrals of the total experimental ESR spectra of FDMPO spin adducts and of the two spectral components FDMPO/CH<sub>2</sub>OH\* and FDMPO/OH\*, determined by iterative fitting of spectra (lines) and by RBF (symbols). *a* – Fenton reaction with methanol, *b* – Fenton reaction with narcissus pollen extract dissolved in methanol.

### 6.3.4 Kinetic analysis

The ESR intensity of the given component is proportional to the actual concentration of the corresponding radical adduct. During the first 100 minutes of the Fenton reaction with DMSO (Figure 6a), the spectrum is dominated by the FDMPO/OH\* adduct component (Table 3, reactions 1 and 5). The intensity of the FDMPO/OH\* component decreased in time together with an increase of the FDMPO/CH<sub>3</sub>\* adduct component, indicating the reaction of the OH\* with DMSO to form the CH<sub>3</sub>\* (Table 3, reaction 2), and later to form FDMPO/CH<sub>3</sub>\* adduct (Table 3, reaction 6). However, the rate constant of reaction 6 is two orders of magnitude lower than that of reaction 2, thus the excess amount of CH<sub>3</sub> radicals could react with H<sub>2</sub>O<sub>2</sub> and becomes a second source for OH\* radicals (reaction 4), resulting in an increase of the FDMPO/OH\* adduct component (Figure 6a). The mechanism of this reaction is similar to that described elsewhere (Yamazaki and Piette 1991; Lee, Lin et al. 2002).

**Table 3.** Possible reactions and corresponding rate constants.

Reaction	Reaction rates 10 <sup>8</sup> (M <sup>-1</sup> s <sup>-1</sup> )	Reference
1 Fe(II)+H <sub>2</sub> O <sub>2</sub> ->OH* +OH* +Fe(III)	63.5	(Rigg, Taylor et al. 1954)
2 OH*+DMSO->CH <sub>3</sub> *+CH <sub>3</sub> (S)OH	54 - 72	(Milne, Zika Rod et al. 1989; Lee, Lin et al. 2002)
3 OH*+CH <sub>3</sub> OH->CH <sub>2</sub> OH*+H <sub>2</sub> O	9.7	(Buxton, Greenstock et al. 1988)
4 CH <sub>3</sub> *+H <sub>2</sub> O <sub>2</sub> -> CH <sub>3</sub> OH+OH*	0.35	(Stevens, Clarke et al. 1972)
5 FDMPO +OH*->FDMPO/OH*	22.4	(Khramtsov, Reznikov et al. 2001)
6 FDMPO+CH <sub>3</sub> *->FDMPO/CH <sub>3</sub> *	0.1	(Khramtsov, Reznikov et al. 2001)
7 FDMPO+CH <sub>2</sub> OH*->FDMPO/CH <sub>2</sub> OH*	0.2	(Khramtsov, Reznikov et al. 2001)

The addition of pine pollen extract dissolved in DMSO changed the proposed mechanism of reaction. Only a small number of CH<sub>3</sub> radicals are trapped by FDMPO, the FDMPO/OH\* component dominates in the total spectrum, and the spectral intensity increases with time (Figure 6b). In this system the compounds extracted from pine pollen by methanol,



compete with DMSO for primary OH\* radicals preventing the formation of carbon-centered radicals (Table 3, reaction 2). Therefore, the extract from pine pollen clearly shows anti-oxidant activity in relation to hydroxyl radicals.

The time evolution of the ESR radical adducts spectra during the Fenton reaction with methanol (Fig. 7a) revealed a constant steady state concentration of FDMPO/OH\* component, and the increase of total spectral intensity is only due to the formation of FDMPO/CH<sub>2</sub>OH\* adducts (Table 3, reactions 3 and 7). Adding the extract from narcissus pollen dissolved in methanol results in a decrease of the total spectrum intensity and in the intensities of both spectral components (Fig. 7b). Obviously, the compounds extracted from narcissus pollen scavenge both hydroxyl and CH<sub>2</sub>OH\*, demonstrating the anti-oxidant activity in relation to these two free radicals.

### 6.3.5 Comparison of the efficiency of iterative analysis and artificial neural networks

The accuracy and time performance of SBF and ANN approaches are summarized in Tables 4 and 5. Determination of the fraction coefficients was successful using either iterative SBF method with the fraction coefficient as the only variable parameter or the RBF artificial neural network. Indeed, the determined fraction coefficients are well correlated (Table 4). However, the time required for the analysis of the set of spectra from one kinetic experiment differs drastically for the two approaches.

**Table 4.** Correlation R between the fraction coefficients extracted by RBF network and by iterative fitting

System	R (correlation)
Fenton reaction with DMSO	0.991998
Fenton reaction with pine pollen extract dissolved in DMSO	0.992585
Fenton reaction with methanol	0.993563
Fenton reaction with narcissus pollen extract dissolved in methanol	0.997104

The application of the SBF approach is straightforward, the time needed for analysis of one spectra is about 156 s, and the productivity of the iterative approach is linearly dependent on the number of spectra to be analyzed (Table 5), resulting in 1560 min for 600 spectra and 2600 min for 1000 spectra. The advantages of SBF for analysis of the spectra are that it doesn't require any preprocessing of data or code modification, and more parameters, if

necessary, could be extracted from each spectrum. In addition to fraction coefficients and integrated intensity, the hyperfine splitting constants, g-tensor and correlation time can be also determined. However, in the presented applications these additional parameters are constant in time, so they are already defined from the simulation of one spectrum. Contrary to the SBF iterative analysis, the productivity of an ANN method for analysis of one spectrum is 0.12 s, and when a set of 600 spectra is analyzed it increases to only 0.25 s. A further increase of the number of spectra doesn't influence significantly the processing time for the RBF network, because it depends mostly on the time needed for file operation (loading and saving), not on the analysis procedure itself. The drawbacks of ANN are that the network should be modified for the actual spin adducts under study and trained to experimental data obtained at the actual conditions before application and only fractions are determined from the experimental spectra. The time for programming a new RBF in Matlab, creating training and testing sets (simulations of spectra with varying fraction parameters) is around 15 minutes.

**Table 5.** Efficiency of RBF network and SBF Iterative fitting analysis\*.

Action	RBF network	Iterative fitting
Preprocessing data	15 min	0
Training	0.4 s	0
analysis of 1 spectrum	0.12 s	156 s
analysis of 600 spectra	0.25 s (3s)**	1560 min
analysis of 1000 spectra	0.28 s	2600 min

\* The numbers were obtained on a pc with 1.9 GHz AMD Turion processor and 2GB RAM.

\*\* Total time of analysis including loading spectra from file and saving results to file

In general, the choice of the method for experimental data analysis and processing depends on which information should be extracted from experimental spectra (e.g. only fraction coefficients and intensity of ESR spectra as a function of time or , in addition, other parameters if one expects that the spectra will change as well), the availability of sufficient, high quality data for creating the set of simulated spectra for neural network training and the number of spectra. Even in the unfavorable case that a new system has to be analyzed and a RBF network has to be trained for that system (15 min), RBF will be beneficial already if more then 10 spectra have to be considered (Figure 8). Moreover, the developed RBF network can be used for real time analysis of spectral components during kinetic measurements

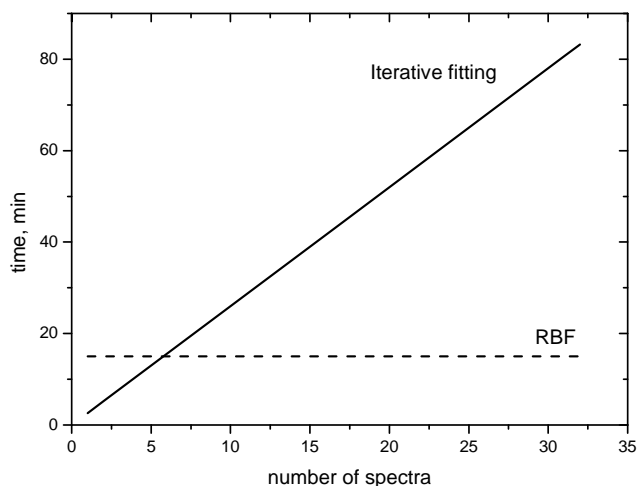


**Figure 8.** Computing time for the RBF network (dotted line) and iterative SBF (solid line) approach as a function of the number of spectra.

## 6.4 Conclusions

The RBF neural network approach was shown to be highly efficient for the analysis of strongly overlapping two component ESR spectra from FDMPO radical adducts. The same accuracy of the fraction coefficient was obtained for all systems under study by the artificial neural network as compared to SBF method. ANN performs well on new spectra with signal/noise of at least 200. The neural networks were separately trained for Fenton reaction in DMSO and Fenton reaction in methanol. Despite the time needed for preprocessing spectra and training procedures, ANN approach is faster than iterative fitting and can be used for real time analysis of experimental spectra.



## REFERENCES

- Bacic, G., I. Spasojevic, et al. (2008). "Spin-trapping of oxygen free radicals in chemical and biological systems: New traps, radicals and possibilities." Spectrochim. Acta Mol. Biomol. Spectros. **69**(5): 1354-1366.
- Bishop, C. M. (1995). Neural Networks for Pattern Recognition, Oxford University Press, Inc.
- Budil, D. E., S. Lee, et al. (1996). "Nonlinear-Least-Squares Analysis of Slow-Motion EPR Spectra in One and Two Dimensions Using a Modified Levenberg-Marquardt Algorithm." J. Magn. Reson. **120**(2): 155-189.
- Busi, E., V. Travagli, et al. "Simulation of EPR Spectra as a Tool for Interpreting the Degradation Pathway of Hyaluronan." Appl. Magn. Reson. **37**(1): 325-337.
- Buxton, G., V., C. Greenstock, L., et al. (1988). Critical review of rate constants for reactions of hydrated electrons, hydrogen atoms and hydroxyl radicals in aqueous solution. Melville, NY, ETATS-UNIS, American Institute of Physics.
- Chalier, F. and P. Tordo (2002). "5-Diisopropoxyphosphoryl-5-methyl-1-pyrroline N-oxide, DIPPMPO, a crystalline analog of the nitron DEPMPPO: synthesis and spin trapping properties." J. Chem. Soc. Perkin Trans.2, **2**(12): 2110-2117.
- Finkelstein, E. L. I., G. M. Rosen, et al. (1979). "Spin Trapping of Superoxide." Mol. Pharmacol. **16**(2): 676-685.
- Frejaville, C., H. Karoui, et al. (1995). "5-(Diethoxyphosphoryl)-5-methyl-1-pyrroline N-oxide: a new efficient phosphorylated nitron for the in vitro and in vivo spin trapping of oxygen-centered radicals." J. Med. Chem. **38**(2): 258-265.
- Hagan, M. T., H. B. Demuth, et al. (1996). Neural network design, PWS Publishing Co.
- Haykin, S. (1998). Neural Networks: A Comprehensive Foundation (2nd Edition), Prentice Hall.
- Israelachvili, J., J. Sjöstén, et al. (1975). "ESR spectral analysis of the molecular motion of spin labels in lipid bilayers and membranes based on a model in terms of two angular motional parameters and rotational correlation times." Biochim. Biophys. Acta **382**(2): 125-141.
- Janzen, E. G. (1971). "Spin trapping." Acc. Chem. Res. **4**(1): 31-40.
- Janzen, E. G. (1998). Spin trapping. Foundations of modern EPR. G. R. Eaton, S. S. Eaton and K. M. Salikhov, Singapore: World Scientific.

- Janzen, E. G., H. J. Stronks, et al. (1985). "Chemistry and biology of Spin-Trapping radicals associated with halocarbon metabolism in vitro and in vivo." Environ. Health Perspect. **64**: 151-170.
- Khan, N., C. M. Wilmot, et al. (2003). "Spin traps: in vitro toxicity and stability of radical adducts." Free Radic. Biol. Med. **34**(11): 1473-1481.
- Khramtsov, V. V., V. A. Reznikov, et al. (2001). "NMR spin trapping: detection of free radical reactions with a new fluorinated DMPO analog." Free Radic. Biol. Med. **30**(10): 1099-1107.
- Kirste, B. (1992). "Methods for automated analysis and simulation of electron paramagnetic resonance spectra." Anal. Chim. Acta **265**(2): 191-200.
- Lee, C.-H., T.-S. Lin, et al. (2002). "EPR studies of free radical reactions of C60 embedded in mesoporous MCM-41 materials in aqueous solution." Phys. Chem. Chem. Phys. **4**(13): 3106-3111.
- Milne, P. J., G. Zika Rod, et al. (1989). Rate of Reaction of Methanesulfonic Acid, Dimethyl Sulfoxide, and Dimethyl Sulfone with Hydroxyl Radical in Aqueous Solution. Biogenic Sulfur in the Environment, American Chemical Society. **393**: 518-528.
- Nelder, J. A. and R. Mead (1965). "A simplex method for function minimization." Comp. J. **7**(4): 308-313.
- Rigg, T., W. Taylor, et al. (1954). "The rate constant of the reaction between hydrogen peroxide and ferrous ions." J. Chem. Phys. **22**(4): 575-577.
- Rokhina, E. V., K. Makarova, et al. (2010). "Free Radical Reaction Pathway, Thermochemistry of Peracetic Acid Homolysis, and Its Application for Phenol Degradation: Spectroscopic Study and Quantum Chemistry Calculations." Environ. Sci. Technol. **44**(17): 6815-6821.
- Smirnov, A. I., T. I. Smirnova, et al. (1995). "Very high frequency electron paramagnetic resonance of 2,2,6,6-tetramethyl-1-piperidinyloxy in 1,2-dipalmitoyl-sn-glycero-3-phosphatidylcholine liposomes: partitioning and molecular dynamics." Biophys. J. **68**(6): 2350-2360.
- Staško, A., P. Raptá, et al. (1993). "Application of spin trapping to the kinetic study in the photolysis of sulfonium salts." Appl. Magn. Reson. **5**(3): 457-466.
- Stevens, G. C., R. M. Clarke, et al. (1972). "Radiolysis of aqueous methane solutions." J. Phys. Chem. **76**(25): 3863-3867.
- Stoll, S. and A. Schweiger (2006). "EasySpin, a comprehensive software package for spectral simulation and analysis in EPR." J. Magn. Reson. **178**: 42-55.

- Wasserman, P. D. (1989). Neural computing : theory and practice / Philip D. Wasserman.  
New York :, Van Nostrand Reinhold.
- William, M. (1986). Introduction to probability and statistics (7th ed.), Duxbury Press.
- Yamazaki, I. and L. H. Piette (1991). "EPR spin-trapping study on the oxidizing species  
formed in the reaction of the ferrous ion with hydrogen peroxide." J. Am. Chem. Soc.  
**113**(20): 7588-7593.





## **Chapter 7**

### **SUMMARIZING DISCUSSION**

#### **7.1 Introduction**

ESR spectroscopy is a powerful tool for the direct study of free radicals, providing information about their surrounding, identity and motion. However, the analysis of ESR spectra is a challenging task because of the complexity of the spectra and partly overlapping peaks. In this thesis methods to analyze fast motion ESR spectra from spin probes and spin trap adducts are presented. As a first step spectra simulation is needed in order to obtain accurate ESR parameters of the contributing components, especially in the case of overlapping ESR spectral components. This situation was met in the study of model membranes by use of the distribution of the TEMPO spin probe over the water and the lipid phases (Chapter 2), as well as the formation of various spin adducts in spin trap studies of reactions that involve radical species (Chapters 3,4,5,6).

In the spin trap studies the next step is identification of the spin adducts based on the obtained hyperfine splitting values. This has been approached by use of an artificial neural network (ANN) and/or calculations of the theoretical hyperfine splitting constants based on electronic structure calculations. These calculations, in combination with ANN, have also been used to study the reaction pathway of the dissociation of the cleavage of peracetic acid (Chapter 5).

#### **7.2 Modeling and analysis of the ESR spectrum (Chapters 2,3,4,5,6)**

In this work simulation based fitting (SBF) was used for the analysis of ESR spectra. An experimental ESR spectrum was approximated by a simulated one based on a

mathematical model. The optimization algorithm varies parameters within the model in order to minimize the difference between the two spectra (error function). The same mathematical model was successfully used for the modeling of the ESR spectra from the TEMPO spin probe (Chapter 2) and from various spin traps (Chapters 3, 4, 5, 6). The ESR line shape was described by a convolution of Lorentzian and Gaussian lineshapes. The aim of the computer simulations was to obtain the ESR parameters with high accuracy, i.e. the optimization routine should find a global minimum of the error function. It turns out that the accuracy of the parameters obtained from the simulations of the ESR spectra measured at X (9.5 GHz), Q (34 GHz) and W-band (95 GHz) increased with the frequency. Only for the W-band spectrum the optimization routine found a global minimum. For the Q and X-band spectra the optimization ended at some local minimum. It appeared that in the model for the fast isotropic ESR spectrum simulations the rotational correlation time and the line broadening are strongly correlated. These correlated parameters can direct the optimization routine to multiple local minima, decreasing the accuracy of the parameters obtained from X and Q-band. The effect of the correlated parameters diminished with the increase of frequency. At W-band a high accuracy of the parameters can be obtained.

Other models of isotropic motion reported in previous studies use more parameters for spectra simulations. That results in more correlated parameters and that decreases the efficiency of optimization routine because the global minimum cannot be achieved. Then either more complicated and time consuming routines are implemented in order to ensure that the optimization finds global minimum or the same SBF performed 10-100 times in order to get the average values. In contrast to previous studies presented in literature, where the main goal was to improve the optimization routine used to find the global minimum, in this work the global minimum was achieved by elimination of the correlation between the parameters in the model by using high frequency. Since the rotational correlation time is independent of the frequency, the simulations of X and Q-band spectra can be performed with rotational correlation times defined from the W-band measurements. Doing so, the accuracy of the remaining parameters was greatly improved.

Values of the rotation correlation time of TEMPO in water (6 ps) and in DOPC lipids (62 ps) (Chapter 2) obtained from simulation based fitting are in agreement with previous reported studies where SBF were used for the extraction of the correlation time from W-band ESR spectra. It is not surprising because at W-band or higher frequency there is no correlation between parameters and thus no problem of finding global minimum.

In case of spin trapping ESR all radical adducts are in the same solvent, thus the line broadening effect due to presence of paramagnetic oxygen is similar for all spectral components. However, the rotational correlation times of different radical adducts depend on the structure of the trapped radical. In this case one broadening parameter was used for the simulation of all radical adduct components, however the correlation time parameters were different. That also decreases the correlation between parameters at X-band and improves the accuracy of obtained parameters.

SBF was applied to extract accurate values of hyperfine splitting constants of POBN (Chapter 3), FDMPO (Chapters 4 and 6) and DIPPMPO (Chapter 5) radical adducts, in order to identify the trapped radicals. In addition, fitting of the experimental spectra allowed to follow the kinetics of each radical adduct. SBF revealed POBN/CH(CH<sub>3</sub>)OH\* ( $a_N=15.5\text{G}$ ,  $a_H=2.5\text{G}$ ), POBN/OH\* ( $a_N=15.0\text{G}$ ,  $a_H=1.6\text{G}$ ) and POBN/CH<sub>2</sub>OH\* ( $a_N=15.4\text{G}$ ,  $a_H=2.8\text{G}$ ) in the spin trapping studies of the Fenton reaction with ethanol and methanol (Chapter 3). For both reactions the presence of taxifolin resulted in a decrease of the spectrum intensity of the radical adducts.

In Chapter 6, the influence of pollen extracts (narcissus and pine) on the Fenton reaction with methanol and with dimethylsulfoxide was studied using SBF. The obtained hyperfine splitting values correspond to FDMPO/OH\*, FDMPO/CH<sub>3</sub>\* observed in the Fenton reaction with dimethylsulfoxide and FDMPO/OH\*, FDMPO/CH<sub>2</sub>OH\* observed in the Fenton reaction with methanol. The obtained parameters, i.e. nitrogen and fluorine hyperfine splitting constants,  $g_{iso}$ , rotation correlation time and line broadening, were used for the simulations of spectra for the training and testing sets of artificial neural networks.

SBF revealed 5 components in the ESR spectrum of the reaction medium, where peracetic acid cleavage over MnO<sub>2</sub> took place in the presence of the spin trap DIPPMPO (Chapter 5). Obtained hyperfine splitting values of spectral components suggested the hydroxyl adduct as the main component and several carbon-centered adducts. The extracted values of the hyperfine splitting constants of POBN, FDMPO and DIPPMPO spin traps are in agreement with values presented in literature. In addition, hyperfine splitting constants of a new free radical, CH<sub>3</sub>(C=O)O\*, were obtained for the corresponding DIPPMPO ( $a_F=50.9\text{G}$ ,  $a_N=10.2\text{G}$ ,  $a_H=13.9\text{G}$ ) and FDMPO ( $a_N=13.8\text{G}$ ,  $a_F=2.46\text{G}$ ) spin adducts (Chapters 4 and 5).

The SBF is successfully used for ESR spectra decomposition and extraction of parameters, however SBF does not recognize radical adducts. The conclusion about radical

adduct identity is drawn based on previously published data or producing the same radical adduct in another way.

### 7.3 DFT calculations (Chapters 4 and 5)

As it was reported in previous studies, comparison between the theoretical ESR parameters, calculated on the basis of DFT optimized geometries, and the ESR experimental parameters of the studied paramagnetic species is a successful method for the species structural identification. However, in order to draw a sound conclusion based on theoretically calculated ESR parameters DFT calculations should use an appropriate basis set and should consider solvent–solute interactions and sometimes also motional effects. In this work the appropriate settings for DFT calculations were selected based on calculations of known radical adducts, such as FDMPO/OH and FDMPO/CH<sub>3</sub>. Hyperfine splitting constants of various FDMPO radical adducts were calculated using DFT calculations at B3LYP/6-31G\*\* level of theory (Chapter 4). Good agreement between the theoretically calculated and the experimentally obtained hyperfine splitting constants of FDMPO/OH\* ( $a_N = 13.3$  G,  $a_F = 2.6$  G), FDMPO/CH<sub>2</sub>OH\* ( $a_N = 14.43$  G,  $a_F = 2.45$  G), FDMPO/CH<sub>3</sub>\* ( $a_N = 14.63$  G,  $a_F = 2.52$  G) was achieved if the solvent effect and effect of the rotation of the trifluoromethyl group was included in the calculations. The good agreement between the experimental ESR parameters and the theoretical ESR parameters ( $a_N = 13.27$  G,  $a_F = 1.99$  G) calculated on the basis of optimized geometry of FDMPO/CH<sub>3</sub>(C=O)O\* allows identification of the new radical adduct observed in the reaction of cleavage of peracetic acid over MnO<sub>2</sub> (Chapter 4).

DFT calculations at B3LYP/6-31g(d) level of theory were performed in order to study the reaction pathway of the homolysis of peracetic acid, i.e. dissociation of the O-O bond of peracetic acid and formation of free radicals (Chapter 5). The optimized geometry of the reactants, products and transition structures were obtained. The heat of formation of peracetic acid (-76.7 kcal mol<sup>-1</sup>) calculated by adopting an atomization approach at HF/6-31G (d) level of theory as well as the calculated O-O bond dissociation energy (48 kcal mol<sup>-1</sup>) are higher than values reported previously, calculated by the group additivity methods. However, this has little effect upon the relative available energies. Therefore, such data can be used to construct an energy diagram for the radical reaction pathway. Our DFT calculations revealed that the dissociation of the peracetic acid O-O bond produced two primary radicals, \*OH and CH<sub>3</sub>(C=O)O\*. The subsequent formation of secondary radicals, CH<sub>3</sub>CO\*, CH<sub>3</sub>(C=O)<sub>2</sub>O\*, CH<sub>3</sub>\* and CH<sub>3</sub>OO\*, was nearly spontaneous. This information was not directly accessible from spin trapping ESR, which only reveals free radicals that react with the spin trap.

## 7.4 Artificial neural networks (Chapters 4, 5 and 6)

Artificial neural networks (ANN) solve different linear and non linear approximation problems. However, each application of an ANN requires an individual architecture design. In general, a multilayer perceptron (MLP) with several hidden layers is a good starting point, due to its ability to approximate any non-linear function. However, in some cases when the desired accuracy of the MLP output either cannot be achieved with current ANN architecture or the training of the MLP takes too long (several days) then other types of ANN should be checked for the better performance.

The MLP type of ANN was used for the estimation of FDMPO radical adduct structures based on their ESR parameters (Chapter 4). Being trained only on previously published data ANN successfully associated the experimentally obtained hyperfine splitting constants with a pre-defined group of FDMPO radical adducts. The FDMPO radical adducts were grouped based on a similar structure of the radical addends, i.e. FDMPO radical adducts that contains carbon-centered spin adducts without oxygen (e.g.  $\text{CH}_3^*$  and  $\text{CH}\equiv\text{C}^*$ ) are assigned to one group, whereas the other group includes carbon-oxygen FDMPO radical adducts with a CO (alkoxyl) group ( $\text{CH}_2\text{OH}^*$ ,  $\text{CH}_3\text{CHOH}^*$  and etc). Nevertheless, although the ANN does not provide a chemical structure of the radical adduct, it is very efficient for the preliminary analysis of the type of trapped radicals (c-centered, hydroxyl, etc.). ANN performed well on FDMPO/ $\text{CH}_3(\text{C}=\text{O})\text{O}^*$  which is totally new and assigned it to carbon-oxygen FDMPO radical adducts with a CO (alkoxyl) group. This approach is potentially important for the analysis of multi-component free radical systems with a variety of free radicals.

In Chapter 5 it is demonstrated that a multilayer perceptron type of ANN associates well the removal efficiency of phenol with relevant process parameters (concentrations of  $\text{MnO}_2$  and PAA and the reaction time). Being trained on a limited experimental dataset the ANN predicted phenol removal rates for the different  $\text{MnO}_2$  and PAA concentrations. This allowed determining the optimal parameters ( $0.7 \text{ g L}^{-1}$  of  $\text{MnO}_2$  and 50 ppm of PAA) for the highest removal efficiency of phenol (80%) in 120 min, without performing a large number of experiments. The control experiment using the optimized parameters confirmed the predicted ANN values of the removal efficiency.

A radial basis function network, another type of an artificial neural network, was adopted to extract the fraction coefficients of different FDMPO spin adduct components from an ESR spectrum (Chapter 6), since MLP failed on experimental data. In contrast to SBF this method is significantly faster already when more than 20 spectra are analyzed. This radial

basis function network was applied to the decomposition of two-components ESR spectra from FDMPO radical adducts formed in the Fenton reaction with dimethylsulfoxide or with methanol in the presence of the extract of pine pollen and narcissus pollen. The radial basis function network analyzed a set of 600 spectra in less than 1 minute, whereas the fitting approach required around 1500 minutes for the same number of spectra. Thus the radial basis function neural network approach is highly efficient for the analysis of large number of ESR spectra if only fractions of components and intensity of the ESR spectra are varied. It turns out that the compounds extracted from narcissus pollen scavenge both  $\text{OH}^*$  and  $\text{CH}_2\text{OH}^*$ , demonstrating the antioxidant activity in relation to these two free radicals in the Fenton reaction with methanol. The extract from pine pollen clearly shows anti-oxidant activity in relation to hydroxyl radicals only in the Fenton reaction with dimethylsulfoxide.

## **7.5 General conclusions**

The improved method to simulate fast isotropic ESR spectra from TEMPO spin probes and various spin traps presented in this thesis results in high accuracy ESR parameters. With the inclusion of W-band data to simulations very accurate ESR parameters are obtained even from X-band spectra. Moreover, application of the ANN to the extraction of the fraction of the spectral components in X-band ESR spectra from spin adducts decreases drastically the time of analysis. The obtained ESR parameters of spin adducts were interpreted by ANN (identification of trapped radicals) and DFT calculations (both identification of trapped free radicals and following the reaction pathway which result in formation of observed free radicals). In general, a combination of the proposed methods, i.e. simulation based fitting of ESR spectra, artificial neural networks analysis and DFT calculations, is needed to extract successfully the unique information from ESR spectra of spin traps.

## Chapter 8

### SAMENVATTING

Electron Spin Resonantie (ESR) is een krachtige techniek waarmee direct aan vrije radicalen gemeten kan worden. Hierbij wordt informatie verkregen over de locale omgeving en de moleculaire beweging van de radicalen. De analyse van ESR spectra is echter nog steeds een uitdagende taak vanwege de complexiteit van de spectra en (gedeeltelijke) overlap van resonantie lijnen van verschillende componenten. In dit proefschrift worden een drietal methoden gepresenteerd en vergeleken om ESR spectra van spin probe moleculen en radicalen die met zogenaamde spin trap moleculen een adduct vormen die met ESR waar te nemen zijn, in de vloeistof fase (snelle, isotrope beweging) te analyseren. Deze analyse methoden zijn toegepast om model membranen te bestuderen via de verdeling van de spin probe TEMPO over de water en de lipide fase (hoofdstuk 2). Daarnaast is de vorming van radicaal spin trap adducten in reacties waarbij radicalen betrokken zijn bestudeerd en zijn de radicaal adducten geïdentificeerd (hoofdstukken 3-6). Als voorbeeld is de Fenton reactie, een overgangsmetaal gekatalyseerde oxidatiereactie, gebruikt. De Fenton reactie is de opsplitsing van waterstofperoxide (de oxidator,  $\text{H}_2\text{O}_2$ ) door reactie met een ijzer(II) ion (de katalysator,  $\text{Fe}^{2+}$ ) in zeer reactieve (radicaal) deeltjes die in staat zijn organische moleculen te oxideren. Hoewel deze reactie al in 1876 door H.J.H. Fenton werd ontdekt en sindsdien onderwerp van ontelbaar veel studies is geweest, is het reactiemechanisme en de aard van de zeer reactieve deeltjes meer dan een eeuw later nog steeds niet met zekerheid bekend. Het grootste experimentele probleem is dat de reactieve deeltjes slechts een zeer korte tijd bestaan voordat ze reageren, zodat ze nauwelijks direct in een meting zijn waar te nemen. Desalniettemin wordt de Fenton reactie (en varianten hierop) veelvuldig toegepast in de industrie. Het probleem van de korte levensduur van de reactieve deeltjes is hier ondervangen door de radicalen te laten reageren met verschillende ESR spin traps, waarbij langer levende radicaal spin trap adducten worden gevormd. Identificatie van deze radicaal adducten is gebaseerd op de waarde van de hyperfijn splitsingsconstanten. Deze is benaderd door middel van (1) fitten

van de experimentele spectra op basis van spectra verkregen via een mathematisch simulatie model (SBF), (2) toepassing van artificieel neurale netwerken (ANNs) en/of (3) berekeningen van de theoretische waarden gebaseerd op de elektronen structuur van de radicaal adducten. Deze berekeningen, in combinatie met de toepassing van ANN, zijn ook gebruikt om het reactiepad van de (katalytische) dissociatie van perazijnzuur (PAA), een bekend radicaalvormend antimicrobieel middel, te ontrafelen (hoofdstuk 5).

In SBF worden via een optimalisatie algoritme de parameters binnen het model gevarieerd, zodanig dat het verschil tussen de twee spectra (de error functie) een vooraf gedefinieerd minimum bereikt. Een nieuw model is gebruikt met minder variabele parameters dan in de reeds in gebruik zijnde modellen. Deze oude modellen resulteren in (sterke) correlaties tussen de parameters en daardoor in verlies van efficiëntie en nauwkeurigheid. Het hier beschreven model (hoofdstuk 2) kon succesvol toegepast worden voor verschillende omgevingen, zowel voor de ESR spectra van de spin probe TEMPO in water en lipide fase als van verschillende radicaal spin trap adducten gevormd door Fenton reacties (hoofdstukken 3-6). De lijnvorm wordt beschreven met een convolutie van een Lorentz en een Gauss lijnvorm. Het blijkt dat parameters verkregen met dit model nauwkeuriger worden bij spectra verkregen met X (9.5 GHz), Q (34 GHz) en W-band (95 GHz) ESR spectrometers, respectievelijk. Alleen voor de W-band spectra resulteerde de optimalisatie in een echt globaal minimum voor de error functie. Voor spectra verkregen met X en Q-band eindigde de optimalisatie van de error functie in een of ander lokaal minimum. Gebleken is dat er in het gebruikte model een sterke correlatie bestaat tussen twee parameters: de rotatie correlatietijd en de lijnverbreding. Het effect van deze correlatie vermindert bij toename van de meetfrequentie. Bij W-band wordt een hoge nauwkeurigheid en reproduceerbaarheid voor beide parameters verkregen. De rotatie correlatietijd is niet afhankelijk van de meetfrequentie, in tegenstelling tot de lijnverbreding. Daarom kunnen de resultaten met X en Q-band verkregen sterk verbeterd worden in nauwkeurigheid als de waarde van de rotatie correlatietijd verkregen via een enkele (referentie) meting met W-band, gebruikt wordt voor simulatie van de eenvoudiger te meten X of Q-band spectra.

Waarden van de op deze manier verkregen rotatie correlatietijd van TEMPO in water (6 ps) en in DOPC (62 ps) zijn in goede overeenstemming met eerder gepubliceerde waarden verkregen met andere simulatiemodellen aan W-band ESR spectra. Dit is niet echt verwonderlijk, omdat bij die (of nog hogere) frequentie er geen correlatie meer is tussen de parameters.



Voor de spin trap ESR studies zijn alle radicaal spin adducten in hetzelfde oplosmiddel gemeten en het lijnverbredingseffect door de aanwezigheid van zuurstof is vergelijkbaar voor alle spectrale componenten. De rotatie correlatietijden van de verschillende radicaal adducten echter zijn afhankelijk van de structuur van de ingevangen radicalen. In dit geval kon voor het SBF model dezelfde lijnverbredingsparameter worden gebruikt voor alle radicaal adducten, maar verschillende rotatie correlatietijden waren vereist. Op deze manier kon de correlatie tussen deze twee parameters in het SBF model voor simulatie van X-band ESR spectra sterk worden geminimaliseerd.

SBF is toegepast om nauwkeurige waarden van de hyperfijn splitsingsconstanten voor POBN (hoofdstuk 3), FDMPO (hoofdstuk 4 en 6) en DIPPMPO (hoofdstuk 5) radicaal adducten te verkrijgen uit X-band ESR spectra. Op deze manier konden in de reacties gevormde en ingevangen radicalen worden geïdentificeerd en de kinetiek van elk radicaal adduct tijdens de reacties worden gevolgd. In de Fenton reactie in ethanol en methanol (hoofdstuk 3) werden zo POBN/CH(CH<sub>3</sub>)OH\*, POBN/OH\* en POBN/CH<sub>2</sub>OH\* aangetoond. Voor beide reacties had de aanwezigheid van taxifoline een afname in de intensiteit van de radicaal adducten tot gevolg, een duidelijke indicatie voor antioxidant activiteit. SBF is toegepast om het effect van pollen extracten (narcus en den) op de Fenton reactie met methanol en met dimethylsulfoxide te bestuderen met behulp van de spin trap FDMPO. De gevonden hyperfijn splitsingsconstanten corresponderen met die van FDMPO/OH\*, FDMPO/CH<sub>3</sub>\* in het geval van de Fenton reactie met dimethylsulfoxide en met die van FDMPO/OH\* en FDMPO/CH<sub>2</sub>OH\* in het geval van de Fenton reactie met methanol. De gevonden waarden voor de hyperfijn splitsingsconstanten,  $g_{iso}$ , de rotatie correlatietijden en de lijnverbreding zijn gebruikt voor de trainings- en testsets voor ANNs.

Met behulp van SBF aan de ESR spectra van het reactiemedium waarin PAA werd gesplitst over MnO<sub>2</sub> in aanwezigheid van de spin trap DIPPMPO (hoofdstuk 5) werden 5 componenten aangetoond. Op grond van de hyperfijn splitsingsconstanten kon worden geconcludeerd dat het hydroxyl adduct de belangrijkste component was. Daarnaast kwamen verschillende koolstofgecentreerde radicaal adducten voor.

De gevonden waarden voor de hyperfijn splitsingsconstanten van POBN, FDMPO en DIPPMPO radicaal adducten zijn in goede overeenstemming met waarden gepresenteerd in de literatuur. Daarnaast zijn de hyperfijn splitsingsconstanten van een niet eerder waargenomen radicaal, CH<sub>3</sub>(C=O)O\*, gevonden, voor de spin adducten met DIPPMPO en FDMPO (hoofdstukken 4 en 5).

SBF kan succesvol worden ingezet voor de decompositie van ESR spectra en om parameters die de spectra bepalen te extraheren, maar kan niet worden toegepast om radicaal adducten te identificeren. Identificatie is gebaseerd op eerder gepubliceerde data van ESR parameters of via kwantummechanische berekeningen op basis van de elektronenstructuur voor de betreffende structuur volgens het principe van de dichtheid functionaal theorie (DFT). Kennis van de elektronenstructuur in moleculen maakt het mogelijk om naast ESR parameters zoals de hyperfijn splitsingsconstanten ook de chemische reacties tussen moleculen te voorspellen en te begrijpen.

Vergelijking van experimentele en theoretische ESR parameters, verkregen op basis van DFT geoptimaliseerde structuren, is een succesvolle methode om het soort paramagnetische molecuul te identificeren. Om echter een correcte conclusie te kunnen trekken moeten de DFT berekeningen een juiste basisset gebruiken en interacties met het oplosmiddel/medium en eventueel ook kinetische effecten van/in het molecuul meenemen. Hier zijn als uitgangspunten voor de DFT berekeningen settings en parameters gebruikt die een succesvolle vergelijking gaven van de resultaten met bekende radicaal adducten, zoals FDMPO/OH\* en FDMPO/CH<sub>3</sub>\*. Hyperfijn splitsingsconstanten van verschillende FDMPO radicaal adducten zijn berekend met DFT op B3LYP/6-31G structuurniveau (hoofdstuk 4). Goede overeenstemming voor FDMPO/OH\*, FDMPO/CH<sub>2</sub>OH\* en FDMPO/CH<sub>3</sub>\* werd gevonden als het effect van het oplosmedium en rotatie van de trifluoromethyl groep in de berekening voor de hyperfijn splitsingsconstante werden meegenomen. De goede overeenkomst tussen experimentele en theoretische waarden van de hyperfijn koppelingsconstanten voor FDMPO/CH<sub>3</sub>(C=O)O\* is gebruikt voor de identificatie van dit nieuwe radicaal adduct in de reactie voor de splitsing van PAA over MnO<sub>2</sub> (hoofdstuk 4). DFT berekeningen met de B3LYP/6-31G basisset zijn vervolgens ook uitgevoerd om het reactiepad van de homolyse van PAA, i.e. de dissociatie van de O-O binding van PAA en de vorming van vrije radicalen, te bestuderen (hoofdstuk 5). Op deze manier werden de geoptimaliseerde structuren van de reactanten, producten en overgangsstructuren verkregen. De berekende vormingsenthalpie van PAA (-76.7 kcal mol<sup>-1</sup>) en de bindingsdissociatie energie (48 kcal mol<sup>-1</sup>) zijn hoger dan waarden gepubliceerd op grond van een iets andere methode. Dit heeft echter weinig effect op de relatieve beschikbare energieën. Daarom kunnen de aldus verkregen gegevens gebruikt worden om een energiediagram te maken voor het radicaal reactiepad. Onze DFT berekeningen legden bloot dat de dissociatie van de O-O binding in PAA resulteerde in twee primaire radicalen, OH\* en CH<sub>3</sub>(C=O)O\*. De daarop volgende vorming van secundaire radicalen, CH<sub>3</sub>CO\*, CH<sub>3</sub>(C=O)<sub>2</sub>O\*, CH<sub>3</sub>\* en CH<sub>3</sub>OO\*,

was nagenoeg spontaan. Deze informatie was niet direct te verkrijgen uit de spin trap studies, waarmee alleen radicalen die reageren met de spin trap te zien zijn.

De derde benadering is met behulp van ANN's. ANN's worden gebruikt voor het oplossen van verschillende lineaire en niet-lineaire benaderingsproblemen. Elke toepassing van een ANN vereist een individueel architecturaal ontwerp. Hier zijn twee verschillende ANN's gebruikt: een multilaags perceptron (MLP) met verschillende verborgen lagen, en een radiaal basisfunctie netwerk (RBF). De laatste werd gebruikt voor die gevallen waar de MLP faalde.

Een MLP is gebruikt voor de schatting van de waarschijnlijkheid dat FDMPO radicaal adducten, die vallen binnen bepaalde van te voren gedefinieerde structuurklassen, aanwezig waren (hoofdstuk 4). De MLP werd hierbij getraind met reeds eerder gepubliceerde data. De FDMPO radicaal adducten konden worden gegroepeerd op basis van vergelijkbare structuur van de radicalen, i.c. koolstof gecentreerd zonder zuurstof (bv  $\text{CH}_3^*$  en  $\text{CH}\equiv\text{C}^*$ ) als een groep, terwijl een andere groep uit koolstof-zuurstof radicaal adducten met een CO-groep (bv.  $\text{CH}_2\text{OH}^*$ ,  $\text{CH}_3\text{CHOH}^*$ , etc) bestaat. De ANN was zeer efficiënt om een eerste analyse te doen om de type radicaal adducten te herkennen, echter zonder echt te identificeren. Zelfs het totaal nieuw gevonden FDMPO/ $\text{CH}_3(\text{C}=\text{O})\text{O}^*$  adduct werd geclassificeerd in de koolstof-zuurstof FDMPO radicaal adducten met een CO (alkoxyl) groep. Deze benadering is potentieel belangrijk voor de analyse van multi-component vrije radicaal systemen met verschillende radicalen.

Een MLP netwerk was zelfs succesvol om de efficiëntie van de afbraak van fenol te associëren aan relevante procesparameters (concentratie  $\text{MnO}_2$ , PAA en de reactietijd). Eenmaal getraind met een beperkte experimentele dataset voorspelde de ANN de afbraaksnelheid van fenol voor de verschillende  $\text{MnO}_2$  en PAA concentraties. Hiermee konden de optimale parameters voor de hoogste afbraak efficiëntie voor fenol worden bepaald, zonder een groot aantal experimenten te moeten uitvoeren. Het controle experiment onder de geoptimaliseerde parameters bevestigde de voorspelde waarden van de afbraakefficiëntie (hoofdstuk 5).

Een RBF netwerk werd opgezet om succesvol de fractiecoëfficiënten van verschillende FDMPO radicaal spin adducten uit experimentele ESR spectra te extraheren (hoofdstuk 6). MLP faalde hierin. Het RBF netwerk was aanzienlijk sneller dan SBF, zodat al bij meer dan 20 spectra, ondanks de tijd nodig voor de trainingsstap, er tijdwinst optrad. Dit RBF netwerk werd gebruikt om (twee component) ESR spectra van FDMPO radicaal adducten te ontleden. Deze adducten werden gevormd in de Fenton reactie met

dimethylsulfoxide of met methanol, in afwezigheid en aanwezigheid van pollenextracten van den of narcis. Het RBF netwerk analyseerde een set van 600 spectra in minder dan 1 minuut, terwijl SBF voor hetzelfde aantal rond de 1500 minuten nodig had. Dit demonstreert dat ANNs zeer efficiënt zijn om grote aantallen complexe ESR spectra te analyseren als alleen de fracties van de componenten, of intensiteiten in de ESR spectra, variëren.

Beide pollen extracten vertoonden antioxidant activiteit. Het extract van narcispollen in methanol vangt zowel  $\text{OH}^*$  als  $\text{CH}_2\text{OH}^*$  weg, het extract van denpollen in dimethylsulfoxide tegen hydroxyl radicalen.

In het algemeen is een combinatie van de drie voorgestelde analyse methoden nodig om succesvol de unieke informatie verborgen in ESR spectra van spin trap moleculen uit de spectra te halen.

## ACKNOWLEDGEMENTS

It would not have been possible to write this thesis without the help, both direct and indirect, and support of the people around me. In this chapter of my thesis I would like to thank all of them. First of all I would like to thank all my supervisors who shared their knowledge and time with me.

I would like to thank Dr. Marcus A. Hemminga, my supervisor at the beginning of the project, who gave me a chance of starting the Sandwich PhD at the Biophysics group in Wageningen University.

I am very grateful to Dr. Igor Borovykh, my supervisor during the whole period of my PhD studies, for sharing his knowledge on sample preparation, using both X-band and D-band ESR spectrometers, high-field measurements and discussions. Thank you for your support in all aspects of my research. I learned a lot from you and I am very proud to be your student.

I gratefully acknowledge Jurate Virkutyte for supervising me and giving me the opportunity to apply for the EU Fellowship to carry out my first spin trapping research project.

I also would like to thank Prof. Dr. Vladimir V. Apanasovich, my supervisor at the department of System Analysis in Belarusian State University.

Of course, the finalizing of this thesis would not have been possible without the help, support and patience of my co-promotor, Dr. Henk Van As.

I am also very grateful to Prof. Dr. Herbert van Amerongen for the care with which he reviewed this thesis; and for conversations and e-mails that clarified my thinking and my writing.

I am very grateful to Dr. Elena Golovina who shared with me her knowledge of ESR and biophysics and who helped me a lot in using the X-band ESR spectrometer.

I am grateful to Netty Hoefakker, the secretary of the Biophysics group for dealing with all the bureaucratic problems in The Netherlands.

I would like to thank people I've got a chance to know in Wageningen, especially Olga, Alexej, Jura, Dasha, Justin. Thank you for parties, dinners and fun we had during my stays in Wageningen. I cannot imagine my life in Wageningen without two things. The first one is a bike, so special thanks to Sergey who was always ready to repair my bike. And the second thing is salsa, so many thanks to Salsa con Jola dance school and Jose for lessons and for salsa parties during the rain autumn and winter time.

Many thanks to Magda, Natalia and Elena Junior for a nice girls company, for shopping, dinners and, of course, for introducing me to the world of NMR.

I would like to express my gratitude to Peter Nazarov for sharing his knowledge on neural networks and simulation based fitting.

I am very grateful to Ekaterina Rokhina who motivated me to start my adventure with quantum chemistry calculations and who always has new ideas for calculations and simulations. Our friendship and professional collaboration meant a great deal to me.

My return travel from Wageningen always went through Italy. I also would like to sincerely thank my “italian” friends Marina, Andrei and Artem for nice skiing times in the Dolomiti.

During the PhD studies I traveled a lot from Minsk to Wageningen, and finally found my “center of mass” in Warsaw. I would like to thank a number of people who gave me the first lessons of Polish language and Polish hospitality, including the following: Estera, Marta, Piotrek, Ola, Gosia and Marcin - all from the Institute of Physics. Marcin, thank you for your enormous help in the optics lab! Marta, Piotrek, Ola, Gosia I am really happy that our friendship didn’t end with the end of my job contract in IF PAN.

A very important role in finalizing my thesis was played by Prof. Iwona Wawer who not only offered me a job in the department of Physical Chemistry, Warsaw Medical University but also allows me to continue the spin trapping ESR project. Being a part of the Physical Chemistry group I am working with a lot of talented and kind people. I am very grateful to Marta Jamroz who shared with me her knowledge of DFT, Gaussian 03 and chemistry and kindly provided her computer with Gaussian03 program for my DFT calculations. I would like to thank Kasia Zawada and Kasia Paradowska for sharing their knowledge in NMR and ESR, for hot coffee and for a comfortable place for coffee breaks. I would like to acknowledge Kasia Lastawska for providing ESR experimental data on the Fenton reaction in the presence of Taxifolin. I would like to thank Asia Celinska for creating a very special atmosphere in our office.

I am very grateful to all colleagues from the Biophysics group of Wageningen University, Department of Physical Chemistry (Warsaw Medical University), Division of Solid State Spectroscopy (Institute of Physics Polish Academy of Science) and System Analysis Department (Belarusian State University) for being great co-workers and creating a pleasant atmosphere for work.

I also would like to send my love and acknowledgments to my family: my parents (Svetlana and Vladimir Makarovy) and grand parents (Rosa and Vladimir Shkoldiny) who’s PhD degrees in radio physics and scientific careers inspired me not only to choose the faculty

of Radio Physics and but also to continue with a PhD after my graduation. Thank you for your love and support.

Last, but by no means least, I thank my husband, Jarek, for his patience, love and understanding and orange bike which I always took with me to Wageningen.

Katerina Makarova





## CURRICULUM VITAE

Katerina Makarova was born on the 24th of November 1981 in Gomel, Belarus (former USSR). Her elementary studies were completed at the Gomel Lyceum in 1999. After following the undergraduate studies in the Belarusian State University (Minsk, Belarus) in the period 1999-2004, she graduated from the Radio Physics faculty with an Honours diploma. In the last year of her university studies she has completed her diploma work entitled: “Modelling and analysis of ESR spectra in membrane-protein systems”. The experimental part of this work was done during her 3 month stay at the Laboratory of Biophysics, Wageningen University, under supervision of Dr. Marcus Hemminga.

2003 -2006 she studied and worked as a laboratory assistant at the Department of System Analysis (Radio Physics faculty of the Belarusian State University (Minsk)) on the research projects concerned with data analysis, neural networks and simulation modeling. September 2006 – September 2008 she studied and worked at the IF PAN on research projects concerned with FTIR, photoluminescence and ESR of solid states. During this time she also visited Gent University (ENDOR ESR) and attended courses of advanced physics of semiconductors, optics and research methods in physics.

From January 2006 until January 2011 she carried out her PhD study in the Laboratory of Biophysics, Wageningen University, as a sandwich PhD-fellow under the supervision of Dr. Igor Borovykh, Dr. Marcus Hemminga and Prof. Dr. V.V. Apanasovich and later also Dr. Henk Van As. Her scientific work was related to spin probe ESR, spin-trapping ESR and analysis and modeling of ESR spectra.

From November 2009 she is working as a teaching and research assistant at the Department of Physical Chemistry (Warsaw Medical University, Warsaw, Poland). Her scientific work is related to DFT calculations and ESR spin trapping experiments

## PUBLICATIONS

Ekaterina V. Rokhina, Katerina Makarova, Elena A. Golovina, Henk Van As, Jurate Virkutyte. Free radical reaction pathway, thermochemistry of peracetic acid homolysis and its application for phenol degradation: spectroscopic study and quantum chemistry calculations. Published in Environmental Science and Technology 44, no 17, 6815-6821 (2010).

Katerina Makarova, Katarzyna Łastawska, Katarzyna Zawada, Iwona Wawer. Spin trapping study of the influence of taxifolin on fenton reaction in ethanol and methanol. Current Topics in Biophysics Online, vol. 33 (Suplement A), 153-156 (2010)

Katerina Makarova, Ekaterina V. Rokhina, Elena A. Golovina, Henk Van As, Jurate Virkutyte. A combination of Neural Networks and DFT calculation for comprehensive analysis of FDMPO radical adducts from fast isotropic Electron Spin Resonance spectra. To be submitted.

Katerina Makarova, Igor Borovykh, Elena A. Golovina, Wawer Iwona, Henk Van As. A neural network approach to the rapid analysis of the kinetics of FDMPO free radical spin adducts from isotropic ESR spectra. To be submitted.

Katerina Makarova, Henrik Brutlach, Elena A. Golovina, Igor Borovykh. Use of multifrequency EPR and simulation-based fitting in partition studies of TEMPO in lipid bilayers. To be submitted

Makarova K., Stachowicz M., Glukhanyuk V., Kozanecki A., Ugolini C., Lin J.Y., Jiang H.X. and Zawada J., Spectroscopic studies of Er-centers in MOCVD grown GaN layers highly doped with Er. Materials Science and Engineering: B, Volume 146, Issues 1-3, 15 January 2008, Pages 193-195

Makarava K. V., Papliatseyeu A. M., Lutkovski V. M. Algorithms of automatical identification of chemical elements by optical spectra //Proceedings of Russian Scientific conference "Physics of radiowaves", Tomsk, Russia. **2002**. PP. V.9–11.

Makarava K. V., Papliatseyeu A. M., Nazarov P. V., Lutkovski V. M. Application of neural networks for compressed data processing in emission spectroscopy //Proceedings of NIRS-**2002** Contest. Belarusian Ministry of Education. Minsk, Belarus. 2003. P. 419–423.

Makarava K. V., Papliatseyeu A. M., Lutkovski V. M., Semenchik E. A., Kozhuro Yu. I. Application of pattern recognition algorithms for karyotypic analysis and detection of chromosome aberrations //Proceedings of 7<sup>th</sup> International Conference of Young Scientists, Puschino, Russia. **2003**. P. 187.

Katerina V. Makarova, Petr V. Nazarov , Vladimir V. Apanasovich, Marcus A. Hemminga, ESR experimental data analysis using simulation-based fitting approach.// Proceedings of 8<sup>th</sup> International Conference on Pattern Recognition and Information Processing (PRIP'05), Minsk